The Effects of Ice and Currents on Wave-breaking Turbulence at the Ocean Surface

Seth Zippel

A dissertation
submitted in partial fulfillment of the
requirements for the degree of

Doctor of Philosophy

University of Washington

2017

Reading Committee:

James M. Thomson, Chair

Alex R. Horner-Devine

Tim T. Janssen

Program Authorized to Offer Degree:
Civil and Environmental Engineering

University of Washington

Abstract

The Effects of Ice and Currents on Wave-breaking Turbulence at the Ocean Surface

Seth Zippel

Chair of the Supervisory Committee:
Associate Professor James M. Thomson
Civil and Environmental Engineering

Breaking waves are critical to the exchange of momentum, gasses, and heat between the atmosphere and ocean. In open water, these exchanges control the growth and decay of waves, and have implications for global heat and gas budgets. However, local geophysical properties can significantly alter these exchanges. At river inlets, strong currents influence swell that has grown over a long ocean fetch, dramatically increasing surface fluxes. The reverse effect is seen in the presence of ice, where ocean wave properties are decoupled from atmospheric forcing, decreasing exchanges across the air/sea interface. Here, measurements of ocean waves and near surface turbulence are presented to show the modification of surface boundary processes from ice and currents.

Measurements from free drifting buoys at the Mouth of the Columbia River are used to evaluate wave breaking parameterizations, where breaking occurs in intermediate depths and in the presence of vertically sheared currents. Breaking waves were identified using images collected with cameras onboard the buoys, and the breaking activity is well-correlated with wave steepness. Vertical shear in the currents produces a frequency-dependent effective current that modifies the linear dispersion relation. Accounting for these sheared currents in the wavenumber spectrum is essential in calculating the correct wave steepness; without this, wave steepness can be over (under) estimated on opposing (following) currents by up

to 20%. The observed bulk wave steepness values suggest a limiting value of 0.4. The observed fraction of breaking waves is in good agreement with several existing models, each based on wave steepness. Further, a semi-spectral model designed for all depth regimes also compares favorably with measured breaking fractions. In this model, the majority of wave breaking is predicted to occur in the higher frequency bands (i.e., short waves). There is a residual dependance on directional spreading, in which wave breaking decreases with increasing directional spread.

Observations at the Columbia River Mouth are also used to investigate the source and vertical structure of turbulence in the surface boundary layer. Turbulent velocity data collected onboard SWIFT buoys were corrected for platform motions to estimate turbulent kinetic energy (TKE) and TKE dissipation rates. Both of these quantities are correlated with wave steepness, which has been previously shown to determine wave breaking within the same dataset. Estimates of the turbulent length scale increase linearly with distance from the free surface, and roughness lengths estimated from velocity statistics scale with significant wave height. The vertical decay of turbulence is consistent with a balance between vertical diffusion and dissipation. Below a critical depth, a power law scaling commonly applied in the literature works well to fit the data. Above this depth, an exponential scaling fits the data well. These results, which are in a surface-following reference frame, are reconciled with results from the literature in a fixed reference frame. A mapping between free-surface referenced and mean-surface reference coordinates suggests 30% of the TKE is dissipated above the mean sea surface.

Lastly, wind, wave, turbulence, and ice measurements from the Arctic Marginal Ice Zone are used to evaluate the response of the ocean surface to a given wind stress, with a focus on the local wind input to waves and subsequent ocean surface turbulence. Observations are from the Beaufort Sea in the summer and early fall of 2014, with fractional ice cover

of up to 50%. Observations showed strong damping and directional modification of short waves, which, in turn, decreased the wind energy input to waves. Near-surface turbulent dissipation rates were also greatly reduced in partial ice cover. The reductions in waves and turbulence were balanced, suggesting that a wind-wave equilibrium is maintained in the marginal ice zone, though at levels much less than in open water. These results suggest that air-sea interactions are suppressed in the marginal ice zone relative to open ocean conditions at a given wind forcing, and this may act as a feedback mechanism in expanding a persistent marginal ice zone throughout the Arctic.

TABLE OF CONTENTS

LIST OF FIGURES

LIST OF TABLES

ACKNOWLEDGMENTS

My advisor, Jim Thomson, deserves a thousand thank-you's. On my very first day working with Jim, there was an accident that he described then as "the low point of his career." These moments of extreme stress and uncertainty have an uncanny ability to expose peoples truer, baser selves. And in that moment, Jim carried himself with grace, and demonstrated his dedication to those around him. Working with Jim for the past five years has only reinforced what I saw then. Jim, you are leader in the deepest sense, thank you for your inspiration, enthusiasm, guidance, and seemingly inexhaustible commitment to the lab.

I have the pleasure of calling Britt Raubenheimer and Steve Elgar my former bosses. They hired me out of undergrad and introduced me to ocean science. Their passion is infectious, and they always found a way to make work fun. Thank you for your continued mentorship. I wouldn't be here if it weren't for you.

My committee, Alex Horner-Devine, Tim Janssen, and Luc Rainville, have all been spectacular. They offered insight and guidance on my work and academic progress for which I am eternally grateful. Thank you for taking time out of your impossibly busy schedules to help me.

Alex De Klerk and Joe Talbert made all of the field work possible with their long hours, technical genius, and sometimes shear force of will. On top of it, they always manage to stay grounded and crack jokes at exactly the right times. Outside of the lab, you both have helped teach me about woodworking, boats, engines and outdoor skills, and for that I can't thank you enough.

The Office of Naval Research provided funding for my work under the DARLA, and MIZ

programs. The biweekly DARLA group meetings helped shape much of my early work, and I am grateful for all the feedback provided there.

Thank you to the EFM group, past and present. I looked forward to Thursdays every week I was at UW. Being able to nerd out about fluid mechanics in a safe space kept me sane and gave me purpose. In that regard, my officemates deserve special recognition. Chris, J. Paul, Maddie, Maru, Mike, and Roxanne, I could not have done this without all your help on homework, coding problems, and understanding difficult concepts. You were always being willing to spend a day on the whiteboard instead of 'working' (and thank you for putting up with my bad dad jokes).

To all of my friends outside of the lab, you are too many to list and thank individually without another 150 pages of space. But thank you for all the laughs and hugs, for helping me to be a better person, and for pushing me to do more.

An unbelievable amount of support came from my family. I don't know what I would do, or who I would be without them. Laura, thank you for always looking out for your little brother. Your strength and stubborn tenacity is something I aspire for. And to my parents, thank you for everything.

DEDICATION

to my family, for your love and support

Chapter 1

INTRODUCTION

1.1 Motivation

River inlets are common, complex coastal features that mediate important exchanges between land masses and the ocean. These gateways are often highly populated, and frequently trafficked for commerce and recreation. Ocean waves traveling into these regions from deeper water bring momentum and mechanical energy, and are modified by a complex system of currents and bathymetry. When these waves break, they are a danger to commercial and recreational vessels operating in the area. Breaking waves also convert energetic wave motions into turbulence at the ocean surface. Wave-breaking turbulence, and its relation to the fate of land sourced sediments, pollutants, biota and nutrients carried with the fresh river water is poorly understood. However, these terrigenous sediments and tracers are important to the ecology of the larger coastal area.

In contrast, Marginal Ice Zones (MIZs) are remote, but still ecologically sensitive and globally relevant regions. The MIZ is defined as the transition between the open ocean and a dense ice pack, and is characterized by floating, disconnected ice floes. Open ocean waves traveling into the MIZ are modified by ice floes, altering the exchanges of heat and momentum across the air-ice-ocean interface. Wave motions can break larger ice floes into smaller pieces, increasing the total ice surface area which could accelerate ice melt. These wave-driven processes help determine the motion, melting and freeze-up of sea ice, but their overall effect has yet to be fully characterized.

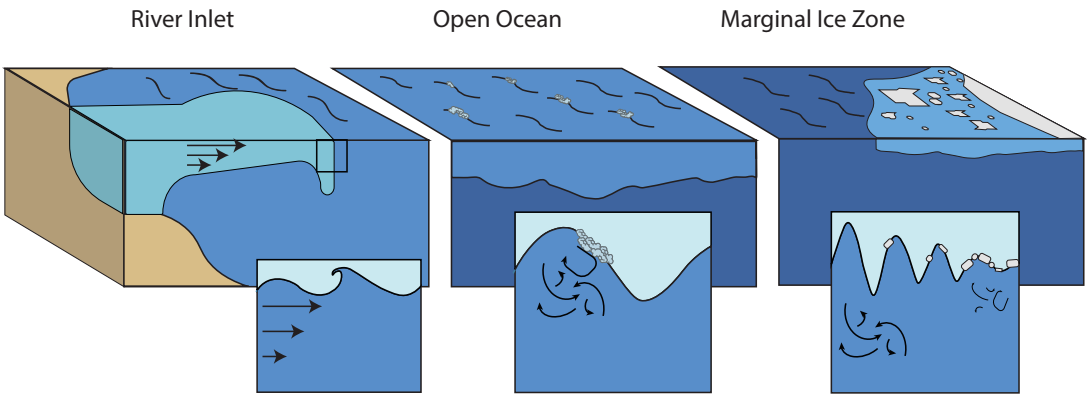

Figure 1.1: Open ocean waves (center) break because of local winds, creating turbulence very near the surface. Waves from the open ocean are modified by currents and bathymetry at river inlets (left), changing the intensity and location of breaking and the resulting turbulence. Waves from the open ocean traveling into the MIZ (right) are damped and scattered, decoupling the wind and the wave field and reducing turbulence.

The goal of this work is to better understand how open ocean waves and related surface processes are modified by currents at river inlets, and ice in the MIZ. A schematic overviewing the regions and wave processes is shown in Figure 1.1. The data used here are from two field campaigns, one at the Mouth of the Columbia River in 2013, and the other in the Arctic Marginal Ice Zone in summer 2014. The majority of observations were taken from surface following buoys designed to measure waves, currents, and turbulence. The non-Eulerian reference frame allows for measurement of turbulence inside wave crests, offering a novel glimpse into air-sea processes.

1.2 Ocean Waves

Surface gravity waves are translational oscillations propagating on the ocean-air interface. A typical water wave is described by its frequency, f, and its amplitude, a (or height, $H = 2a$), and its wavenumber, k. Wave frequency is defined as the inverse of the wave period, T^{-1}, or the rate of crests per unit of time. Higher frequency waves are closer together in time, and lower frequency waves occur with more time between wave crests. Sometimes these are also referred to as shorter and longer waves respectively, because higher frequency waves are also shorter in length. Rather than use length, it is conventional to use wavenumber, defined as 2π multiplied by the inverse of the wave length, to describe an ocean wave's spatial scale because it makes an easier analogous scale to frequency. That is to say, high frequency waves are shorter, and therefore will also have higher wavenumber. Wave amplitude is defined as the distance from wave crest to the mean water line. Wave height is then the crest to trough vertical distance, for a sinusoidal wave this is twice the amplitude.

Anyone who has spent time watching the ocean often balks at the sinusoidal description of waves, and rightly so. The complicated surface we see when looking out over large bodies of water almost never resembles a sinusoid with a single frequency and amplitude. We call these idealized sinusoids regular waves, while the complex ocean surface patterns that are a mix of many different wave frequencies, amplitudes, and directions are called irregular waves. It can, in fact, be difficult to describe irregular waves mathematically. One useful method is spectral analysis, which takes advantage of the fact that any time series can be represented as an infinite sum of sinusoids. Using this property, the sea surface elevation η at a single point in space at time t, can be expressed,

$$\eta(t) = \sum_n a_n \cos(\sigma_n t + \phi_n), \tag{1.1}$$

where $\eta(t)$ is the sea surface deviation from a mean waterline reference, a_n is the amplitude, $\sigma_n = 2\pi f_n$ is the wave intrinsic frequency, and ϕ_n is a phase. The subscript n represents a

single component, which is the idealized regular sinusoid. Therefore, applying a Fast Fourier Transform (FFT) to an ocean elevation time series yields a description of the amplitudes a_n and frequencies σ_n. It is more conventional to analyze the power spectrum, which gives squared amplitudes and frequency, but not phases ϕ. In part, this is because the squared amplitude is related to the wave energy density (the sum of kinetic and potential energy) which is,

$$E = \rho g \langle \eta^2 \rangle = \frac{1}{2} \rho g a^2, \tag{1.2}$$

where ρ is the density of water, g is acceleration due to gravity, $\langle\rangle$ represents a time average, and $\langle \eta^2 \rangle = (1/2)a^2$ holds for sinusoidal waves. Therefore, the power spectrum of a time series of ocean surface elevations can define the energy of each frequency component, $E(\sigma)$, and conservation laws can be used to model and track these wave components.

1.2.1 Conservation of Wave Action

Different from many physical systems, it is simpler to track wave action, which is defined $N = E/\sigma$, than it is to track energy [*Bretherton and Garrett*, 1968]. The radiative transfer equation describes the conservation of wave action, and is at the heart of modern operational wave models. In a simplified form, it can be written,

$$\frac{dN}{dt} + \nabla \cdot N(\mathbf{C_g} + \mathbf{u}) = S/\sigma, \tag{1.3}$$

where $\mathbf{C_g} = \partial\sigma/\partial\mathbf{k}$ is the group velocity, or the speed of energy propagation, $\mathbf{u}$ is a non-wave induced water velocity, and ∇ represents horizontal derivatives. S represents numerous source and sink terms that describe wave growth from wind, wave dissipation from breaking and friction, and non-linear interactions which can transfer energy between frequencies. Much of the challenge and progress in recent years has been appropriately and efficiently parameterizing the terms in S in a way that well represent physics, are easy to compute, and give accurate predictions of wave heights and frequencies.

1.2.2 Dispersion

Dispersion is a fascinating property of ocean waves, and one that distinguishes them from other physical waves like light, and sound. Put simply, long ocean waves travel faster. Therefore, when waves at many different frequencies are formed (such as during a storm) the longer waves outrun the shorter waves, and the waves spread apart or disperse (and thus the name). Mathematically, dispersion is described,

$$C = \frac{\sigma}{k} = \frac{g}{\sigma}\tanh(kd), \tag{1.4}$$

where C is the wave phase speed (the speed of wave crests), d is the water depth, and tanh() is the hyperbolic tangent function. In deep water kd is large, the tanh function asymptotes to unity, and the wave speed is an inverse function of frequency. Therefore, long waves (with small frequency) travel faster in deep water. In shallow water kd is small, and $\tanh(kd) \approx kd$ so that the wave speed depends only on depth and gravity.

1.2.3 Wave Modifications by Currents

Ambient ocean currents complicate the dispersion relation. The speed of wave crests relative to an Earth stationary reference frame, denoted the absolute reference frame, becomes $\mathbf{C}+\mathbf{u}$. This is more commonly depicted in terms of wave frequency,

$$\omega = \sigma + \mathbf{u}\cdot\mathbf{k}, \tag{1.5}$$

where ω is the absolute frequency, and $\sigma = \sqrt{gk\tanh(kd)}$ is the intrinsic frequency (from equation 1.4). Therefore the current induces a frequency shift, $\mathbf{u}\cdot\mathbf{k}$, which depends on wavenumber and the wave direction relative to the current. When the ocean current is not uniform vertically (i.e., there is vertical shear), it is less clear what value to use for $\mathbf{u}$. This sheared dispersion is a large focus of Chapter 2, which contains a more thorough review of previous work on this topic.

When the ocean current is equal to the wave group velocity (the energy propagation velocity) the wave cannot propagate upstream and is called a blocked wave. From equation 1.3 we can see this causes a problem. If the waves are stationary, and sources and sinks are zero, the one dimensional case reduces to $\frac{dN}{dx}(C_g + U) = 0$. Therefore, as $C_g + U$ approaches zero, the wave action must become infinitely large, clearly an unphysical result. In reality, the source/sink terms can no longer be zero here. Often, wave breaking occurs to limit the wave height and non-linear transfers occur, which put energy at different frequencies (and thus different wave speeds). Still, wave models do poorly in these regions, often predicting wave heights much too large due to an insufficiently large dissipation relative to this rapid increase in wave height.

When currents differ over a horizontal distance, waves can be turned, or refracted. The absolute wave crest speed, $C + U$ is changed inside the current, but not just outside of it. Therefore, one part of the wave outruns the other, forcing the wave to turn. For an opposing current jet, like those found at river inlets on ebbing tides, waves are focused into the region of opposing currents. This compounds with shoaling and blocking effects to make an extremely hazardous region.

1.2.4 Wave-Ice interactions

The effect of ice on waves is strongly dependent on ice type, geometry, and spacing, which can change over relatively short space and time scales. Newly formed, or actively freezing grease ice creates a thin near-surface viscous (sometimes described as soupy) layer, and is often accompanied by closely spaced small disks of ice called pancakes. Older, fractured ice floes called brash ice tend to be larger, irregular shapes that often have larger spacing than pancakes. Some longer waves can propagate far into the ice field reaching nearly continuous ice sheets. It is difficult to identify ice type from remote sensing products, however, and most reported ice products only report a sea ice extent or the fraction of ice cover over a

spatial area (e.g. AMSR2 products, *Spreen et al.* [2008]), making regional treatment of these ice types difficult in wave models. Further, due to the difficulty of gathering wave data in polar regions, a very limited set of field validations exists. Still, considerable progress has been made recently on constraining and implementing the wave/ice source sink term(s) S_{ice} [*Rogers and Zieger*, 2014].

The in-ice measurements presented in this thesis were located in a brash ice field, the effects of which will be highlighted here. Brash fields are often spaced such that free propagation of open water waves is possible between floes. Smaller waves are scattered, reflected, and/or refracted around ice floes creating a more directionally spread wave field. Waves are also damped, and although the exact physical mechanism is not yet determined, it is usually attributed either to turbulence created from shear on the ice floe boundary, or from a mass loading (added surface pressure) effect. Therefore both conservative (scattering) and non-conservative (damping) effects are important. How these wave/ice effects modify other source/sinks (e.g., wind input and breaking dissipation) from open water is a large focus of Chapter 4.

1.2.5 Wave Breaking

Wave breaking is nearly as ubiquitous as ocean waves, as deepwater wind-driven whitecapping accompanies the formation of ocean waves, and depth limited surf-zone wave breaking occurs at nearly all ocean boundaries. Despite the prominence of wave-breaking, the process is still not well understood. It is non-linear and creates a multi-phase flow as the overturning wave crest entrains air as bubbles. This is also why the process is so important, this overturning enhances the transfer of gas and momentum between the atmosphere and the ocean, it dissipates energy from the ocean waves, and creates turbulence at the ocean surface.

Still, some progress has been made in predicting and describing the breaking process. An early theory presented by *Stokes* [1880] used a kinematic breaking criterion, defining

wave breaking as the wave particle speed exceeding the wave phase speed. This definition resulted in a maximum steepness of $H/L \approx 1/7$. This was extended to finite-depth waves by *Miche* [1944], who found $(H/L)_{max} = 0.142 \tanh(kd)$, and thus defined a breaking condition applicable to intermediate and shallow water waves. Many lab and field studies do not agree on a single limiting wave steepness [as reviewed by *Perlin et al.*, 2013], and the use of individual wave steepness as a predictor for the initiation of individual wave breaking has largely been refuted. Still, steepness is related the the non-linearity of waves, and bulk wave steepness is useful in describing wave breaking distributions. *Chawla and Kirby* [2002] defined a bulk breaking criterion similar to the *Miche* [1944] steepness,

$$\gamma = \frac{H_s k_m}{\tanh(k_m d)}, \tag{1.6}$$

where γ is the bulk wave steepness, $H_s = 4\sqrt{\int E(f)/(\rho g) df}$, and k_m is the energy mean wavenumber. Even this, though, has been a difficult line of analysis. For example, *Holthuijsen and Herbers* [1986] measured statistics from breaking and non-breaking events, finding very little difference in steepness between the two. More recent studies have elaborated on this effect. For example, *Schwendeman and Thomson* [2017] used stereo video to measure wave breaking events in deep water, and found that while wave slope is large before breaking events, the effect is spatially and temporally localized and thus difficult to capture effectively with a point measurement. While it is clear that wave-by-wave steepness is still problematic in its ability to predict breaking, bulk steepness parameters are still useful. Similar to the findings of *Holthuijsen and Herbers* [1986], *Thornton and Guza* [1983] measured individual wave heights in a surf zone, and found a range of individual breaker heights for a single water depth (and therefore a single γ). However, *Thornton and Guza* [1983] found that breaking statistics followed heuristic distribution that could still be described with H_s/d.

1.2.6 Wave Dissipation

Wave dissipation, the energy lost from the wave field, is primarily due to wave breaking. Historically, shallow water and deep water (whitecapping) dissipation source functions have been treated separately. Deep water dissipations are functions of wave steepness but until recently have largely been heuristic, and tuned to correctly balance wind input. Recent work has better related these deep water functions to more closely resemble breaking measurements [e.g., *Ardhuin et al.*, 2010].

Shallow-water wave-breaking dissipation functions are primarily based on the bore model, where a breaking wave is related to a hydraulic jump which has an analytic energy dissipation function based on the difference in water elevation. By relating the vertical length scale in a hydraulic jump to a wave height, an energy dissipation function per wave crest can be developed. This function is then integrated with a breaking wave height distribution to estimate the total wave energy dissipation rate,

$$D_{brk} = \int_0^\infty P_b(H) D'_{brk}(H) dH, \tag{1.7}$$

where $P_b(H)$ is the probability distribution function of breaking waves, D'_{brk} is the dissipation of a wave of height H, and D_{brk} is the total depth limited breaking dissipation of the wave field. Variations on these dissipation functions employ different vertical scales in the bore model, modifying D'_{brk} [e.g., *Chawla and Kirby*, 2002], or report different probability distributions for breaking wave heights $P_b(H)$ [e.g., *Battjes and Janssen*, 1978; *Thornton and Guza*, 1983; *Filipot et al.*, 2010]. Applications to spectral models must partition this dissipation amongst frequency components, and typically each spectral component is reduced by a consistent fraction, $S_{brk}(\sigma) = (D_{brk}/E_{tot})E(\sigma)$.

As of yet, a budget tracking the pathway of energy from wave-breaking to other mechanical systems has not been closed. A large fraction of the energy is used to create and submerge bubbles, as much as 50% [*Lamarre and Melville*, 1991], and to eject spray into the atmo-

sphere. The creation of these bubbles and spray significantly enhance gas exchange between atmosphere and ocean [*Deike et al.*, 2017]. Another pathway for wave dissipation energy is into oceanic turbulence, created directly from velocity shear made by the overturning wave crest.

1.3 Turbulence Basics

Turbulent flows are important in their ability to effectively mix fluids, including chemical properties like salinity, heat, as well as mixing momentum. These types of flows are very non-linear due the the advection (or convection) of fluid, which makes them difficult to study and model directly. Often turbulent flows are separated into a time averaged component and a fluctuating component in what is called the Reynolds decomposition,

$$U(\mathbf{x},t) = \langle U(\mathbf{x},t)\rangle + u(\mathbf{x},t). \tag{1.8}$$

The mean flow can then be modeled by applying this decomposition to the the Navier Stokes equations. The basic form of the Reynolds Averaged Navier Stokes (RANS) equations is,

$$\frac{D\langle U_j\rangle}{Dt} = \frac{1}{\rho}\frac{\partial}{\partial x_i}\left[\underbrace{\mu\left(\frac{\partial\langle U_i\rangle}{\partial x_j}+\frac{\partial\langle U_j\rangle}{\partial x_i}\right)}_{\text{Viscous Stress}} - \underbrace{\langle p\rangle\delta_{ij}}_{\text{Isotropic (Pressure) Stress}} - \underbrace{\rho\langle u_i u_j\rangle}_{\text{Reynold's Stress}}\right], \tag{1.9}$$

where the terms on the RHS are the viscous stress, the pressure forcing, and the Reynolds stresses. The Reynolds stresses arise from the fluctuating component of the advective term in the material derivative. The addition of the Reynolds stresses creates a closure problem, because the tensor $\langle u_i u_j\rangle$ is unknown, and no new equations have been added. Therefore parameterization of this term has been the subject of extensive study in turbulence research. A large class of these parameterizations used extensively in geophysical flows are turbulent kinetic energy (TKE) models (one and two equation models), which use the idea of a turbulent viscosity to model Reynolds stresses. In these models the mean velocity shear multiplied

by the turbulent viscosity, ν_t, is used to define the Reynolds stress. A common way to parameterize the turbulent viscosity is with the square root of the TKE and a length scale. Therefore, these models also track the TKE with a transport equation,

$$\frac{Dq^2}{Dt} = -\nabla \cdot T + \mathcal{P} + B - \epsilon, \tag{1.10}$$

where q^2 is the TKE, T represents turbulent transport, $\mathcal{P}$ is production of TKE, B is buoyant production/destruction, and ϵ is the TKE dissipation rate. This is the so called 'one equation' model, which is closed with definition of T, B and ϵ. Two equation models define a second transport equation either for ϵ (and thus are called k-ϵ models) or a transport equation for turbulent frequency $\omega_t \equiv k/\epsilon$ (so called k-ω models). Note, convention in the turbulence community is to use k for TKE, which we distinguish from ocean wavenumber by using q^2 for TKE.

1.3.1 The Energy Cascade

In turbulent flows, motions at both large and very small scales are important, and capturing all of these scales of motion in measurements or models is difficult. At the largest scales of motion, shear (velocity differences across space) creates TKE (this is encapsulated in the production term, $\mathcal{P}$, in equation 1.10). Velocity motions are transferred to smaller scales as larger eddies break up and become smaller eddies. This process continues recursively until the smallest scales of motion where viscous effects become important, and energy is transferred into heat. This process of transferring turbulent energy to successively smaller scales is called the energy cascade. The pioneering work of *Kolmogorov* [1941] helped constrain flows across this large range of scales. *Kolmogorov* [1941] proposed three hypotheses, first, that the smallest scales of turbulent motion are statistically isotropic, second, that the smallest scales of motion are uniquely determined by the viscosity and the dissipation rate, and third, that there exists an intermediate range of scales (between the largest, energy containing eddies, and the smallest scales mentioned in the second hypothesis) that are uniquely determined

by the dissipation rate, independent of viscosity. This partitions turbulent scales into three ranges, the smallest scale is called the dissipative range and is where turbulent motion is turned into heat because of viscous effects. The intermediate range is called the inertial subrange, where viscous effects are negligible, but the transfer of energy from larger scales to smaller scales is set by inertia. The largest scales of motion are called the energy containing range.

The size of eddies in the dissipative range, by these hypotheses, must scale as $\eta_t = (\nu^3/\epsilon)^{1/4}$. With the molecular viscosity of water $\nu \approx 10^{-6}$, it is clear that these scales are minuscule, and are one reason turbulence can be difficult to include in any computer model, or to measure directly. The velocities in the inertial subrange can be scaled as $u' = (\epsilon k_t)^{1/3}$ where k_t is a turbulent wavenumber. The power spectrum of velocities in this range then must scale with the TKE dissipation rate, and turbulent wavenumbers,

$$S(k) \propto \ell u'^2 = k_t^{-1} \left(\epsilon/k\right)^{2/3} = \epsilon^{2/3} k_t^{-5/3}. \tag{1.11}$$

Measurements of turbulent flows are therefore often assessed through the power spectrum of velocity. Measured velocities in the inertial subrange can be used to estimate the TKE dissipation rate, and if velocities are measured at small enough k_t (larger scales, and thus including the energy containing range), the total TKE can be established. Therefore, measurement the velocity power spectrum (and therefore of both q^2 and ϵ) considerably constrain equation 1.10.

1.3.2 Wave-breaking Turbulence

Wave-breaking turbulence received attention when it was tagged as a potential player for determining mixed layer depths which are (still) not predicted well [*Belcher et al.*, 2012] but are important for global heat budgets. Oceanic turbulence is created at the surface boundary in the wave breaking process, and therefore is linked to the wave-breaking energy dissipation. However, since the deep-water wave-breaking dissipation term has been largely

used as a tuning knob for wave models, turbulence models often take this source directly from wind stress. This is loosely justified using *Phillips* [1985], where the wind source term is balanced by wave dissipation and (energy conserving) non-linear transfers. Thus, the total energy dissipated by the waves can be equated to the total energy input into waves from wind. This provides a surface boundary flux of turbulence. Within a few wave heights of the surface, TKE dissipation rate is balanced by vertical transport, $\nabla \cdot T = -\epsilon$, with shear production being relatively small [*Craig and Banner*, 1994]. Using these definitions, wave-breaking turbulence was shown to be effective at mixing thinner mixed layers in two equation turbulence models [e.g., *Noh and Jin Kim*, 1999], however it does not fully explain the discrepancies in measured and modeled mixed layer depths globally [*Belcher et al.*, 2012]. Therefore, work on vertical mixing for deeper mixed layers has shifted to other processes (e.g., Langmuir turbulence and the Craik-Leibovich vortex force), while wave-breaking turbulence still remains relevant in regions where buoyancy gradients exist very near the surface, such as river inlets and in the MIZ (Figure 1.1).

Surface waves and related surface fluxes are modified by strong currents and bathymetry at river inlets and by ice in the MIZ. Therefore, it's unclear how to apply much of the work that has focused on deep water wave-breaking, and whether or not many of the same assumptions apply. For example, the surface flux of turbulence is likely enhanced beyond the total wind input at river inlets, as bathymetric and current effects can significantly enhance wave dissipation, and wave/ice interactions likely reduce the wind input and resulting turbulence.

In deepwater, wave-breaking TKE dissipation rate is typically scaled as

$$\frac{\epsilon H_s}{G} = A \left(\frac{z}{H_s} \right)^{-2}, \tag{1.12}$$

where G is the surface flux of TKE, and H_s is the significant wave height [*Terray et al.*, 1996]. This scaling has been validated in a number of subsequent field and lab studies, but has not been extensively tested outside of deep water, open ocean conditions.

1.4 Prior work

Work on wave breaking, wave dissipation, and turbulence from measurements at a river inlet in North Carolina were used in the author's Masters Thesis [*Zippel*, 2014], and later submitted for publication in JGR:Oceans. During the review process, significant changes were made to the work, some of which will be outlined here. The full citation for the article is,

> Zippel, S., and J. Thomson (2015), Wave breaking and turbulence at a tidal inlet, J. Geophys. Res. Oceans, 120, 1016-1031, doi:10.1002/2014JC010025.

SWIFT drifters, were deployed at New River Inlet (North Carolina) between April 26th and May 21st, 2012. The SWIFTs measure wind, location, drift speed, waves, turbulent dissipation rate, and take images (for wave breaking estimates). Bathymetry data was collected by the Army Corps FRF LARC survey system on May 2nd, 2012. Reported water depths were corrected for tides using a pressure gauge. Surface currents and positions were estimated as the 5-minute averages of GPS time series of velocity and position, respectively. The study focused on 11 drifts, where images were manually reviewed for the presence of breaking waves.

Figure 1.2 evaluates four different wave dissipation models using observed energy flux gradients. The wave-dissipation parameterizations are based on the bore model, where *Battjes and Janssen* [1978], updated in *Janssen and Battjes* [2007] (hereafter JB07) and *Thornton and Guza* [1983] (hereafter TG83) mainly differ in the treatment of the breaking wave height distribution function. Both of these models are updated for the effects of currents through modifying the bore model height scaling, and the breaking parameter in *Chawla and Kirby* [2002], and are hereafter refered to as CK1 and CK2 (A full description of the parameterizations is provided in *Zippel and Thomson* [2015]). The models were not tuned, and used arbitrary constants $\gamma = 0.4$ and $\beta = 0.5$. The current adjusted models from *Chawla and*

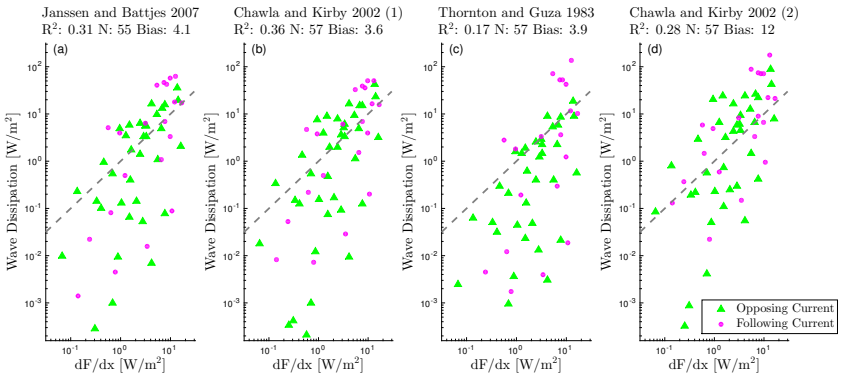

Figure 1.2: The four wave dissipation models (Section 1.2) are shown against estimates of wave energy flux gradients. The grey dashed line represents 1:1. The models were not tuned, and used arbitrary constants $\gamma = 0.4$ and $\beta = 0.5$. Green triangles represent data taken when waves oppose currents. Magenta circles show data when waves follow currents. The CK1 model has the best skill, $r^2 = 0.36$ and lowest bias, 3.6 [W/m^2]. All wave models are biased high when compared to measurements. Errors in the measurement based wave energy flux gradient estimates are as large as 50% of the estimate. However, the estimates are still useful in evaluating the models because the range of values span two decades.

Kirby [2002] showed slightly improved correlations with observations when compared their depth-only dependent counterparts ($r^2 = 0.31$ to $r^2 = 0.36$, and $r^2 = 0.17$ to $r^2 = 0.28$). However, the current adjusted model CK2 increased bias, significantly overestimating wave energy dissipation. This bias can be corrected by using a much lower β, but the required tuning would be unphysical. In addition, the JB07 based models show better correlation with the measured flux gradients than the TG83 based models ($r^2 = 0.31$ and $r^2 = 0.36$ compared to $r^2 = 0.17$ and $r^2 = 0.28$). The generally low correlations of all models are attributed to errors in observed energy flux gradients of up to 50%. However, the estimated energy flux gradients spanning two orders of magnitude are still useful in showing general trends in the models.

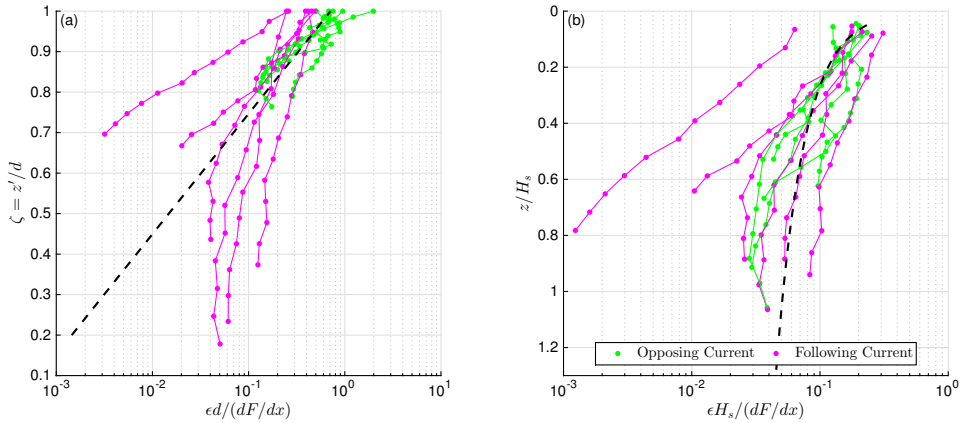

Figure 1.3: Turbulent dissipation rate scalings from **(a)** the exponential *Feddersen* [2012b] scaling, and **(b)** the modified *Terray et al.* [1996] power law scaling. Points where currents oppose waves are shown in green. Following waves and currents are shown in magenta. Of the 14 profiles for which two or more breakers were identified per 5 minute burst, 11 had a forward differenced flux gradients $\mathrm{d}F/\mathrm{d}x$ that passed quality control. Each distinct profile has 13 dissipation estimates for a total $N = 143$. Because the *Terray et al.* [1996] scaling is undefined at $z' = 0$, surface dissipation measurements are not used in the fit (N = 132). The exponential scaling has a greater correlation, with $r^2 = 0.54$ for the *Feddersen* [2012b] scaling compared to the $r^2 = 0.48$ for the *Terray et al.* [1996] scaling. Non-linear fits are found using MATLAB's *fitnlm* function.

Non-dimensional profiles of the turbulent dissipation rate for measurements where breaking was observed with cameras are shown in Figure 1.3. Panel (a) is the exponential surf zone scaling derived by *Feddersen* [2012b]. Panel (b) is the power law scaling introduced by *Terray et al.* [1996] and adapted to the surf zone by *Feddersen* [2012b]. For each, the gradient of wave energy flux, $\mathrm{d}F/\mathrm{d}x$, is used to normalize the profiles. Of the 14 bursts with two or more breaking waves per 5 minute burst ($n \geq 2$), 11 passed quality control ($\mathrm{d}F/\mathrm{d}x < 0$). Surface dissipation rates ($z = 0$) were excluded from the *Terray et al.* [1996] estimates, because the scaling asymptotes at the surface. Best fit curves were found using MATLAB's *fitnlm* function. By fitting each burst individually, errors in wave energy flux gradients are absorbed into the fitting parameters A_F, and A_T. However, because each profile has a small number of points ($n = 13$), the best fit parameters to all 11 bursts are plotted in Figure 1.3.

The exponential scaling by depth had improved skill over the power law scaling by wave height ($r^2 = 0.54$ compared to $r^2 = 0.48$). The exponential scaling was especially skillful for the individual following wave-current cases ($r^2 \geq 0.95$) when compared to the opposing cases ($r^2 \geq 0.87$). The best fit exponent for the power law scaling was $\lambda = -0.50$, which does not agree with the literature, where typically $\lambda = -2$ is found. By contrast, the two parameters in the *Feddersen* [2012b] scaling, α and A_F, were similar to the reported values in *Feddersen* [2012b]. Using the best fit for all data, $\alpha = 7.7$ gives a theoretical $\tilde{A}_F = 0.0035$. The implied percent of wave dissipation to TKE dissipation is then $A_F/\tilde{A}_F = 0.089$, or 8.9%, similar to the 15% found in *Feddersen* [2012b].

While individual profile fits for the exponential scaling are more skillful with following currents, there is less variation between profiles with opposing currents such that correlations with all the opposing current points are larger than all the follow current points ($r^2 = 0.59$, to $r^2 = 0.52$). The decay scale for the best fit of the opposing current cases is more than twice that of the following current cases: $\alpha = 9.4$, compared to $\alpha = 4.4$. However, the implied wave dissipation to TKE dissipation ratio is similar between opposing and following

cases (9.9% and 8.0% respectively).

Turbulence profiles in Figure 1.3a qualitatively follow the exponential scaling closely in the top 40% of the water column ($0.6 < \zeta \leq 1$), however scaled values in the lower water column deviate from the expected scaling. It is possible that the exponential scaling, which assumes a constant turbulent length scale, breaks down near the bottom boundary layer where turbulent length scales are typically assumed to increase linearly from the bed. *Feddersen* [2012b] found good agreement with the exponential scaling near the bed, but used observations with mean velocities to $U < 0.3$ m/s, where here surface velocities are $U \geq 0.6$ m/s. Breaking on opposing wave and currents was measured in deeper water, and therefore this effect is only seen for following wave and current cases. *Jones and Monismith* [2008] found the wave affected surface layer transitioned directly into the bottom boundary layer in an estuarine embayment, with the transition typically in the bottom 10% of the water column. The much higher transition depth suggested by Figure 1.3a could be due to larger currents, however an estimate of bottom shear cannot be made from SWIFT observations, and therefore the expected transition depth proposed in *Jones and Monismith* [2008] is not quantified in this study.

1.5 Thesis Outline

Measurements from the MCR cruise and the MIZ cruise are presented in the following chapters. Chapter 2 evaluates the effect of strong sheared currents on dispersion, and the resulting wave steepness. The relation of this current dependent steepness to wave breaking statistics are discussed, and a number of wave breaking models are tested against data. The chapter has been reproduced with minor changes from,

> S. Zippel, and J. Thomson. Surface wave breaking over sheared currents: Observations from the Mouth of the Columbia River. J. Geophys. Res. Oceans, 122, 3311-3328, 2017. doi:10.1002/2016JC012498.

Chapter 3 presents turbulence measurements from the mouth of the Columbia River. Wave-breaking turbulence measurements are used to better constrain one and two equation model constants. The effects of wave-breaking turbulence on breaking layers, and the effects of reference frame are discussed. The contents of this chapter have been submitted to the Journal of Physical Oceanography for publication,

> S. Zippel, J. Thomson, and G. Farquharson. Turbulence from breaking surface waves at the mouth of the Columbia River, J. Phys. Oceanogr. (In Revisions)

Chapter 4 presents measurements from the Arctic Marginal Ice Zone and shows how waves are modified by the ice, and discusses the implications of this on near surface turbulence. The chapter is adapted from the article,

> S. Zippel, and J. Thomson. Air-sea interactions in the marginal ice zone, Elem Sci Anth., 4:95, 2016. doi: http://doi.org/10.12952/journal.elementa.000095

Lastly, Chapter 5 provides a summary, and a discussion of future directions on these topics.

Chapter 2

SURFACE WAVE BREAKING OVER SHEARED CURRENTS: OBSERVATIONS FROM THE MOUTH OF THE COLUMBIA RIVER

2.1 Introduction

Wave breaking and wave-current interaction at tidal and river inlets has been historically difficult to predict and understand. The effect of currents on waves is commonly smaller than the effect of bathymetry on waves, and this makes measurements of wave-current effects in the field difficult to discern from changes in tidal elevation [*Kang and Iorio*, 2006; *Olabarrietta et al.*, 2011; *Olabarrieta et al.*, 2014; *Mendez et al.*, 2015; *Chen et al.*, 2015]. Despite being a secondary effect, understanding and incorporating the effects of currents on waves is important to understanding river inlet systems. For example, *Olabarrieta et al.* [2014] modeled a simplified river inlet system, showing that jet instability was increased due to the interaction of large waves with high outflow. In another study at a lagoon in Portugal, *Dodet et al.* [2013] showed enhancement of wave heights and wave dissipations on ebbs, as well as a reduction of wave heights on floods as a result of wave-current interactions. Further, *Dodet et al.* [2013] noted that incorporating wave-current feedback in model simulations added an ebb/flood asymmetry that decreased seaward transport of sediment in the tidal channel on ebbs.

Farther from the coast, refraction of waves by currents can effect how and which waves propagate to inlets. *Hopkins et al.* [2015] used models and measurements at Katama Inlet on Martha's Vineyard to show that wave refraction by currents is important for accurate prediction of waves offshore of the surf zone. *Pearman et al.* [2014] showed strong refraction

and steepening of wind waves in drifter measurements at the San Francisco Bight. In a separate study of the San Francisco ebb tidal delta, *Hansen et al.* [2014] showed wave refraction (in this case due to a combination of bathymetry and currents) created large along shore pressure gradients offshore of the surf zone.

Wave/current effects in deep water can potentially affect buoyant plumes, as wave breaking has been suggested as a mechanism for enhanced river plume mixing. *Gerbi et al.* [2013] modeled a buoyant river plume during upwelling-favorable winds, finding the plume was thicker when a wave breaking turbulence parameterization was included. *Thomson et al.* [2014] showed near surface turbulent kinetic energy dissipations due to wave breaking at a front formed by the Columbia River plume were larger when short waves were present, possibly causing a thicker plume than was observed on an adjacent day without short waves.

While currents affect waves through refraction and steepening, wave breaking has an effect on currents through turbulence injection into the ocean surface [*Craig and Banner*, 1994; *Terray et al.*, 1996], and through wave-breaking induced radiation stress gradients [*Longuet-Higgins and Stewart*, 1962]. Therefore, better understanding of wave breaking at river inlets can lead to improvements in prediction of not only the waves themselves, but of currents, water quality, and sediment transport.

Wave breaking also poses a hazard to marine traffic. River inlets are often both active areas for vessels, and dangerous to navigate [*Masson*, 1996]. Improved understanding of wave breaking at sites with strong currents could help improve safety in these complex, highly trafficked areas.

2.1.1 Wave Breaking Models

Wave breaking is often separated into two regimes based on the ratio of depth d and wavelength L: 1) deep water, where the ratio of depth to wavelength is $d/L > 1/2$, and 2) shallow water, where $d/L < 1/20$. Breaking at river inlets often occurs in intermediate depths, and

therefore models developed to include the effects of currents are often modified from either regime. However, because the deep and shallow models were developed separately, the wave-current breaking schemes often have fundamentally different approaches. Shallow models (e.g. *Battjes and Janssen* [1978]; *Thornton and Guza* [1983]) explicitly define breaking fraction from a probabilistic assumption of breaking wave heights. In contrast, deep models (e.g., *van der Westhuysen* [2012]) often skip explicit definition of breaking fraction in favor of direct estimates of wave dissipation modified from white capping or saturation models. As a result, these latter models will be discussed, but not directly compared with data in this study.

Battjes and Janssen [1978] developed one of the first wave-breaking models for the surf zone. They combined the steepness limit from *Miche* [1944], and the assumption that all waves with heights above this steepness limit in a Rayleigh distribution were breaking (i.e., a clipped wave height distribution), leading to a transcendental equation for breaking fraction,

$$\frac{1-Q_b}{\ln(Q_b)} = -\left(\frac{H_{rms}}{H_{max}}\right)^2, \tag{2.1}$$

where Q_b is the fraction of breaking waves to the total number of waves, and H_{rms} is the root mean square wave height. Using an approximation for the *Miche* [1944] steepness limit (as described in *Chawla and Kirby* [2002]), $H_{max}k_m/\tanh(k_m d) = \gamma$, the equation above can be restated as,

$$\frac{1-Q_{b,BJ78}}{\ln(Q_{b,BJ78})} = -\left(\frac{H_{rms}k_m}{\gamma\tanh(k_m d)}\right)^2, \tag{2.2}$$

where k_m is the mean wavenumber, d is the water depth, and γ is a constant prescribing the breaking limit. In this form, the breaking model is more easily applied to breaking waves outside of shallow water, although only a slight modification to the breaking limit (and not the clipped Rayleigh model) was made. This form of the breaking model is also more easily applied to breaking in the presence of currents, which alter the wavenumber k (see next section).

Thornton and Guza [1983] measured breaking wave heights in the surf zone, finding broken wave height distributions did not fit the assumptions of the clipped *Battjes and Janssen* [1978] model, but rather a range of broken wave heights existed, some much less than the steepness limit. Therefore, they suggested a heuristic breaking wave height distribution function by multiplying the Rayleigh distributed wave heights by a weighting function. *Chawla and Kirby* [2002] modified this function for breaking in intermediate depth with currents,

$$W(H) = a\left(\frac{H_{rms}k_m}{\gamma\tanh(k_m d)}\right)^n\left\{1-\exp\left[-\left(\frac{Hk_m}{\gamma\tanh(k_m d)}\right)^2\right]\right\}, \tag{2.3}$$

where here, $W(H)$ is the weighting function, and $n = 2$, and $a = 1$ are constants. Breaking fraction can be found through integration of the breaking wave height distribution,

$$Q_{b,CK02} = \int_0^\infty W(H)P(H)\mathrm{d}H = \left(\frac{H_{rms}k_m}{\gamma\tanh(k_m d)}\right)^4\left[\left(\frac{H_{rms}k_m}{\gamma\tanh(k_m d)}\right)^2 - 1\right]^{-1}, \tag{2.4}$$

where $P(H)$ is the Rayleigh distribution as a function of wave height, H. For the purposes of this study, evaluations of the wave breaking models will be done using H_s instead of H_{rms}, which results in an increase in γ by $\sqrt{2}$.

While deep water studies of wave breaking have often favored breaking metrics besides Q_b, (i.e., focused on whitecap coverage [*Monahan*, 1971; *Monahan and Muircheartajgh*, 1980; *Callaghan et al.*, 2008; *Schwendeman and Thomson*, 2015b], and more recently the breaking crest speed distribution $\lambda(c)$, e.g., *Gemmrich et al.* [2008]; *Thomson and Jessup* [2009]; *Kleiss and Melville* [2010]) there have also been studies of breaking fraction. *Banner et al.* [2000] examined breaking fractions for a collection of three different data sets, showing a frequency centered steepness $s = H_p k_p/2$ explained the trend of dominant wave breaking. Breaking fractions were fit to an exponential,

$$Q_{b,B00} = C_1(s - C_2)^{C_3}, \tag{2.5}$$

with, $C_1 = 22.0, C_2 = 0.055, C_3 = 2.01$. This model was intended to capture the dominant breaking, and thus the scale of breaking waves was determined in estimation of Q_b, and

considered for the steepness parameter s. For the purposes of this study, we extend the steepness parameter to include finite depths, and consider the exponential fit in both a mean sense ($s = H_s k_m / \tanh(k_m d)$) to better compare this heuristic fit to the aforementioned breaking models, and in the dominant wave band as originally intended.

More recently, *Filipot et al.* [2010] proposed a breaking model for use in all depth regimes, combining ideas from *Chawla and Kirby* [2002] and *Banner et al.* [2000] (amongst others), as well as extending the probabilistic bulk model to a quasi-spectral model. The *Filipot et al.* [2010] steepness parameter is similar to the *Chawla and Kirby* [2002] steepness, and is defined:

$$\beta_r = \frac{H_r(f_c) k_r(f_c)}{\tanh(k_r(f_c) d)}, \tag{2.6}$$

with $H_r(f_c)$ and $k_r(f_c)$ defined below.

The wave spectrum is sub-divided into four frequency bands related to the peak frequency, f_p. Bands are defined by a center frequency, f_c, at bands $f_c = [0.55, 1, 1.86, 3.45] \times f_p$, and a window width of $\delta = 0.6$. Parameters for wave height, H and wavenumber, k in each band are found through integration of the wave energy spectrum multiplied with a Hann windowing function, G. For example, significant wave height for a given band, $H_r(f_c)$, would be:

$$H_r(f_c) = \frac{\sqrt{2}}{4} \sqrt{\int_0^\infty G_{fc}(f) E(f) df}, \tag{2.7}$$

where here, G is the window function (Hann window) which is non-zero in the band of interest, about center frequency f_c. The characteristic wavenumber is defined similarly, $k_r(f_c) = \int G_{fc} E(f) k \mathrm{d}f / \int G_{fc} E(f) \mathrm{d}f$. *Filipot et al.* [2010] estimate and remove the amplitude of non-linear harmonics using an iterative method, as these nonlinear harmonics would result in overestimates of wave energy for frequencies above the peak.

The breaking rate for each band is found using a method similar to *Chawla and Kirby* [2002], via an integrated breaking wave height distribution. However, the parameters $a = 1, n = 2$ are changed from the values used in Equation 2.3, to $a = 1.5, n = 4$. The new

weighting function is:

$$W(H, f_c) = a \left[\frac{\beta_r}{\tilde{\beta}}\right]^2 \left\{1 - \exp\left[-\left(\frac{\beta}{\tilde{\beta}}\right)^n\right]\right\}, \tag{2.8}$$

where $\tilde{\beta}$ is the limiting steepness and $\beta = \beta(H) = kH/\tanh(kd)$. Originally, the limiting steepness is set to a fraction of the maximum linear steepness determined from an approximate stream function solution, $\tilde{\beta} = b \times \beta_{max,lin}$, where $b = 0.48$ and $\beta_{max,lin}$ is a third order polynomial of $\tanh(kD)$. For the purposes of this study, we simplify the parameterization to $\tilde{\beta} = 0.48$.

2.1.2 Wave-current interactions

Waves propagating over a current experience a shift of $\vec{U} \cdot \vec{k}$ in absolute frequency ω. Often, the current speed, U is taken as a depth averaged current [*Booij et al.*, 1999], or a surface current, and applied uniformly to all frequencies. However, vertical shear results in a modification to the wave-current interaction, based on the vertical distribution of the currents relative to the vertical distribution of wave motion (which attenuates with depth according to wavenumber). This can be approximated in a depth-averaged sense by using an effective current U_{eff}, such that the linear dispersion relation is,

$$\omega = \sigma_{intr} + \vec{U}_{eff}(k) \cdot \vec{k}, \tag{2.9}$$

where ω is the absolute (fixed reference frame) frequency and $\sigma_{intr} = \sqrt{gk\tanh(kd)}$ is the wave intrinsic frequency (reference frame moving at U_{eff}). A deep water approximation for U_{eff} was first presented by *Stewart and Joy* [1974], and extended to finite depth by *Kirby and Chen* [1989]. The effective current, U_{eff}, is defined to a first order as,

$$U_{eff}(k) = \frac{2k}{\sinh(2kd)} \int_{-d}^{0} U(z)\cosh(2k[d+z])\mathrm{d}z, \tag{2.10}$$

where z is the depth below the sea surface. Thus, shorter waves effectively experience the surface current, while longer waves experience a weighted average of the current profile based

on their length. This distinction between surface currents and the effective current for wave-current interaction is important, because measurements of waves using freely drifting buoys will be in a reference frame moving with the surface current, not the effective current.

Recent X-band radar measurements of waves have confirmed the analytic *Kirby and Chen* [1989] dispersion relation [*Lund et al.*, 2015; *Campana et al.*, 2016]. Using the radar-measured wavenumber, $\vec{k}$ and frequency, ω, the studies inverted the dispersion relation to estimate $U(z)$, and found estimated profiles compared favorably with acoustic doppler measurements.

2.2 Methods

The Columbia River Mouth, located on the Washington-Oregon border, is known for large swells, strong tidal currents, and complex bathymetry. The inlet entrance is roughly 3.5 km wide, and has been engineered with two jetties at the mouth (a third jetty was also constructed inside the river mouth), and a dredged shipping channel is maintained out the west facing inlet, turning southward. Previous studies have shown strong wave-current interactions at this site, using both remote sensing data [*Gonzalez and Rosenfeld*, 1984] and model simulations [*Kassem and Ozkan-Haller*, 2012]. Field measurements of waves and wave breaking have historically been sparse.

For the present study, data were collected at the mouth of the Columbia River between May and September of 2013 using SWIFT drifters (http://www/apl.uw.edu/swift). Bathymetry (survey data originally from *Gelfenbaum et al.* [2015]), and drift tracks are shown in Figure 2.1. On ebb tides, drifters were released inside the inlet and recovered offshore after 3-4 hours once the tide had changed to allow for safe passage across the Columbia Bar. On floods, the drifters were deployed inside the two jetties and kept within eyesight of the research vessel, or accompanying small boat. Drifters approaching shore were recovered and re-deployed in deeper water to avoid beaching. Drifters were deployed in pairs, commonly staying within a few hundred meters of each other over the course of their deployments.

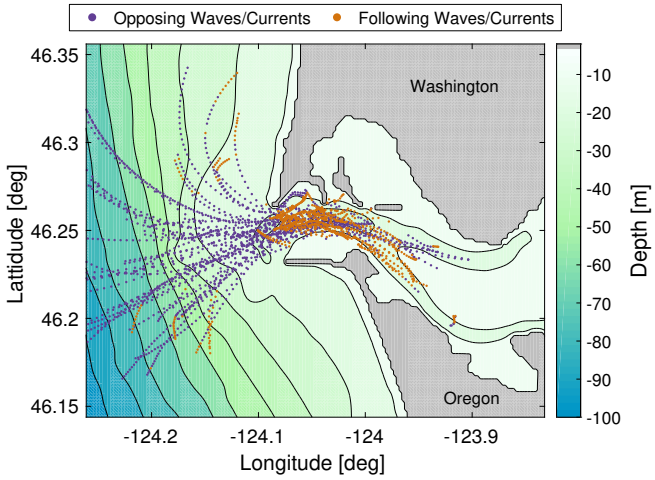

Figure 2.1: Centered drifter positions every 5 minutes are displayed over 10 m bathymetry contours at the mouth of the Columbia River. Drifter positions are colored by the relative direction of wind and waves, purple for opposing waves and currents, and orange for following waves and currents.

Offshore wave heights during the experiment were typically 1-2 m, tidal flows exceeded 3 ms^{-1} on strong ebbs, and wind speeds were typically 5-10 ms^{-1}. A summary of the deployments dates, tide stage, and general wind/wave conditions can be found in Table 2.1. Figure 2.2 shows histograms of the wave heights, peak frequencies, drift speeds, and depths measured over the course of this experiment. While opposing waves and currents generally occurred throughout ebb deployments, drifters would occasionally turn with obliquely incident waves such that there would be following relative wave/current directions when offshore. More ebbs were sampled than floods.

2.2.1 SWIFT drifters

SWIFT drifters are free-floating miniature spar buoys outfitted with a suite of instruments to make measurements near the ocean surface [*Thomson*, 2012]. In this study, six second-

Table 2.1: Overview of drifter deployments

date	tide stage	winds, [ms^{-1}]	wind direction [from]	offshore waves [m]
21-May-13	ebb	10	west-northwest	2.5-3.0
22-May-13	flood to ebb	5	west-southwest	2.5-3.5
25-May-13	ebb to flood	3-10	south	1.6
26-May-13	ebb to flood	3-12	south-southeast	1.2
27-May-13	slack to ebb	8-12	south	2-4
28-May-13	ebb, then ebb to flood	5-7	southwest	2
29-May-13	ebb	5-10	northwest	1.5-2.0
30-May-13	ebb	7	south	1.5
1-Jun-13	ebb, flood	5	south-southeast	1.0
2-Jun-13	ebb	10	north, northwest	1.5
3-Jun-13	flood to ebb	10	northwest	1.5
4-Jun-13	ebb	12-15	northwest	1.0-1.5
6-Jun-13	flood	3-7	northwest	1.0-1.5
7-Jun-13	flood	5-8	west/northwest	1.0 - 1.5
8-Jun-13	ebb	5-10	north	2-3
9-Jun-13	ebb	7.5	northwest	2.0
22-Jul-13	ebb and flood	5	north	1.0
23-Jul-13	flood and ebb	5-10	north	1.2
24-Jul-13	ebb to flood	5-8	north	1.2
25-Jul-13	ebb to flood	5-8	north	1.2
26-Jul-13	ebb	5-8	north	1.5
3-Sep-13	ebb	light	-	1.0
04-Sep-13	ebb to flood	5	southeast	0.8
08-Sep-13	flood	10	north	1
09-Sep-13	ebb to flood	5-8	north	1
10-Sep-13	flood	3	north	1
11-Sep-13	ebb to flood	8	south	1
12-Sep-13	ebb to flood	light	-	1.5
13-Sep-13	ebb	5	west-northwest	1

[a] Offshore waves heights taken from CDIP buoy 162. Winds were measured shipboard. Tidal stage is relative to Clatsop Spit.

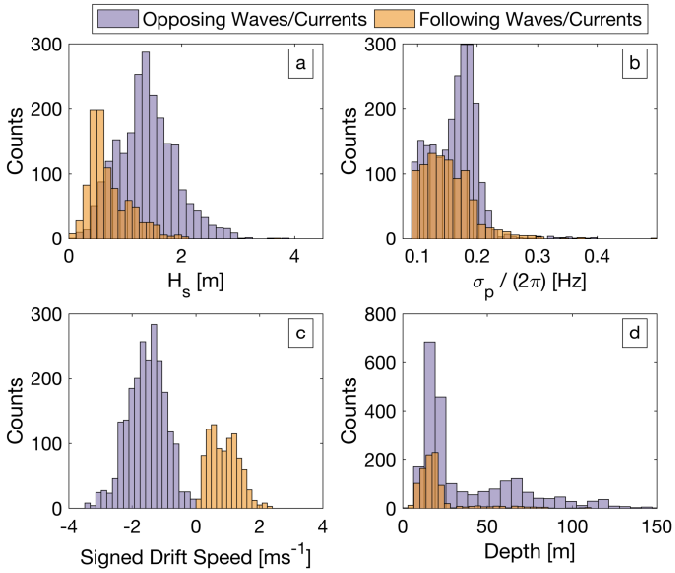

Figure 2.2: Histograms of significant wave height (a), peak wave frequency (b) drift speed (c) and depth (d) are shown above, colored by the relative wave/current direction.

generation SWIFTs were used, equipped to measure: wave orbital velocities, buoy drift speed, and location using a GPS logger (Qstarz BT-Q1000eX), vertical profiles of velocity using an Acoustic Doppler Current Profiler (1MHz Nortek Aquadopp), and breaking waves using a camera (GoPro Hero2).

Clocks from each independently recording instrument were synced before each deployment. However, clock drift made exact synchronous analysis difficult. Therefore, data were processed in 5-minute bursts, and averages over these bursts are used. While these short time averages result in noisy statistics, they are a compromise with the problem of statistical stationarity when drifting rapidly through a heterogeneous environment.

2.2.2 Currents

Drift speeds were measured using the onboard GPS logger at 5 Hz. Vertical profiles of the currents were measured with 1 MHz Doppler profilers, which were mounted internally in the spar buoy, looking down, such that the instrument head was approximately 1 m below the surface. The instrument recorded velocities in 1 m bins, up to a range of 25 m, with a 30 cm blanking distance, giving velocities at depths ranging from 1.35 m and 25.35 m below the surface. The Doppler data were recorded at 1 Hz, and averaged in 5 min intervals (300 samples per burst). Drift speeds were used to to correct the measured Doppler current profiles to absolute velocities (i.e., to convert from the drifting reference frame to the fixed reference frame). Because these measurements were made from a moving platform on the free surface, they inherently include a component of the Stokes drift [*Rascle and Ardhuin*, 2009]. This Lagrangian drift component is removed before subsequent analysis. However, the Stokes drift component is relatively small when compared with the large tidal velocities, generally less than 5% of the surface drift, and less than 3% of the measured ADCP velocity.

Only two of the six drifters recorded velocity profiles, because the other four drifters were equipped with up-looking Doppler to measure surface turbulence [e.g., *Thomson et al.*, 2014]. Vertical current profiles from the two drifters were extrapolated to the other four drifters using an empirical approach, where current profiles are bin-averaged by surface drift speed and direction. Appendix A expands on this process. The bin-averaged velocity profiles are shown in Figure 2.3. Generally, vertical shear was larger for opposing waves and currents (primarily ebbs, purple profiles) than following waves and currents (primarily floods, orange profiles). The exception being where drifters far offshore turned to follow the dominant wind and wave direction. These data primarily fit the dark orange bin in Figure 2.3, where vertical shear is larger when compared to the other following wave/current profiles.

2.2.3 Estimating Wavenumber, k

Estimation of wavenumber from a moving measurement platform in the presence of vertically sheared currents requires careful attention to reference frame. Here, we define three distinct reference frames, the absolute frame, ω, the wave intrinsic frame, σ_{intr}, and the measurement frame, σ_{meas}. The relation between the associated frequencies depends on the measurement platform velocity, U_{meas}, the effective velocity, $U_{eff}(k)$, and the wavenumber, which is independent of reference frame,

$$\omega = \sigma_{intr} + \vec{U}_{eff}(k) \cdot \vec{k} = \sigma_{meas} + \vec{U}_{meas} \cdot \vec{k}. \tag{2.11}$$

For regions of low shear or for small k, it is reasonable to assume that currents effects each wavenumber uniformly: $U_{meas} = U_{surface} = U_{eff}$ such that $\sigma^2_{meas} = gk\tanh(kd)$. However, in regions of large vertical shear (such as those measured during this experiment) there is significant variation from the effective current $U_{eff}(k)$ and the surface drift velocity, U_{meas}. Therefore, wavenumber must be estimated using,

$$\sigma_{meas} = \sqrt{gk\tanh(kd)} - [U_{meas} - U_{eff}(k)]\cos[\theta_r(k)]k, \tag{2.12}$$

where we have made the assumption that the measured velocity and the effective velocity are in the same direction. Here, $\theta_r(k)$ is the relative direction between the waves and the currents as a function of wavenumber.

Since estimates of U_{eff} are reliant on wavenumber (Equation 2.10), an iterative scheme was necessary. An initial estimate of wavenumber using the surface drift, $gk_{surf}\tanh(k_{surf}d) = \sigma^2_{meas}$ was used to estimate the first iteration of $U_{eff}(k)$ with Equation 2.10. The resulting $U_{eff}(k)$ was used in Equation 2.12, which was solved with MATLAB's *fminsearch* function, which employs a simplex method for finding minima in non-linear functions [*Lagarias et al.*, 1998]. This process was repeated until the percent difference in k when compared with the previous iteration became sufficiently small (mean percent difference less than 10^{-4}

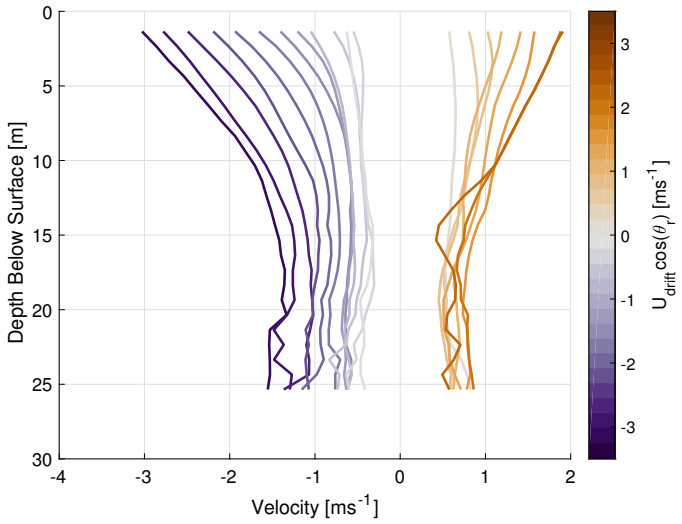

Figure 2.3: Profiles of velocity, bin averaged by drift speed relative to mean wave direction, are shown above. Shear was typically larger on ebbs, when waves opposed currents (purples) when compared with floods, where waves followed currents (oranges).

). Typically less than four iterations were required for each case (i.e., each 5-minute burst average).

Figure 2.4a shows the change in effective current relative to the surface current based on the mean shear profiles. For frequencies above 0.4 Hz, the effect is small. However the effect is large at low frequencies, with effective currents reaching less than 50% of the surface current. The largest relative change in effective current does not coincide with the largest currents, but rather with the largest shear. This is mostly found on ebbs, and thus the reduction from surface current to effective current is asymmetric with tide stage.

Figure 2.4b shows the percentage change in spectral wave slope squared, which is a parameter given by Ek^2 that will be related to the analysis of wave breaking observations (to follow). The squared slope is most affected in the wind sea range, near $f_{meas} = 0.2$ Hz, despite the smallest effective currents being at low frequencies (as seen in Figure 2.4a). This

is due to the the decreasing effect of the frequency shift at low frequencies, as $\vec{U}_{eff}(k) \cdot \vec{k}$ is small when k is small. Estimated slopes are more affected by shear on opposing waves and currents, when shear is larger, than on following waves and currents (floods) when vertical shear is less pronounced.

In linear theory, waves are blocked when the ambient current is equal and opposite to the intrinsic wave group speed, $C_g + U\cos(\theta_r) = 0$. Using the effective current increases the frequency at which this blocking occurs, as U_{eff} is reduced relative to $U_{surface}$. A histogram of estimated blocking frequencies is shown in Figure 2.4c. Blocking frequency is estimated as the lowest frequency for which $C_g(f) + U\cos(\theta_r(f)) = 0$, although we note this estimate is sensitive to the relative direction $\theta_r(f)$. The use of U_{eff} when compared with $U_{surface}$ results in fewer blocking frequencies estimated in the 0.25 to 0.4 Hz range, consistent with the effects discussed in Figure 2.4a-b. For either estimate, blocking frequencies are well above the peak frequencies (Figure 2.2b).

2.2.4 Measured Wave Energy Spectra

Wave energy spectra were estimated from the 5 Hz GPS data using the *Herbers et al.* [2012] method. GPS velocity data were processed in 5-min bursts using Welch's method, where FFTs of 128 s, de-trended Hanning-tapered windows were averaged with 75% overlap. Neighboring frequency bands were then merged, giving each spectrum approximately 42 degrees of freedom. Spectra of velocity, S_{uu} and S_{vv} were converted to surface elevation spectra using:

$$E(f) = \frac{(S_{uu} + S_{vv})c^2}{g^2}, \tag{2.13}$$

where c is the wave phase speed. Here $c = g\tanh(kd)/\sigma$ can only be determined after obtaining the the correct wavenumber at each frequency (via the iterative method in the preceding section).

Estimates of sea surface elevation from drifting platforms are sensitive to low-frequency

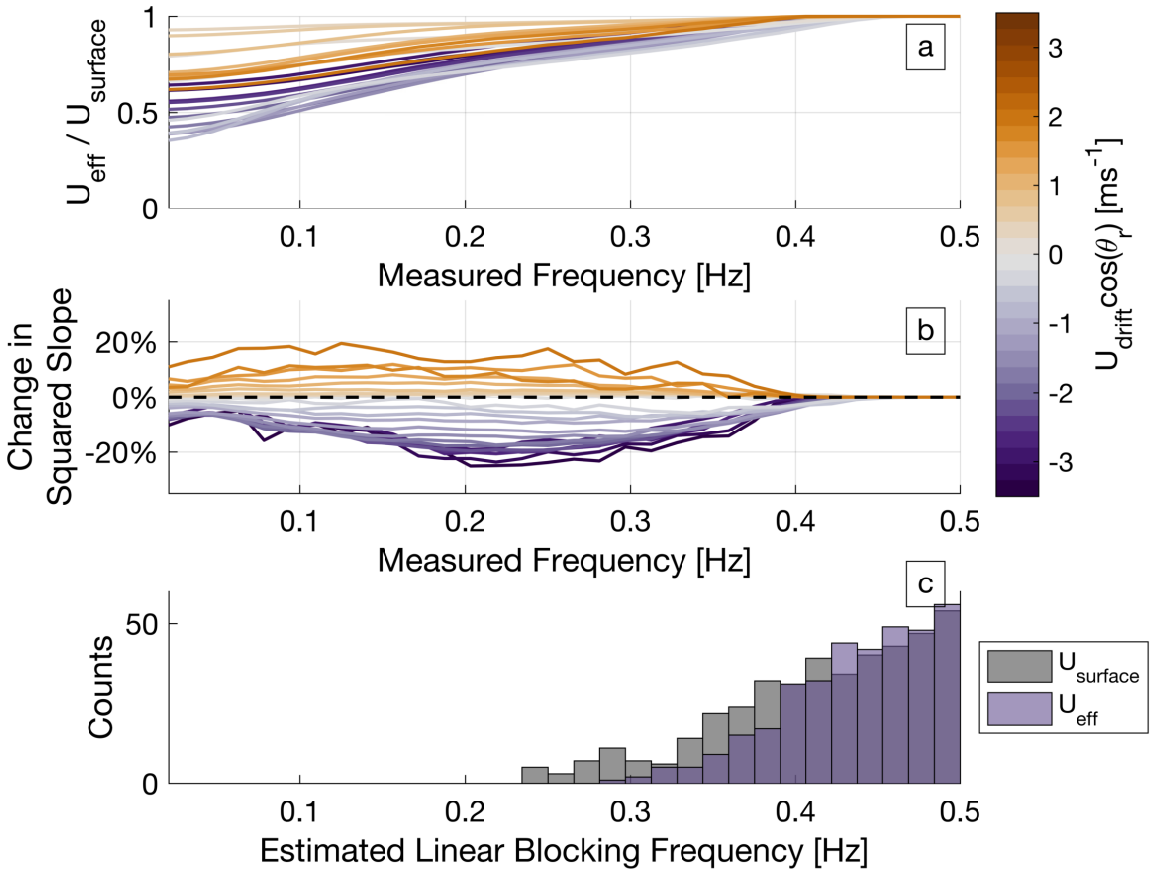

Figure 2.4: (a) The ratio of surface current to effective current based on the velocity profiles shown in Figure 2.3. (b) The percent difference in spectral squared slope, Ek^2, based on frequency and velocity profile. (c) A histogram of the estimated linear blocking frequency (the lowest frequency for which $C_g + U\cos(\theta_r) \approx 0$), using the surface current and the effective current.

noise, as the conversion heavily weights low frequencies through multiplication by $c^2 \propto \sigma^{-2}$. There are also non-linear interactions that affect the low-frequency regions of Lagrangian measured wave spectra *Herbers and Janssen* [2016]. Here, a small sub-set of spectra with maximum energy densities at the lowest measured frequency bins were removed from subsequent analysis. Buoy resonant motions contaminate frequencies near the natural frequency, approximately 1 Hz. Therefore frequencies above 0.8 Hz were not considered in analysis. Further, the buoy's tilting motions result in slight overestimation of horizontal velocities in the 0.2 to 0.5 Hz band. An empirical frequency dependent correction for this tilting motion was determined in a post-calibration of the buoy through the addition of an accelerometer.

Bulk wave parameters, significant wave height, H_s, mean wavenumber, k_m, and peak frequency f_p are estimated using the common forms: $H_s = 4\sqrt{\int E(f)df}$, $k_m = (\int E(f)kdf)/(\int E(f)df)$, and $f_p = (\int E(f)^4 f df)/(\int E(f)^4 df)$ [*Young*, 1999], with the integration range, $0.0625 < f < 0.8281$ Hz. Although the spectral correction for effective current is essential for the accuracy of the results that follow, these bulk parameters are used to simplify much of the presentation of the results.

2.2.5 Wave Breaking

GoPro cameras were mounted at the top of a 1 m mast on each buoy, looking down at the ocean surface, recording images at 1 Hz. The sampling scheme resulted in approximately 12,000 images recorded per SWIFT during a single 3-4 hour drift, and roughly 1.6 million images in total. Images were tagged as either breaking or non-breaking using the method of *Rusch et al.* [2014], where each image is given a score based on four distinct analysis techniques, and high scoring images are reviewed manually to confirm breaking waves.

Image score is increased if, (1) the number of relatively bright pixels in the image are above a threshold, (2) the median of the local (3x3 pixel) range-filtered image is above a threshold, or (3) if the entropy of the image is above a threshold. These three methods give the highest

score to bright, highly textured images. However, images with sun glare often have a similar brightness and texture to breaking waves, and would cause images without breaking waves to have a high score. The score of images with possible sun-glare contamination is reduced using an algorithm for the radial dependence of pixel brightness (which is strong for glare and weak for breaking waves). Because flagged images are manually reviewed, there are very few images scored as breaking waves where none exist (i.e., very few false positives, or type-1 errors). However, it is likely there are breaking waves that were not flagged by the analysis (i.e., false negatives, or type-2 error), and thus these estimates are likely an under prediction of the actual wave breaking.

Tilting motions from the buoy can result in large camera angles, which extend the camera footprint to the horizon and sky. Thus, images are first masked to limit the region of interest to the set of pixels near the buoy's deck. Further, a central image mask is used to exclude the pixels containing the buoy deck, mast, and flag, which can add image brightness and texture unrelated to breaking events.

The number of breaking waves in a 5-min burst, N_{brk}, is converted to breaking fraction, Q_b, using the peak wave frequency, f_p,

$$Q_b = \frac{N_{brk}}{\tau f_p}, \tag{2.14}$$

where $\tau = 300$ s, such that τf_p is an estimate for the number of dominant waves passing under the SWIFT during the 5 min burst. Note that this is the frequency in the drifting reference frame of the buoy ($f = \sigma_{meas}/2\pi$), because the parameter is the ratio of wave breaking to the observed waves.

Example images of breaking waves on ebb (purple) and flood (orange), as well as histograms of the total wave breaking counts, and breaking fraction are shown in Figure 2.5. The majority of the samples contain no breaking waves (the average breaking probability was small). Due to the short burst interval, N_{brk} has a larger effect on breaking fraction than the wave frequency. As a result, the conversion from the integer valued N_{brk} to Q_b gives a

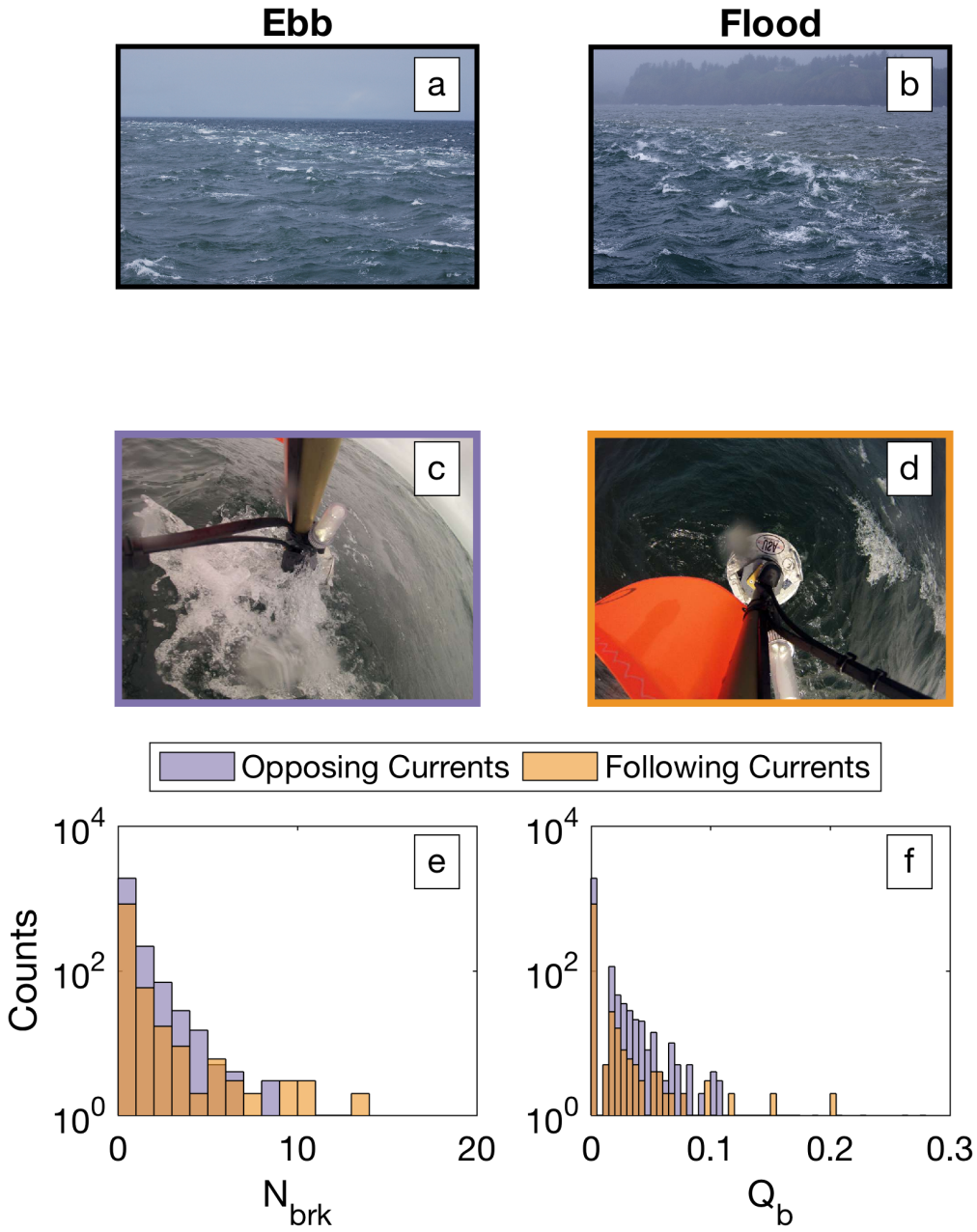

Figure 2.5: Examples of waves breaking on river fronts are shown for (a) an ebb example and (b) a flood example, photos courtesy of C. Bassett. Wave breaking as seen in the drifter mounted GoPro are shown in (c) and (d). Histograms of breaking rates (e) and breaking fraction (f) for all deployments, colored by opposing or following relative current direction.

banded distribution of breaking fraction (Figure 2.5e-f).

2.3 Results

2.3.1 Limiting Bulk Steepness

Wave measurements during the experiment show a wide range of heights, lengths, and steepness values. However, all of these measurements stay below a bulk steepness limit defined by the curve,

$$\frac{H_s k_m}{\tanh(k_m d)} < 0.4, \tag{2.15}$$

as seen in Figure 2.6. This limit applies across all aboservations, from large swells to small wind seas. Given to the large number of measurements taken over a range of scales and conditions, this curve represents a comprehensive steepness limitation with finite-depth and shear-current effects (which are included in estimation of k via Equations 2.10 and 2.12). Here, the maximum observed steepness $\gamma \approx 0.4$ is comparable to the range of limiting bulk steepness reported in previous studies, both in shallow water limit (e.g., *Raubenheimer et al.* [1996]; *Janssen and Battjes* [2007]) and deep (e.g., *Drazen et al.* [2008]; *Filipot et al.* [2010]) environments.

The importance of the applying the sheared current correction in estimating wavenumber (Equation 2.12) is apparent here, as the majority of tall waves, $H_s > 1$ m, are measured on opposing sheared currents, and thus are up to 20% less steep than would be assumed using the surface current alone. The effect is less strong on following waves and currents, where the correction is closer to 10%. However, failure to correct the wavenumber for shear (via the effective current parameter) would obscure the universal steepness limitation shown here; instead, a spurious result of two distinct limiting steepness values would be inferred.

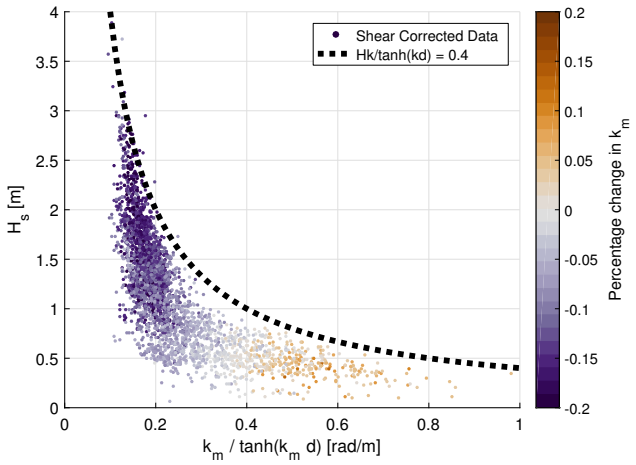

Figure 2.6: A scatter plot of significant wave height, H_s and depth adjusted mean wavenumber, $k_m/\tanh(k_m d)$ is shown above. Data points are colored by the percentage change in mean wavenumber from including currents relative to the surface value. Shear on opposing currents reduces the mean wavenumber (purples), and shear on following currents increases the mean wavenumber (oranges).

2.3.2 Breaking and the Relation to Bulk Steepness

The limiting steepness observed in the preceding section presumably occurs because of wave breaking. Indeed, Figure 2.7 shows that observed breaking fractions Q_b increase with bulk steepness. These measurements include data from buoys caught in convergence zones, which may represent a different type of breaking, but are still part of the average breaking that occurs in a river inlet. A more detailed discussion of fronts is provided in section 2.4.1. Three existing parametric models for wave breaking as a function of wave steepness, *Battjes and Janssen* [1978]; *Banner et al.* [2000]; *Chawla and Kirby* [2002] were fit to the data by minimizing the squared residuals. The model fits are shown as curves in Figure 2.7, and the model fit statistics are reported in Table 2.2. Here, we note that the *Banner et al.* [2000] model has been adjusted to use the full mean steepness, rather than the dominant steepness as originally intended, and thus a difference in the best fit constants is expected. Both the

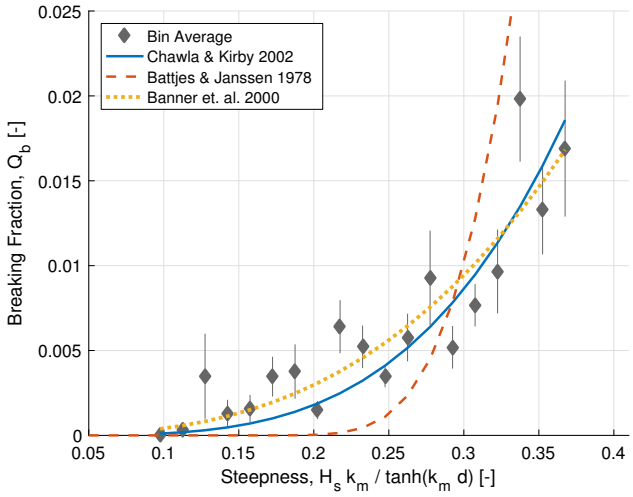

Figure 2.7: Breaking fractions, Q_b are bin averaged and plotted against steepness with standard error bars in gray above. Best fits, minimizing the sum of squared residuals to the *Chawla and Kirby* [2002] (solid blue), *Battjes and Janssen* [1978] (dashed orange), and *Banner et al.* [2000] (dotted yellow) models are overlaid on the measurement averages.

Chawla and Kirby [2002], and the *Banner et al.* [2000] models fit the data well. In contrast, the *Battjes and Janssen* [1978] model predicts a sharper increase in breaking with steepness than is seen in the data; it therefore under predicts breaking at low steepness values and over predicts at higher steepness values. While the *Banner et al.* [2000] model has the lowest sum of squared residuals, it has three free fitting parameters, and thus would be expected to provide a better fit. The *Chawla and Kirby* [2002] model has a similar error in using only one fit parameter, the limiting steepness γ. Further, the γ giving the best fit is similar to that used in the original study (0.84, compared to 0.96 in this study, once taking into account the difference between H_{rms} and H_s).

The video data has a small geographic footprint when upright, (approximately 2 m by 2 m) which potentially registers smaller wave breaking scales more easily than long breaking scales. A direct, per-scale comparison is difficult because the video data processing sim-

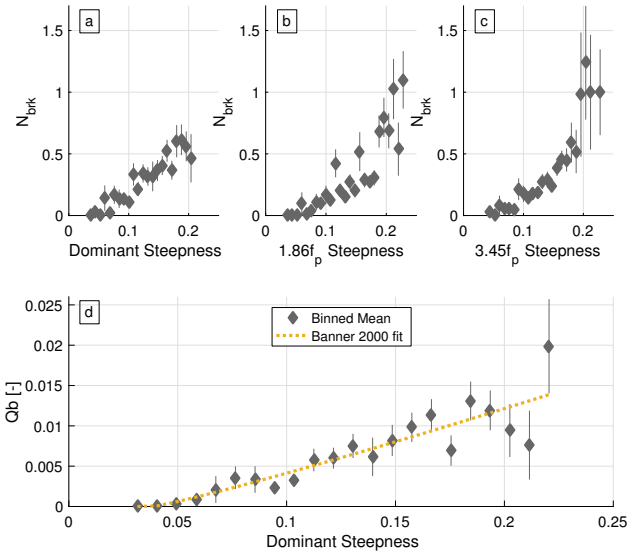

Figure 2.8: Wave breaking rate (number per 5 minutes) is bin averaged and plotted against steepness ($s = H_r k_r \tanh(k_r d)$) defined on scales relative to f_p (a), $1.86 f_p$ (b) and $3.45 f_p$ (c). The *Banner et al.* [2000] model for breaking fraction in the dominant wave breaking scale is compared with binned means in (d).

ply returns a binary flag for breaking on each image, and not an estimate of breaker size. However, we find the measured breaking rates increase with scale dependent steepness as defined by *Filipot et al.* [2010], (e.g., Equation 2.6). Figures 2.8a-c show breaking rates binned and plotted against steepness defined on different wave scales. When compared with the dominant steepness (Figure 2.8a), the trend appears linear, while a stronger increase of breaking rate with steepness is observed at the higher frequency bands (relative to the peak, Figure 2.8b-c). Dominant breaking fraction is also seen to increase nearly linearly with the dominant steepness (Figure 2.8d), and the best fit of the *Banner et al.* [2000] exponential model essentially results in a linear fit. Defining $Q_b = N_{brk}/(\tau f_c)$ introduces a slight auto-correlation with $1/f_c$ and the wave scale steepness. This auto-correlation is inverted in the previous example (e.g., Figure 2.7).

It is important to note that the breaking fractions measured in this study are lower than those reported in other studies, both in deep and shallow water. *Banner et al.* [2000] reports values as large as $Q_b = 0.08$ in deep water, while *Thornton and Guza* [1983] reports values as large as $Q_b = 0.6$ in shallow water. This is likely due to a combination of data processing and data collection methods. The semi-automated breaking detection algorithm employed in this study is designed to avoid false positives, but not false negatives, likely resulting in an underestimate of breaking counts. Further, the [*Young*, 1999] peak frequency is often slightly above the spectral energy maximum, which may overestimate the number of waves in each 5 min burst, thus decreasing estimates of Q_b. While these two artifacts may reconcile the difference between this study's measured breaking fractions, and reported deep water breaking fractions, it is unlikely to account for the difference with shallow water breaking fractions which are an order of magnitude larger. Of course, the waves in this study are not in shallow water, but rather range from intermediate to deep water conditions.

Despite infrequently measured breaking, there is still an apparent lower limit, below which no breaking is observed, $H_s k_m / \tanh(k_m d) = 0.1$, or $\beta_r = 0.05$. This value is similar to the $Hk/2 = 0.055$ observed in *Banner et al.* [2000] as a lower threshold on wave breaking steepness in deep water.

2.3.3 Filipot et al. [2010] Comparison with N_{brk}

In addition to the bulk parameter models, these observations can be applied as quasi-spectral estimates of wave breaking to provide an evaluation of the *Filipot et al.* [2010] model. Examples are shown in Figure 2.9 for opposing waves and currents (Figure 2.9a), and following waves and currents (Figure 2.9b). Breaking on following currents was primarily predicted for the shortest wave scale, $3.45 f_p$, while the shear correction mostly affects frequencies in the middle of the spectrum. Therefore, breaking rates on floods are not affected by the distinction between $U_{surface}$ and U_{eff}. Predicted breaking rates on ebbs, (opposing waves/currents),

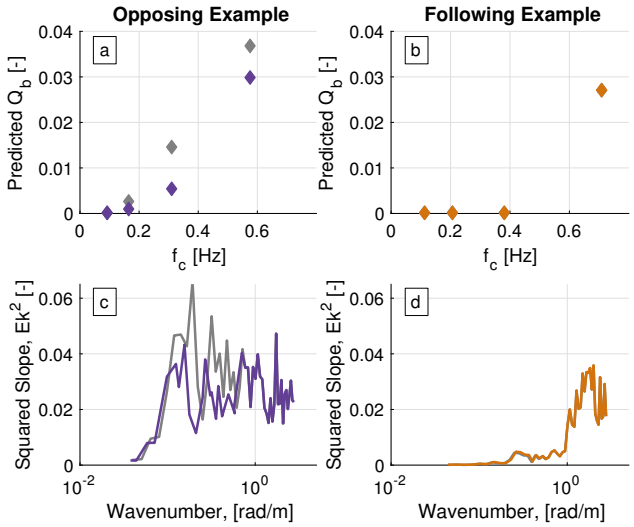

Figure 2.9: Example predictions of breaking fraction for each centered frequency bin for the *Filipot et al.* [2010] model for an ebb case (a) and a flood case (b). Grey points show the prediction without the sheared wavenumber correction. Spectral squared slope examples are shown in (c) and (d).

however, are greatly affected by this shear correction, as seen in Figure 2.9a. This is because there are notable changes to spectral steepness in 2.9c that are caused by the adjustment to U_{eff}. In this case, failure to correct for the sheared current results in over prediction of breaking fraction by about 50%. In part, this is due to breaking occurring in frequency bands more affected by the sheared currents, ($0.1 < f < 0.4$, Figure 2.4b), and that the predictions of Q_b grow quickly with steepness, such that the prediction is sensitive to small changes to the estimated wavenumber.

Extending this model to the entire data set, the total number breakers per wave spectrum predicted by the *Filipot et al.* [2010] model are compared with measured breaking data in Figure 2.10a. Since *Filipot et al.* [2010] subdivides a spectrum into four wave scales, the breaking fraction for each wave scale is multiplied by the estimated number of waves, $f_c\tau$, and summed together for an estimate of the total number of breakers per burst interval. This

Table 2.2: Best fit statistics for bulk wave breaking models

Model	Best fit parameters	Sum of Squared Residuals	Mean Percent Error
CK'02	$\gamma = 0.96$	1.1×10^{-4}	0.4
BJ'78	$\gamma = 0.65$	0.098	0.97
Ban'00 (mean)	$C_{1,2,3} = (0.29, 0, 2.8)$	9.7×10^{-5}	0.37
Ban'00 (dominant)	$C_{1,2,3} = (0.093, 0.039, 1.1)$	1×10^{-4}	0.27
Filipot'10	(not fit) $\tilde{\beta} = 0.48$	XX	XX

[a] Models were best fit to minimize the sum of squared residuals to the binned means. The *Filipot et al.* [2010] model was compared to N_{meas}, and not Q_b, and is therefore not compared above.

allows comparison between the model and the measured data, but in doing so effectively integrates over the spectrum, obscuring the model's predictions of scale. The model is well-correlated with the observations, however the model over-predicts breaking (i.e., mean of the residuals is $\langle N_{model} - N_{meas} \rangle = 1.6$). This is especially apparent in the $N_{brk} < 3$ range, which accounts for over 90% of the measured data. Most of the breaking predicted in the *Filipot et al.* [2010] model is in the shortest wave scale, $3.45 f_p$ (Figure 2.10d). No breaking is predicted at frequencies less than the spectral peak (i.e., the longest wave scale) and thus that histogram is excluded from Figure 2.10. Of course, this particular result is sensitive to the definition of spectral peak and the spectral shapes within this dataset; applying the *Filipot et al.* [2010] model to other datasets might predict breaking at these long scales.

There is a general separation of scales between cases of following and opposing currents. On following currents, the *Filipot et al.* [2010] model primarily predicts breaking in the shortest wave scale. On opposing currents, the model again predicts that the shortest wave scale also has the most breaking, but the longer scales have proportionately much more breaking activity.

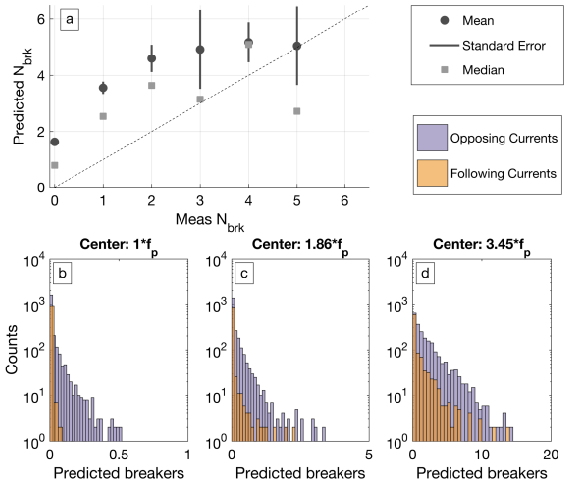

Figure 2.10: Bin averaged predictions of the total number of breaking waves using the *Filipot et al.* [2010] model are compared with breaking measurements (a). Histograms of the predicted breakers per frequency bin (i.e., wave scale) are shown in (b), (c), and (d), colored by opposing or following current direction.

2.4 Discussion

2.4.1 Strong Horizontal Current Gradients at Fronts

The images of flooding and ebbing fronts shown in Figure 2.5 highlight an important aspect of wave breaking that has not yet been discussed here. Fronts were commonly seen at the mouth of the Columbia River, and these were visually observed to be regions of intense breaking. They were also regions where the horizontal gradient in currents was large, both on ebbs when the (relatively) quiescent ocean water meets the outflowing river current, and on flooding fronts where the incoming tide is opposed by river currents. For both of these scenarios, the adverse gradient felt by the waves would require a rapid increase in wave steepness, often to an asymptote, as discussed in *Babanin et al.* [2011] and *van der Westhuysen* [2012]. Characterization of the spatial gradients from buoy point measurements (drifters) was not

possible, because the buoys remain trapped in the fronts and the horizontal gradients are not quantified. Further, only a select number of examples included visual confirmation from a shipboard observer. Still, the drifters in fronts generally measured much higher breaking rates than the mean wave steepness in the area. This may contribute to the high variability in mean breaking fraction in the steepness range, $0.15 < H_s k_m / \tanh(k_m d) < 0.25$, as bulk wave parameters likely do not capture other potential effects leading to breaking at fronts, such as single and double reflection [*Trulsen and Mei*, 1993; *Rousseaux et al.*, 2008, 2010], non-linear interactions [*Liu et al.*, 1990], and sideband growth [*Chawla and Kirby*, 2002; *Babanin et al.*, 2011].

2.4.2 Model Performance

The *Chawla and Kirby* [2002] model performs well, given only one free fitting parameter, γ. The model was modified from a shallow water form to include currents, which often shift breaking to intermediate depths. It is interesting to note that this model still performs well in this study, where approximately 80% of the data were in deep water (defined $d/L > 0.5$). This supports the use of a universal (unified, finite-depth) model for wave breaking, such as *Filipot et al.* [2010].

It is not surprising that the *Filipot et al.* [2010] over predicts wave breaking, given first that our measured breaking rates are likely underestimated due to type-2 error, and second, that we may be overestimating steepness on the ebbs (majority of data) due to the assumption of linear dispersion with a first order adjustment to the currents. In particular, [*Kirby and Chen*, 1989] made the assumption that $U/c << 1$, which is likely true for long waves in this study, but certainly not accurate in the short waves which often neared or reached blocking conditions on strong ebbs. Further, the majority of breaking predicted in the *Filipot et al.* [2010] model is in the higher frequency bands, where this effect would be strongest.

2.4.3 Directionality

A number of studies have suggested that increased directional spread, $\Delta\theta$ decreases breaking rates or probabilities [*Banner et al.*, 2002; *Gemmrich*, 2010; *Gemmrich et al.*, 2013; *Schwendeman and Thomson*, 2015b], or stated differently, that unidirectional waves are more likely to break. Further, [*Filipot et al.*, 2010] briefly discusses the importance of directional spread, but did not have directional data available for comparison. Figure 2.11a supports this hypothesis by showing a positive trend with averaged *Filipot et al.* [2010] model residuals ($N_{model} - N_{meas}$) and energy averaged directional spread, defined by

$$(\Delta\theta)_m = \frac{\int E(f)(\Delta\theta)df}{\int E(f)df}, \tag{2.16}$$

with spread estimated from the Kuik parameters $\Delta\theta(f) = \sqrt{\left(1 - \sqrt{a_2(f)^2 + b_2(f)^2}\right)\Big/2}$ [*Kuik et al.*, 1988; *Herbers et al.*, 2012]. At relatively low directional spreads ($\Delta\theta_m = 0.3$), the model does well in the mean, only slightly over predicting the breaking (mean residuals are 0.5), while as directional spread increases the model predicts much more breaking than was observed (mean residuals of ~ 2 at $\Delta\theta = 0.5$). This suggests that for the same steepness, waves with narrower directional spreading are more likely to break.

Residuals also appear to have a negative trend with the apparent current strength, $U\cos(\theta_r)$, as seen in Figure 2.11b. While it is possible that the two effects are related, as opposing currents cause refraction, which may lead to increased directional spread, there is no correlation or mean trend between $U\cos(\theta_r)$ and $\Delta\theta_m$. Two effects could then explain the correlation of $U\cos(\theta_r)$ and residuals. As suggested in lab study of *Yao and Wu* [2005], vertical shear $\partial U/\partial z$ could have a slight effect on wave breaking steepness, with waves breaking at steeper values for negative shear (as was seen on opposing currents, Figure 2.3). Therefore, less breaking would occur on large negative $U\cos(\theta_r)$, however more breaking would be predicted based on a constant breaking threshold $\tilde{\beta}$. The other possibility is that our measurements still over predict steepness values on ebbs, even after the shear

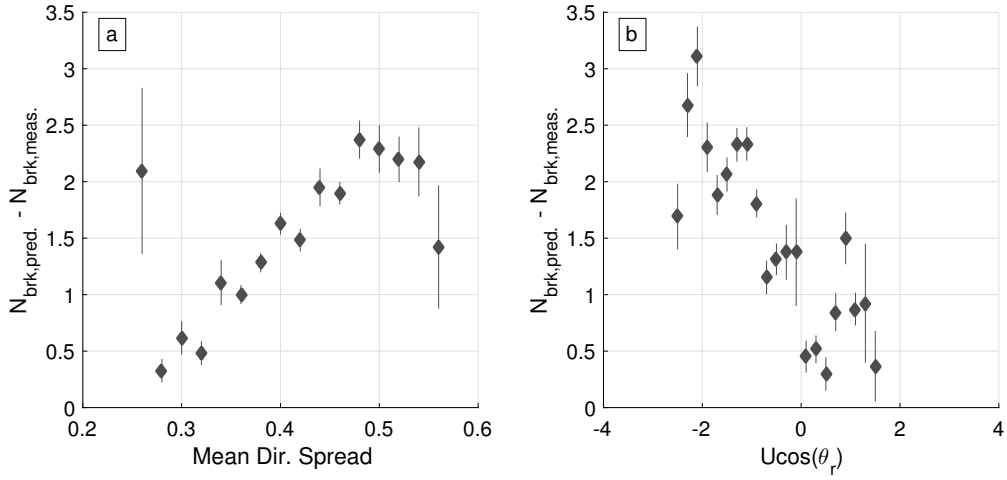

Figure 2.11: Wave breaking count residuals from the *Filipot et al.* [2010] model, $N_{model} - N_{meas}$, are bin averaged and plotted against mean directional spread (a), and the relative wave/current strength (b). Error bars show standard error.

correction, due to the assumption of linear, first-order shear dispersion, the assumed mean velocity profiles, or other factors. Without direct measurement of wavenumber, it is difficult to distinguish between the two effects.

2.4.4 Interpretation of the Limiting Steepness, γ

The range of steepness parameters that best fit the breaking data ($\gamma = 0.96, 0.65$, Figure 2.7, and Table, 2.2) is much larger than the maximum bulk steepness values observed in the data ($\gamma = 0.4$, Figure 2.6). This discrepancy can be attributed to an assumption inherent in the model, that as the local steepness approaches the value of the breaking parameter, the breaking fraction must approach 0.5 (i.e., every other wave is breaking). This is a logical assumption for the surf zone (where the Rayleigh distribution based breaking models were developed) where waves tend to reach breaking saturation as they approach the shoreline. However mean breaking fractions for the steepest observed waves in this study were approx-

imately 2%, clearly far from saturation. The result is a larger best fit breaking parameter than observed limiting steepness (e.g., Figure 2.6). This discrepancy in breaking fraction highlights some of the difficulties in a unified deep and shallow water wave breaking theory. Breaking in the two regimes have differing characteristics, which can be difficult to reconcile under the same limitations. For example, the relation of whitecap coverage to wind speed in deep water can be stronger than to wave statistics [*Schwendeman and Thomson*, 2015b], where in shallow water breaking is primarily controlled by bathymetry.

2.4.5 Implications for Spectral Wave Modeling

These results highlight the importance of including the vertical distribution of currents in spectral wave modeling. For example, using only surface currents in tidal inlets where vertical shear is expected could result in over estimates of steepness, and incorrect blocking frequencies resulting in overly large wave heights and incorrectly distributed wave dissipation. On flooding (following) currents, wave steepness may be understated, due to overestimations of the following current. While the changes in steepness are relatively small ($< 20\%$), they can result in large differences in breaking rates due to the shape of the breaking fraction functions.

This study focuses on breaking fractions, an underlying assumption in many dissipation models, rather than the dissipation itself. However, the poor agreement of the *Battjes and Janssen* [1978] model with the measured data casts doubt on dissipation models which include $Q_{b,BJ78}$, (e.g., *Ris and Holthuijsen* [1996] dissipation model for waves/currents). The success of *Chawla and Kirby* [2002] in fitting observed breaking data, and the relative success of the *Filipot et al.* [2010] breaking model give credence to modifications to the shallow water based dissipation models. Still, this study only quantifies and compares the wave breaking statistics, and not the underlying estimated wave dissipation. Further, the success of the *Filipot et al.* [2010] provides a basis for a universal wave breaking parameterization applicable

in deep and shallow water.

2.5 Conclusions

Measurements of waves and currents were collected at the Mouth of the Columbia River between May and September of 2013. Profiles of velocity in the top 25 m of the water column were used to refine the calculation of wavenumber, helping prevent the otherwise erroneously large estimates of wave steepness on opposing currents. We find the spectral correction to wave number is necessary in analysis of bulk steepness. The range of all bulk steepness values fall below $\gamma = 0.4$, consistent with other studies.

Wave breaking models based on a weighted Rayleigh distribution of breaking wave heights do well to explain the trends in measured wave breaking fractions. These models are based on a finite depth steepness, applicable to intermediate depth environments where wave breaking is often observed at river inlets. A quasi-spectral model also compares well with measured wave breaking. Measurements of directional spread indicate a relation to wave breaking as well, qualitatively consistent with previous deep water wave dissipation parameterizations.

In some ways, it is remarkable that linear methods for wave breaking work so well in these environments. The key to the success of these models in representing the field data is likely the statistical nature of the approach. In short, the probability of breaking is captured by the bulk parameters of the waves, with proper adjustment for sheared currents and finite-depths, but the details of the breaking process (and the inherent nonlinearity) are yet to be revealed.

2.6 Chapter Appendix

2.6.1 Velocity Binning and U_{eff} Sensitivity

Twenty bins of relative surface velocity, $U\cos(\theta_r)$, spaced at 0.29 ms^{-1} were used to create the mean velocity profiles in Figure 2.3. Of the 5293 5-minute bursts collected, 1198 5-minute

averaged velocity profiles were collected (22% of the data). The validity of using the bin-averaged velocity profiles in the top 25 m of the water column to estimate mean wavenumber was tested in the following ways.

2.6.2 Data Denial

A data denial study showed that using binned, mean profiles of velocity estimated similar mean wave numbers, k_m, to those estimated using the measured profiles. Mean profiles were calculated with 85% of the measured profiles (selected with a random number generator), and the remaining 15% were used for cross-validation. Here we will use $k_{m,meas.}$ for mean wavenumbers estimated using measured profiles, and $k_{m,mean}$ for mean wavenumbers estimated with the bin-averaged velocity profiles. Both the training data used to create the mean profiles, and the cross-validation set showed narrow Gaussian-shaped histograms of residuals, $k_{m,meas.} - k_{m,mean}$. The normalized residuals had means near zero, (-6.6×10^{-4} and 2.4×10^{-4} for training and cross-validation sets respectively) and small variance, (3.0×10^{-4} and 3.9×10^{-4} for training and cross-validation sets respectively).

2.6.3 Profile Depth Limitations

Many of the measured velocity profiles did not extend to the full water depth. However, extrapolations of measured velocity profiles to include velocities below 25 m water depth did not significantly affect estimates of mean wavenumber, k_m. Velocity profiles were fit with an exponential decay model to extrapolate velocities below 25 m. These extended profiles were then used to estimate mean wavenumber where the measured profile did not extend the full water column. All the extrapolated profiles were less than 0.1% different from the profiles using measured velocity profiles, ($|k_{m,extrap}/k_{m,meas.} - 1| < 10^{-3}$). This is likely because velocity shear is greatest near the surface, and because the surface velocities are weighted larger in the estimation of U_{eff}, (Equation 2.10).

Chapter 3

TURBULENCE FROM BREAKING SURFACE WAVES AT THE MOUTH OF THE COLUMBIA RIVER

3.1 Introduction

Turbulence at the ocean surface is important to the exchange of gasses, heat, momentum, and kinetic energy between the atmosphere and ocean. Turbulence introduced through wave breaking [e.g., *Craig and Banner*, 1994] and wave-turbulence interactions [e.g., *Thorpe*, 2004] elevate turbulence levels beyond the predictions for classic rigid boundary layers [*Agrawal et al.*, 1992]. Extensive work over the past three decades has improved understanding of the oceanic surface boundary layer through field measurements [*Agrawal et al.*, 1992; *Terray et al.*, 1996; *Drennan et al.*, 1996; *Gemmrich and Farmer*, 2004; *Jones and Monismith*, 2008; *Gerbi et al.*, 2009; *Sutherland and Melville*, 2015; *Thomson et al.*, 2016], development of models [*Craig and Banner*, 1994; *Burchard*, 2001; *Umlauf et al.*, 2003; *Umlauf and Burchard*, 2003; *Carniel et al.*, 2009], and laboratory measurements [*Duncan*, 1981; *Rapp and Melville*, 1990; *Lamarre and Melville*, 1991; *Drazen and Melville*, 2009]. This prior work has focused on wave conditions in deep and intermediate water depth. A more limited literature has focused on measurements and models in the surf zone [*Feddersen and Trowbridge*, 2005; *Feddersen et al.*, 2007; *Feddersen*, 2012a, b; *Grasso et al.*, 2012] and at river inlets [*Thomson et al.*, 2014; *Zippel and Thomson*, 2015; *Moghimi et al.*, 2016], where modifications to the wave field from currents and bathymetry alter surface boundary layer processes.

Very near the surface (within a few wave heights), turbulent kinetic energy (TKE) dissipation rates are balanced to a first order by turbulent transport [*Scully et al.*, 2016], which can be modeled as a diffusive process [*Craig and Banner*, 1994; *Burchard*, 2001; *Umlauf and*

Burchard, 2003]. Wave breaking provides a source of turbulence, which is modeled as a TKE flux input at the surface. In deep water, the equilibrium of short wind-waves [*Phillips*, 1985; *Thomson et al.*, 2013] is often assumed, and the surface flux into the ocean is estimated from wind parameters [*Gemmrich et al.*, 1994; *Terray et al.*, 1996; *Sutherland and Melville*, 2015; *Thomson et al.*, 2016]. In the surf zone, the breaking of long waves injects additional TKE to the surface, on the order of 10-15% of the total wave energy flux gradient [*Feddersen*, 2012b; *Zippel and Thomson*, 2015]. The surface flux of turbulence is difficult to prescribe at river inlets where wave breaking is different from purely wind-driven white capping or depth-limited surf. Here, waves break on strong currents and in intermediate depth [*Zippel and Thomson*, 2017]. Indeed, even wave dissipation (distinct from the turbulent dissipation) in such environments is still an active area of research [e.g., *Rapizo et al.*, 2017].

In addition to the magnitude of the TKE surface flux, the vertical fate of this turbulence remains an active research area. Many studies agree that the decay scale is set by the wave height and that the vertical decay is a power law. However, measurements have yet to converge on a single decay exponent, λ, for TKE dissipation rate. Estimates are typically constrained to $1 < \lambda < 2$, but this appears to be sensitive to the choice of reference frame. Many studies using fixed frame instruments, such as *Terray et al.* [1996]; *Drennan et al.* [1996]; *Jones and Monismith* [2008]; *Gerbi et al.* [2009] found decay scales of, $\lambda = 2$. Studies measuring inside wave crests with wave-following platforms found different values, for example *Gemmrich* [2010] found $1 < \lambda < 1.5$, *Sutherland and Melville* [2015] found $\lambda = 1$ for $z < 0.6H_s$, and *Thomson et al.* [2016] found $\lambda = 1.4$.

There is a lack of consensus, then, on the appropriate surface flux of TKE and its vertical decay at river inlets. This has, in part, lead to difficulty in understanding how wave breaking turbulence influences such regions. Even so, there is a growing body of work on how wave-breaking turbulence might interact with buoyant layers. For example, *Gerbi et al.* [2013] modeled a buoyant river plume during upwelling favorable winds and found that the inclusion

of wave-breaking turbulence increased plume thickness. Using field measurements, *Thomson et al.* [2014] showed large wave energy flux gradients across a plume front and observed wave-breaking turbulence levels at the surface that were as large as published turbulence values at the subsurface plume interface. Further studies have investigated surface boundary layer effects where buoyancy is relevant [*Vagle et al.*, 2012; *Gerbi et al.*, 2015].

3.1.1 Turbulence Scalings

Craig and Banner [1994] presented one of the first analytic results for wave breaking turbulence. Assuming turbulent transport can be modeled diffusively, they presented a solution where vertical diffusive transport balances TKE dissipation near the ocean surface,

$$\frac{d}{dz}\left(\nu_k \frac{dq^2}{dz}\right) = \epsilon, \tag{3.1}$$

where ν_k is diffusivity of TKE, q^2 is TKE, and ϵ is the TKE dissipation rate. In *Craig and Banner* [1994], diffusivity is a function of turbulent length scale, ℓ, a constant, S_q, and the turbulent velocity scale such that $\nu_k = S_q \ell q$. We note that it has become more common since *Craig and Banner* [1994] to express the diffusivity of TKE as a function of the eddy diffusivity and σ_k, the turbulent Schmitt number, such that $\nu_k = \nu_t/\sigma_k = (C_\mu/\sigma_k)q\ell$ [*Umlauf and Burchard*, 2003], where C_μ is a shear dependent stability function [*Canuto et al.*, 2001]. *Craig and Banner* [1994] also assumed a linearly increasing turbulent length scale, ℓ, with distance from the surface, z (defined positive down)

$$\ell = L(z + z_0), \tag{3.2}$$

where z_0 is a roughness length, and L was assumed to equal Von Kàrmàn's constant, κ, such that $L = \kappa = 0.41$. *Umlauf and Burchard* [2003] suggested length scales in free-shear flows may not evolve identically to wall-bounded shear flows, and thus suggested $L < \kappa$. The common closure assumption between TKE, ℓ, and the TKE dissipation rate, ϵ, was also

made,

$$\ell = (C_\mu^o)^3 \frac{q^3}{\epsilon}. \tag{3.3}$$

Where $C_\mu^o = 0.55$ is a model constant. Lastly, using a surface boundary condition relating the flux of TKE through the surface, G, to wave energy dissipation, Eq. (3.1) was shown to yield power law decay functions for TKE dissipation and TKE respectively,

$$\frac{\epsilon z_0}{G} = 2.4 \left(1 + \frac{z}{z_0}\right)^{-\lambda}, \tag{3.4}$$

$$\frac{q^2}{G^{2/3}} = 2.51 \left(1 + \frac{z}{z_0}\right)^{-(2\lambda/3-1)}. \tag{3.5}$$

Umlauf and Burchard [2003] showed the power law decay λ could be expressed in terms of model parameters,

$$\lambda = \frac{3(C_\mu^o)}{2L} \left(\frac{2}{3} R \sigma_k\right)^{1/2} + 1, \tag{3.6}$$

where $R = C_\mu^o / C_\mu$. In the absence of mean shear (as is expected in the surface boundary layer with wave breaking) the stability function C_μ is assumed to equal the model constant, C_μ^o such that $R = 1$ [*Canuto et al.*, 2001; *Umlauf and Burchard*, 2003]. The constants used in *Craig and Banner* [1994] result in $\lambda = 3.4$, which would require $\sigma_k \approx 2$ under this framework [*Feddersen and Trowbridge*, 2005, section 2.c offers a useful discussion on σ_k.]. *Burchard* [2001] therefore suggested the turbulent Schmitt number be a function of the ratio of production and dissipation, $\sigma_k = \sigma_k(P/\epsilon)$.

Terray et al. [1996] proposed that the surface roughness length is proportional to the significant wave height, $z_0 \propto H_s$, and used field measurements from small waves on a lake to fit the scaling,

$$\frac{\epsilon H_s}{G} = 0.3 \left(\frac{z}{H_s}\right)^{-\lambda}. \tag{3.7}$$

A power law decay with $\lambda = 2$ was proposed to hold below a breaking layer with depth, $z_{brk} = 0.6 H_s$, above which dissipation rate was assumed to be constant. This constant breaking layer concept has been refuted with recent measurements from surface following

platforms, where the decay slope $1 \leq \lambda \leq 2$ is found very near the free surface [*Gemmrich*, 2010; *Sutherland and Melville*, 2015; *Thomson et al.*, 2016]. These recent measurements are in moving frame coordinates, $\tilde{z} = z - \eta$, where η is the ocean free surface.

Currently, there is no clear consensus on how to map measurements from the $\tilde{z}$ coordinate frame to coordinates referenced to the mean sea surface, that is to say, mapping from $\tilde{z}$ to $z = \langle \tilde{z} \rangle$. Both *Gemmrich* [2010] and *Thomson et al.* [2016] did it directly, using raw time series of η. Without a general coordinate transform, it is difficult to fully interpret comparisons of the various field measurements and model predictions. It is also important to note the change from $(z/z_0 + 1)$ in the analytic solution to (z/H_s) in the scaling, which can give similar functional values near the surface for different values of λ and z_0/H_s.

Choosing a constant turbulence length scale, $\ell(z) = \ell_c$ results in an exponential decay, rather than a power law decay, as discussed in [*Umlauf et al.*, 2003] for deep water, and independently in [*Feddersen*, 2012b] for shallow water. This solution is particularly interesting as it may apply in the region $z \leq z_0$, where the assumption of a linearly increasing length scale near the surface may not hold. Following *Feddersen* [2012b], the TKE dissipation rate could then be expressed as,

$$\frac{\epsilon z_0}{G} = A \exp(\alpha z / z_0), \tag{3.8}$$

with $\alpha = (3/2)^{1/2} C_\mu z_0 \ell_c^{-1}$ and $A = \alpha / \exp(\alpha)$ such that specification of $\ell_c / z_0 = L$ sets the decay scale.

Here, we present field measurements of turbulence and waves from the mouth of the Columbia River to examine the validity of these surface turbulence models under a wide range of wave conditions. In particular, we focus on determining an appropriate model roughness length and length scale decay constant. A description of the field site, the data set, and wave and turbulence processing techniques are presented in section 2. Data processing includes a method for correcting buoy velocities for platform motion, and compares two methods for estimating TKE dissipation rates. Field measurements are compared with

existing turbulence models in section 3, along with a limited exploration of the interaction of surface turbulence with the sub-surface stratification. Section 4 discusses the choice of model constants, and the implications of the measurement reference frame on the results. The results are summarized in section 5.

3.2 Methods

Measurements of waves and turbulence were collected from freely drifting SWIFT buoys [*Thomson*, 2012] at the Mouth of the Columbia River as part of the RIVET-II experiment between April and September of 2013. Up to six buoys were deployed at a time on drifts lasting a few hours each. On ebbs, the research vessel would often wait for the tide to change in order to safely cross the Columbia River Bar, such that buoys were not tended during the drifts. On floods, the research vessel could operate throughout the domain, and buoys were tended during the drifts (including reset if they approached shore, thus avoiding grounding). Therefore, ebb deployments lasted longer, and more data were collected on ebb tides. Buoys were deployed in pairs, and they typically stayed within a few hundred meters of each other throughout a drift. Figure 3.1 shows drifter tracks over 10 m bathymetry contours (bathymetry prepared by *Akan et al.* [2017]). Measured wave heights ranged from 1 m to 4 m, winds were typically 5-10 m s^{-1}, and drift speeds were up to 3.5 m s^{-1} on strong ebbs.

3.2.1 Surface Waves and Wave Breaking

Wave statistics were estimated with velocity data collected at 5 Hz with Qstarz BT-Q1000eX GPS loggers. Following the *Herbers et al.* [2012] method, horizontal velocities were converted to sea surface elevation statistics using linear theory,

$$E(f) = \frac{(S_{uu} + S_{vv})c^2}{g^2}, \tag{3.9}$$

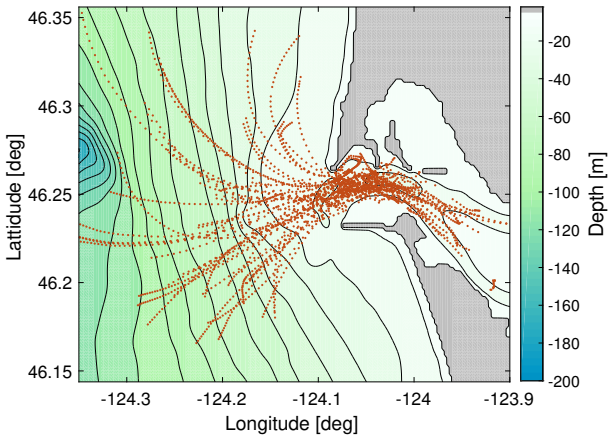

Figure 3.1: Drifter 5-min averages in location (orange) are shown over 10 m bathymetry contours at the mouth of the Columbia River.

where $E(f)$ is the wave spectrum, S_{uu} and S_{vv} are the spectra of horizontal velocity components, c is the wave celerity determined from dispersion, and g is the gravitational constant. Significant wave heights were estimated as $H_s = 4\sqrt{\int E(f)df}$. The wave celerity c and wavenumber k are altered via wave current interaction and vertically sheared currents, and therefore the *Kirby and Chen* [1989] dispersion relation was used to estimate wavenumber via an iterative scheme. Wave breaking is observed onboard each buoy using a GoPro Hero 2 camera. A full description of the wave breaking and wave spectral processing is available in *Zippel and Thomson* [2017].

3.2.2 Raw turbulence data and motion correction

Velocities were measured using 2 MHz Nortek Aquadopp profilers. The Aquadopps were mounted inside the buoy spar, with the length of the Aquadopp body vertical. The Aquadopp heads were mounted in line with the body, such that the 3 acoustic beams were looking 20 degrees off axis with vertical. Samples were recorded at 4 Hz in pulse coherent (HR) burst mode, with a 5-min sampling interval (1024 samples per burst), in 16 profile bins spaced 4

cm apart with a 10 cm blanking distance. The profiler heads were mounted at 0.67 m depth such that the farthest bin from the Aquadopps were approximately at the ocean surface. Because the buoys were free drifting, the velocities measured in this reference frame were primarily turbulent fluctuations. The velocity range of the pulse coherent instruments was 1.15 m s^{-1} in the horizontal and 0.48 m s^{-1} in the vertical, allowing accurate measurement of turbulence in strong currents (drift speeds were measured over 3 m s^{-1}, but drifter slip relative to these currents was less than 10 cm s^{-1}). More details on the Aquadopp settings and sensitivity are in *Thomson* [2012].

The drifting platform primarily tracks with the free surface, such that velocity contamination by wave orbital motions is small. However, measured along beam velocities, $\mathbf{u}_{beam}(z,t)$, are contaminated by buoy motions, both translational (bobbing) and rotational (tilting) motions. We remove these motions from the time-domain measured velocity as follows.

Pressure measurements onboard the Aquadopp are converted to water depth using $z = P/\rho g$, where ρ is the water density and P is the measured pressure. The vertical velocity relative to the free surface is then estimated using a centered difference of the measured water depth. The component of this velocity projected into along-beam coordinates is, $u_{bob,beam} = (\mathbf{T}\hat{\mathbf{x}}) \cdot \mathbf{u}_{bob}$, where $\mathbf{T}$ is the rotation matrix based on the measured heading, pitch, and roll, and $\hat{\mathbf{x}}$ is the position unit vector of the Aquadopp measurement bin relative to the the beam transducer. Because the roll is measured in the yawed, pitched reference, and pitch is measured in the yawed reference, the transformation matrix is, $\mathbf{T} = \mathbf{H}(\mathbf{PR})$, with

$$\mathbf{H} = \begin{bmatrix} \cos(h) & \sin(h) & 0 \\ -\sin(h) & \cos(h) & 0 \\ 0 & 0 & 1 \end{bmatrix}, \mathbf{P} = \begin{bmatrix} \cos(p) & 0 & -\sin(p) \\ 0 & 1 & 0 \\ \sin(p) & 0 & \cos(p) \end{bmatrix}, \mathbf{R} = \begin{bmatrix} 1 & 0 & 0 \\ 0 & \cos(r) & -\sin(r) \\ 0 & \sin(r) & \cos(r) \end{bmatrix},$$

where h is the heading, p is the pitch, and r is the roll.

The Aquadopps were mounted away from the center of motion of the buoy, looking off axis resulting in a non-orthogonal beam vector relative the rotational motions. Following

Edson et al. [1998], the fixed-frame angular rate psuedovector, $\mathbf{\Omega}$, was estimated,

$$\mathbf{\Omega} = \begin{bmatrix} 0 \\ 0 \\ \dot{h} \end{bmatrix} + \mathbf{H} \begin{bmatrix} 0 \\ \dot{p} \\ 0 \end{bmatrix} + \mathbf{HP} \begin{bmatrix} \dot{r} \\ 0 \\ 0 \end{bmatrix},$$

where $\dot{()}$ represents a centered difference estimate of the derivative. The expected rotational velocity measured along a beam is then $u_{rot,beam} = \hat{\mathbf{x}} \cdot \{\mathbf{\Omega} \times [\mathbf{T}(\mathbf{x} - \mathbf{m})]\}$, where $\mathbf{m}$ is the center of motion of the buoy. There is a small amount of overlap, as the bobbing correction implicitly contains a component of the vertical rotational motion. We estimate the rotational effects to be relatively small when compared with the bobbing correction. Still, this may overcorrect motions in some cases and result in a bias in TKE.

Raw measured along-beam velocities were corrected in the time domain $u(t)_{cor,beam} = u(t)_{meas,beam} - u(t)_{bob,beam} - u(t)_{rot,beam}$. Due to the centered difference estimates for $\dot{h}$, $\dot{p}$, $\dot{r}$, and $\dot{z}$, the number of corrected samples in each burst became 1022, rather than the measured 1024. Before further processing, velocity data were quality controlled using the reported backscatter amplitude ($a > 30$ counts) and correlations ($cr > 50$) [*Elgar et al.*, 2001; *Thomson*, 2012]. Removed points were replaced with cubic interpolation (because a continuous series is needed for spectral analysis), however if more than half of the 4-Hz samples were removed, the 5-min bin sample would not be used. Velocity spectra were estimated using Welch's method, where each 1022 sample motion-corrected time series was split into windows of 64 samples each with 50% overlap, and a Hamming taper was applied to each window. The FFTs of each window were then averaged, resulting in a power spectral density estimate with approximately 16 degrees of freedom.

Example velocity spectra are shown in Fig. 3.2. Typically, the vertical velocities due to bobbing (and estimated from the pressure measurement) accounted for most of the platform motion contamination, and the effects of rotational motion were relatively small. The translational bobbing motions were most apparent near 1 Hz, the estimated natural frequency

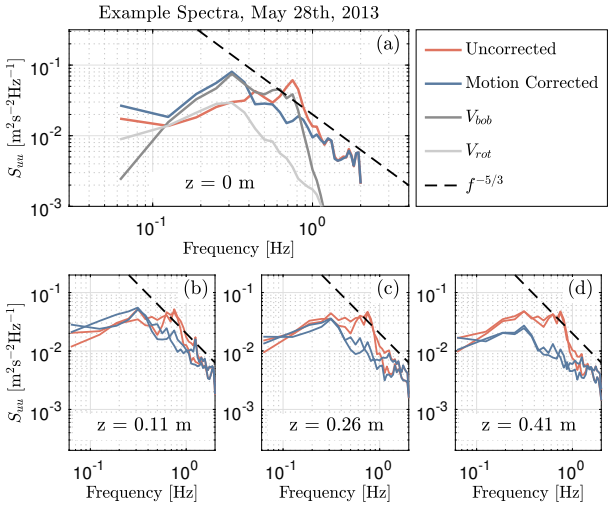

Figure 3.2: Example 5-min along-beam velocity spectra from May 28th, 2013, are shown above. The spectrum of measured velocity (orange) is shown along with the spectra of estimated motion induced bobbing (dark grey) and rotational velocity (light grey), and the motion corrected spectrum (blue) for the forward-facing beam's near surface bin in (a). The raw, and motion corrected spectra from all three Aquadopp beams at depths 0.11 m, 0.25 m, and 0.41 m are shown in b-d along with a $f^{-5/3}$ slope for reference.

of the buoy [*Thomson*, 2012]. A second peak associated with the tilting motions was also apparent at a slightly lower frequency. The bobbing motions contaminate the frequencies where the equilibrium range is typically observed. Once corrected for platform motions, however, a region with $f^{-5/3}$ slope is evident in most spectra, consistent with an inertial subrange. Two of the Aquadopp beams faced away from the vane, and were thus oriented away from any flow disturbance caused by platform (i.e., away from self-wake). The third beam, however, often experienced flow distortion and was therefore not used.

3.2.3 TKE dissipation rates and TKE

Two methods were used to estimate TKE dissipation rates, the structure function method [*Wiles et al.*, 2006], and a spectral method based on *Tennekes* [1975]. We will briefly overview

the former here, and note the more complete description can be found in *Thomson* [2012]. The second-order structure function is defined,

$$D(z,b) = \langle [u(z) - u(z+b)]^2 \rangle, \tag{3.10}$$

where b is the spatial distance between measurements, $\langle\rangle$ denotes a time average, and $u(z)$ is the demeaned along-beam velocity. The structure function can be related to the dissipation rate ϵ through,

$$D(z,b) = C_\nu^2 \epsilon(z)^{2/3} b^{2/3} + N, \tag{3.11}$$

where N is an offset introduced through uniform noise across all measurements, and $C_\nu^2 = 2.2$ is a constant [*Wiles et al.*, 2006].

The spatial structure function has been the preferred TKE dissipation estimate in previous studies using SWIFT drifters because it is robust to platform motion. In this present study, motion correction is done directly, and thus the dissipation rate can also be estimated using the $f^{-5/3}$ slope region of the spectrum. In the spectral method, velocity measurements in frequency are converted to turbulent wavenumber with an advective scale, $k_t = 2\pi f / U_{adv}$, and the assumption of a frozen turbulence field. This presents a problem in the free drifting measurement frame as the relative velocity of the ambient water relative to the platform is near zero, $U_{adv} \approx 0$. Here, we follow from *Tennekes* [1975], where velocity spectra in the absence of an ambient current are expected to follow a self-advected form,

$$\Phi(\omega) = \chi \epsilon^{2/3} u_{rms}^{2/3} \omega^{-5/3}, \tag{3.12}$$

where u_{rms} is the root mean square of the demeaned velocity, and $\chi = 8$ is a constant [*De Silva and Fernando*, 1994] and $\omega = 2\pi f$. Equation (3.12) is inverted to solve for ϵ.

Example profiles of TKE dissipation rates are shown in Fig. 3.3. Spectrally estimated dissipation rates use the mean slope in the inertial subrange, set to $0.68 < f < 1.5$ Hz. The methods agree favorably in magnitude across all three acoustic beams. The spectral

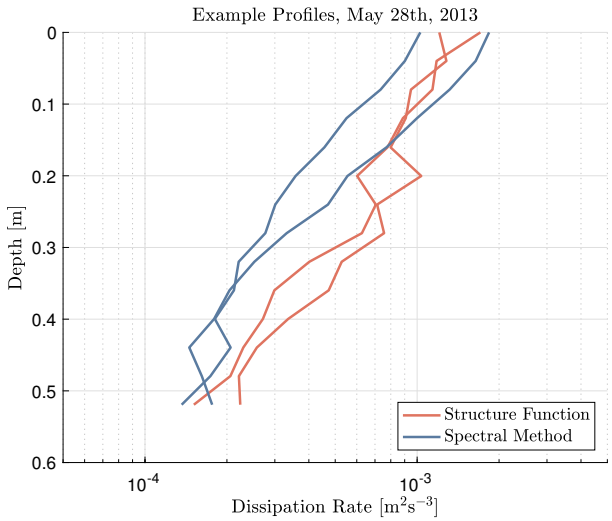

Figure 3.3: Example profiles of TKE dissipation rate estimated using the structure function method (orange) and the spectral method (blue) are shown. The data used here to estimate TKE dissipation rates are the same as were used in Fig. 3.2.

method shows more variation vertically. This may be due to increased spatial independence in estimating dissipation. That is to say, the structure function method uses distributed spatial information in estimating TKE dissipation rates, which may blur existing spatial gradients. The spectral method is more localized in space, with strict separation between estimates in depth, which may be the cause of increase vertical slope in Fig. 3.3. This is consistent with the work of *Guerra and Thomson* [2017], where structure function estimates also showed less spatial variation than the spectrally estimated dissipation rates, (i.e., *Guerra and Thomson* [2017] Figs. 6, and 12).

A comparison of the spectral method and the structure function method across all measurements and depth bins is shown in Fig. 3.4. The structure function method reaches a noise floor of $\epsilon \sim 10^{-5}$, where spectral dissipation estimates ranged to 10^{-7}, implying a smaller noise floor. At larger dissipation rates, most of the estimates agree.

TKE is estimated using the variance of the motion-corrected velocities along each beam.

The variances from beam 2 and 3 (beam 1 is in the wake of the platform and thus avoided) are averaged, such that $q^2 = (3/2)(\sigma_{u,2}^2 + \sigma_{u,3}^2)/2$, assuming isotropy. In the case of non-isotropic turbulence, horizontal eddies larger than the drifting platform are not expected to be measured, as they would result in platform motion, not velocity fluctuations relative to the free drifting platform. It is not clear if these eddies will retain importance when the measured turbulence analysis is in the free drifting reference frame.

The velocity measurements in this study are referenced to the free water surface ($\tilde{z}$-coordinates) rather than the mean sea surface (z-coordinates). While the balance of diffusion and dissipation has, to this point, been referenced to the z-coordinate reference, we will nonetheless test these equations from the surface following reference. We note that the same set of equations can be derived from a diffusive-dissipative balance in substituting $\tilde{z}$ for z, if no extra terms arise in the TKE balance from the coordinate transform. In fact, the surface boundary condition of TKE flux is more physically justified at the free surface than the mean surface. The numeric implications of this reference frame mapping are discussed in section 4a.

3.3 Results

3.3.1 Wave steepness

The results suggest that surface wave breaking is the dominant source of near-surface turbulence throughout the Columbia River Mouth. Figure 3.5 shows a strong correlation of depth-averaged TKE and TKE dissipation rates with the finite-depth wave steepness. *Zippel and Thomson* [2017] showed this steepness is a strong indicator of wave breaking at river inlets, which is distinct from both wind-driven breaking in deep water and bathymetry-driven breaking in the nearshore. The commonly used deep and shallow indicators for wave breaking (U_{10} and H_s/d, respectively) are not correlated with the turbulence estimates from this study (not shown). The strong correlation of turbulence values with wave steepness holds

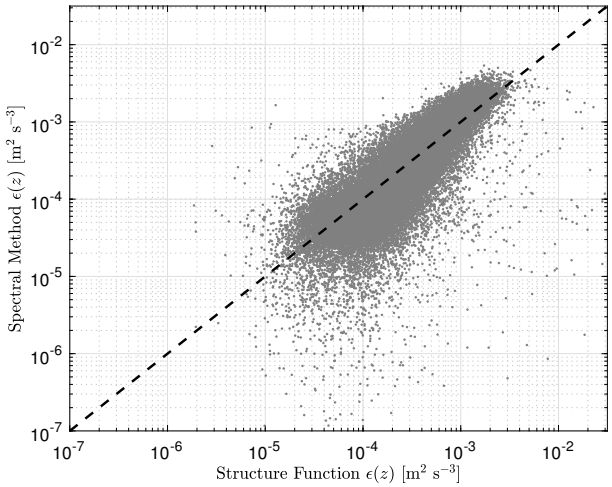

Figure 3.4: A comparison of TKE dissipation rate estimates from all depth bins, at all sampling locations from the structure function method and the spectral method are shown, along with a 1:1 line (dashed black).

for estimates from both the spectral method and the structure function method.

3.3.2 Turbulent Length Scales

Roughness length estimates $\ell(\tilde{z} = 0)$ are found by combining Eqs. (3.2) and (3.3), such that

$$q^3/\epsilon = [L/(C_\mu^0)^3]z_0.$$

Figure 3.6 shows estimates from the measurement bin closest to the free surface (within 0.04 m of the instantaneous surface). The roughness lengths are related to both significant wave height and mean wavenumber. The correlation with wave height is strong, while the correlation with mean wavenumber is weaker (though still significant). Of course, wave height and wavenumber are not completely independent, as often waves are limited in steepness ($Hk/\tanh(kd)$ is roughly constant). Wave height estimates were more robust than mean wavenumbers (which assumed a dispersion relation for waves over a sheared current, see *Zippel and Thomson* [2017]), and therefore may explain the difference in correlations. For

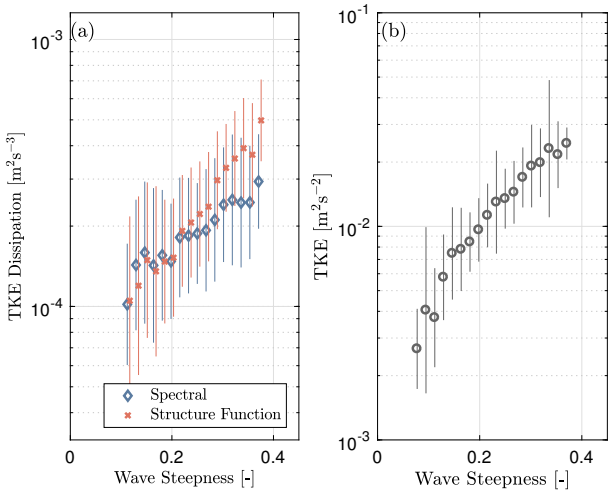

Figure 3.5: TKE and TKE dissipation rate estimates are depth averaged, binned, and plotted against finite depth wave steepness ($H_s k_m / \tanh(k_m d)$). Turbulence estimates vary nearly an order of magnitude over the measured range of wave steepnesses. Variations between structure function and spectral TKE dissipation rates in (a) are due to differences in the shape of each turbulence profile.

roughness length proportional to the wave height, $z_0/H_s = z_b$, the data yield the parameter constraint $z_b L/(C_\mu^0)^3 \approx 2.5$. This is consistent with typical model values, $L = \kappa = 0.4$, $(C_\mu^0)^3 = 0.55$ and $z_b = 1$, but allows for other combinations. Still, the results strongly support the wave height roughness length suggested in *Terray et al.* [1996], and moderately support the wavenumber roughness length suggested in *Drennan et al.* [1996] and in *Jones and Monismith* [2008]. The results do not support a constant roughness length, or more complicated variations such as *Gemmrich and Farmer* [1999]. The ratio q^3/ϵ has no correlation with drift speed, U, or drift speed normalized by the mean wave phase speed, U/C_p.

Estimates of length scale at depth are consistent with the values at the surface, but do not further constrain model parameters. Figure 3.7 shows estimated length scales, ℓ across all measurement depths, $\tilde{z}$, plotted against the expected relationship with depth below the free surface. The parameter values $L/(C_\mu^0)^3 = 2.5$, $z_b = 1$ (Fig. 3.7a) and $L/(C_\mu^0)^3 = 6.5$ and

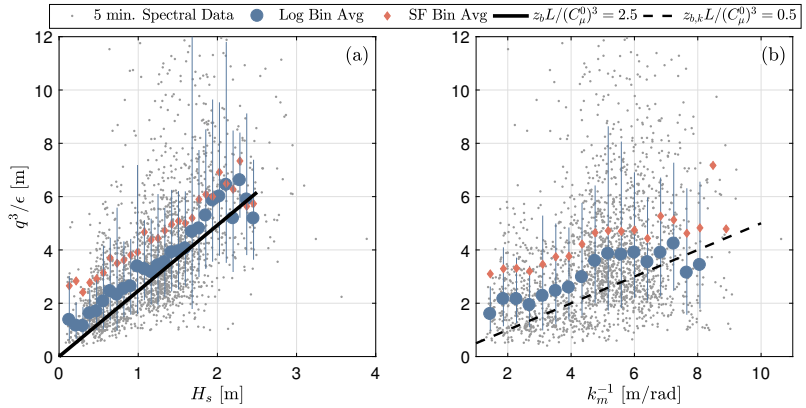

Figure 3.6: The relation of surface roughness length to wave parameters is tested with data at the approximate free surface, $\tilde{z} = 0$ through combination of Eqs. (3.2) and (3.3). Grey circles show 5-min averages of unscaled turbulent length q^3/ϵ, blue circles show log mean averages with one standard deviation in log space. Orange diamonds show the log mean averages estimated with structure-function derived TKE dissipation rates. The solid line shows the slope for $z_b L/(C_\mu^0)^3 = 2.5$, while the dashed line shows the slope with wavenumber scaled roughness length, $z_{b,k} L(C_\mu^0)^3 = 0.5$. The significant wave height (a), has a strong trend with turbulence data, while the mean wavenumber (b) has a weaker trend.

$z_b = 0.32$ (Fig. 3.7b) fit the log-normal mean of the results well. Since measurements have a limited depth range, most of the variation in the data is explained by wave height, which ranges from approximately $0.25 < H_s < 3.5$, where measured depths are limited to $\tilde{z} < 0.5$. This is highlighted in Fig. 3.7c, which shows that wave heights without depth variations are still correlated with turbulence results.

3.3.3 Decay Scales

Decay scales λ are estimated following the power law model (Eq. 3.7). Applying the full model requires estimating the magnitude surface input TKE flux, G, which is poorly constrained and not possible to directly estimate from these measurements. Instead of specifying G, the TKE and TKE dissipation rates are normalized by their measured near surface values, $q^2(0)$

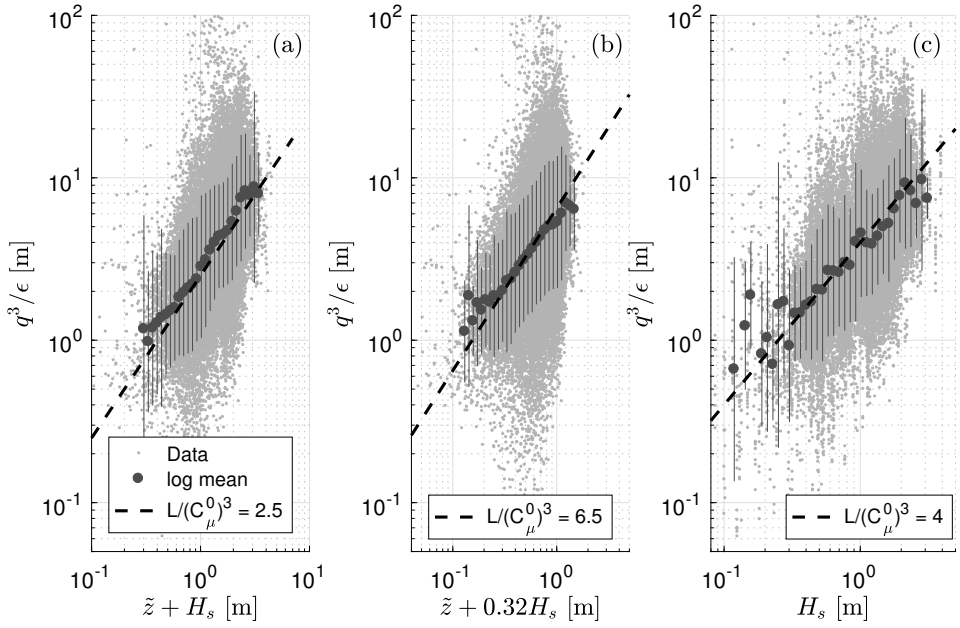

Figure 3.7: Estimates of turbulent length scale from turbulence measurements are are shown against the parameterization of linearly increasing length scale with distance from the surface with $z_0 = H_s$ (a), and with $z_0 = 0.32H_s$ (b). Black dots show the log mean, with horizontal bars showing one standard deviation in log space. The dashed black line shows a 1:1 correspondence. Most of the variation in $\ell(z)$ is explained by the wave height alone (c).

and $\epsilon(0)$ (rather than scaling them). The normalized values are expected to have the same decay scale, but may contain errors due to uncertainties in vertical placement z. For ϵ, this offset error is $[1 + (\Delta z/z_0)]^\lambda$, where Δz is the error in position. For Δz on the order of an Aquadopp bin size (0.04 m), we expect this vertical error to be small. Errors in normalized TKE and TKE dissipation rates are expected to be log distributed. The noise floor in such a normalization is therefore relative to the surface value. However, given surface values of $\epsilon \sim 10^{-3}$, and noise floors of $\epsilon \sim 10^{-5}$, we expect approximately two decades, with error increasing farther from the surface. Noise floor estimates of TKE are more complicated due to motion correction, however a similar range could be expected.

Normalized TKE and scaled depth (Fig. 3.8) show good agreement with power law decay

models. The more standard model parameters $L/(C_\mu^0)^3 = 2.5$, $z_b = 1$ (dotted line) do not fit the measurements well, and tend to over predict the amount of turbulence at depth. Decreasing the roughness length to $z_b = 0.5$ and $L = 0.3$ (dashed line) gives better agreement, but is no longer fully consistent with the measurements shown in Figs. 3.6 and 3.7. The parameter values $L = 0.21$, $C_\mu^0 = 0.32$, $z_b = 0.32$ (dashed dotted) do a reasonable job in matching the measurements, and hold with the relation $L/(C_\mu^0)^3 = 6.5$ from Figure 3.7b. The exponential solution also seems to fit the data well near the surface. However, the constants in the exponential solution are, again, relatively unconstrained. Taking $z_b L/(C_\mu^0)^3 = 4$ from Fig. 3.7c, and constraining $0 < L < 0.4$, we arbitrarily set $z_b = 0.1$ as the approximate location where the power law decay seems to dramatically lessen. A reasonable fit is achieved with $C_\mu^0 = 0.15$, $L = 0.135$.

Normalized TKE dissipation rates are shown against scaled depths in Fig. 3.9. Here, parameters $L = \kappa$, $C_\mu^0 = 0.55$, and $z_b = 1$ predict more dissipation at depth than is measured (similar to TKE in Fig. 3.8). The other sets of constants all do reasonably well to predict the measured dissipation rate profiles. Constants $L = 0.21$, $C_\mu^0 = 0.32$, $z_b = 0.32$ fit the TKE dissipation decay, TKE decay, and the length scale arguments (Figs. 3.7b and 3.8). This parameter set gives $\lambda = 3.6$, which is larger than the decay reported in *Terray et al.* [1996]. However, the scaling $(z/H_s)^{-2}$ still represents the data well for $0.1 < (z/H_s) < 1$, as shown by the red dashed-dotted line in Fig. 3.9. Therefore the decay $\lambda = 3.6$ is still consistent with previous studies over the measured depth range. This highlights the importance of the roughness length in the argument of the power law model, especially close to the surface. Estimates of normalized TKE dissipation from the structure function method are similar to those from the spectral method, but do show slightly reduced decays. Lastly, the exponential solution fits the top of the profile well, below which the power law relation, $(z/H_s)^{-2}$, appears to hold. The falloff of the bin averaged values at lower depths is related to the relative turbulence noise floor, and the horizontal definition of bins.

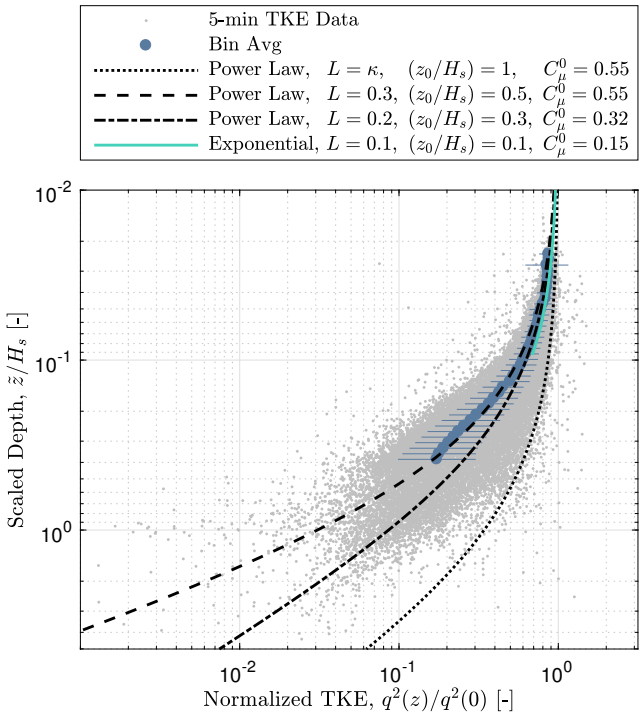

Figure 3.8: Normalized 5-min estimates of TKE are plotted against scaled measurement depth. Data are bin averaged in log space, with horizontal bars showing one standard deviation. The black lines shows the predictions from power law solutions for different sets of constants. The dashed and dashed-dotted lines used parameters consistent with Fig. 3.6a and Fig. 3.6b respectively. Lastly, the light blue line shows the exponential solution expected for a constant length scale, plotted for $z \leq z_0$. Binned data profiles do not extend lower than the estimated noise floor.

The parameter values $L = 0.21$, $C_\mu^0 = 0.32$, $z_b = 0.32$ are not arbitrary, but were found by minimizing the sum of log residuals between measurements and models via Eqs. (3.3) and (3.2), (3.4), and (3.5). Slight weighting was given to the normalized dissipation residuals because the similarity in the two estimations of dissipation increased confidence in the measurements.

3.3.4 Fronts and Buoyancy Scaling

Fronts are common in the vicinity of the river mouth, and these complicate the estimation of wave steepness used in Fig. 3.5. The fronts are associated with strong horizontal gradients in currents, dU/dx, and convergences where downwelling occurs. Such gradients are difficult to quantify with free drifting buoys alone, because the drifters rapidly move toward the convergence zone and stay within it, providing no current or wave information on either side. Thus, the buoy estimates are highly localized within these gradients. The data set includes a few cases where spatial information is available in the form of surface current maps derived from airborne interferometric Synthetic Aperture Radar (SAR) [*Farquharson et al.*, 2014]. Buoy 5-min drift positions are shown overlaid on a SAR composite velocity map in Fig. 3.10a, which is used as a case study of the interaction between the wave-breaking turbulence and the river plume.

The SAR velocity field is a composite of six aircraft passes over the estuary. Each pass took approximately 7 min to complete, so the surface velocity field shown in Fig. 3.10a evolved over a period of 42 min. This evolution, combined with calibration errors from pass to pass (< 10 cm s^{-1}) account for some of the variation seen in data collected during each track in the composite field. Other pass to pass differences may be ascribed to a surface velocity measurement bias that depends on the SAR viewing geometry in areas of large sub-resolution (meter scale) waves [*Thompson and Jensen*, 1993]. This bias has not been characterized for this data set due to the lack a comprehensive measurement of the surface

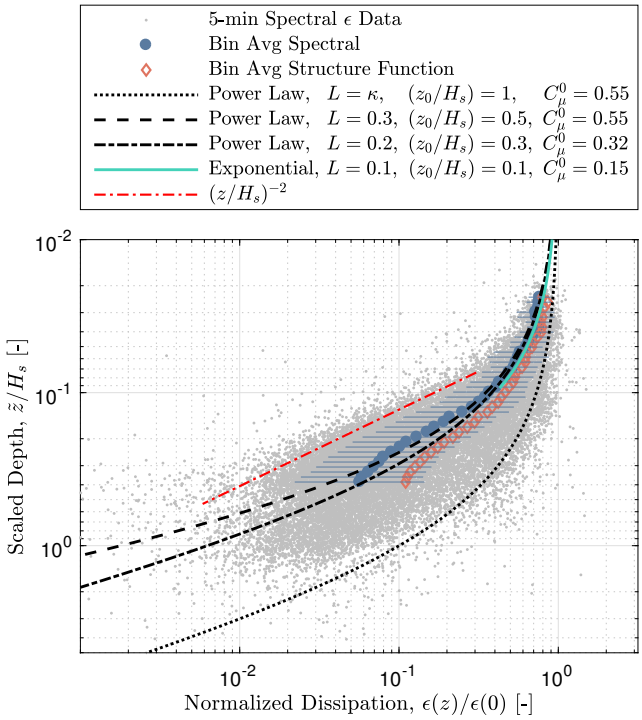

Figure 3.9: Normalized measurements of TKE dissipation rate are plotted against the scaled measurement depth. Blue circles show the log mean of estimates processed with the spectral method, and horizontal bars show one standard deviation. Orange diamonds show the binned log means of structure function estimates. The black lines shows the predictions from power law solutions, and the light blue line shows the exponential solution expected for a constant length scale. Binned data profiles do not extend lower than the estimated noise floor. The dashed-dotted red line shows the $\lambda = -2$ slope predicted by the *Terray et al.* [1996] scaling, offset vertically.

wave field (including breaking) throughout the domain. Areas of noisy measurements are due to low backscattered signal from the surface.

Despite these sources of noise, a front can be seen by the rapid spatial change in velocities in the SAR-derived velocity field (approximate Longitude -124.02, Fig. 3.10a). A large gradient in wave energy flux would be expected across such a current gradient, dU/dx, even on following currents, due to the rapid change in wave steepness required from conservation of wave action and dispersion [*Chawla and Kirby*, 2002]. The SWIFT buoys were visually confirmed to be caught in this front at approximate Longitude -124.04, which matches with tower based Radar measurements of the front (not shown). SAR measurements slightly lagged the timing of buoys in the convergence zone, and thus the front is not as visible at this leading edge in Fig. 3.10a. Measurements of wave breaking rate (Fig. 3.10b) and TKE dissipation rates (Fig. 3.10c) increased in tandem where the horizontal gradient in currents was largest. The increase in wave breaking turbulence at the front is consistent with the results of *Thomson et al.* [2014], where a similar example is provided from an ebbing front offshore (using a different case from this same data set). Unfortunately, a direct estimate the wave surface flux G used in Eq. 3.7 cannot be made for any of these cases, because the wave measurements are at the gradient (rather than across it). Still, the elevated turbulence associated with the waves can be compared to other sources of turbulence in the river mouth.

Sub-surface turbulence across plume fronts has been measured at similar levels to those presented here for the near surface (ϵ in the range of 10^{-4} to 10^{-3}), and this turbulence is typically attributed to shear production, which is opposed by stable buoyancy at a strong density interface [*Kilcher and Nash*, 2010; *Horner-Devine et al.*, 2015]. Therefore, it is worth investigating whether the surface turbulence ($O10^{-3}$) is not exclusively from wave breaking, and is affected by shear and buoyant effects that are expected in the absence of waves. In a similar manner, there are questions on the effect of wave-breaking turbulence on these estuarine forced (shear production and buoyancy) terms.

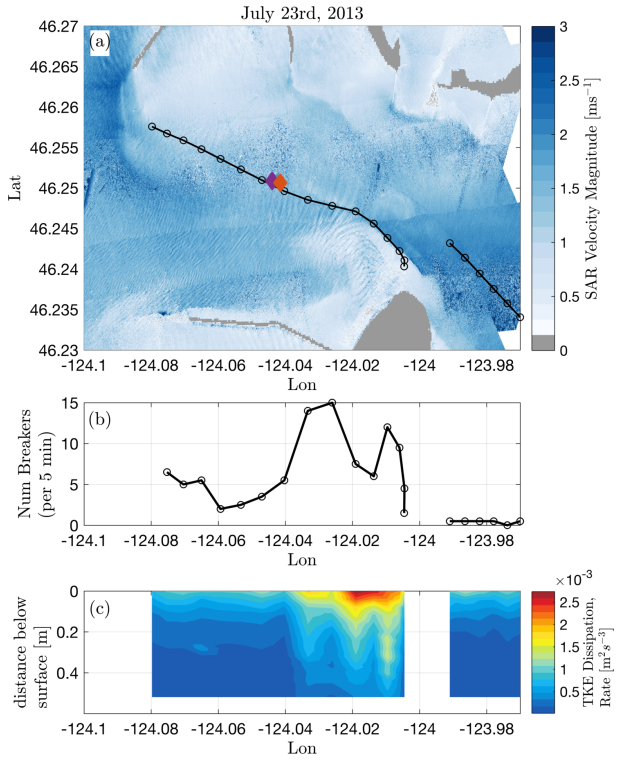

Figure 3.10: Data from a flooding drift deployment on 23 July 2013 are shown here. The magnitude of velocities estimated from airborne interferometric SAR are shown with drifter locations in (a). The drifters, moving left to right, enter a convergence zone, where the horizontal gradient in velocity is large. Measured wave breaking (b) and TKE dissipation rate (c) increase while the drifters are in the convergence zone. Throughout the drift, the buoy measured wind speed was relatively constant at $U_1 = 8$ m s^{-1}, and the relative depth was $H_s/d < 0.1$. Locations of CTD casts (Fig. 3.11) are shown with the purple and orange diamonds.

Here, we use the ratio of buoyancy flux to vertical diffusive transport to diagnose the relative importance of these effects. This ratio is approximated as,

$$\frac{B}{T} = \frac{\frac{g}{\rho_0}\langle \rho' w' \rangle}{\frac{d}{dz}\frac{\nu_t}{\sigma_t}\frac{dq^2}{dz}} \approx \frac{\nu_t^\rho N^2 H_s}{0.3G}\left(\frac{z}{H_s}\right)^2, \tag{3.13}$$

where N^2 is the buoyancy frequency, and ν_t^ρ is the diffusivity of density, such that the buoyancy destruction (production) is treated diffusively. This is similar to a Richardson number if the denominator is loosely thought of as kinetic energy (although it is actually the turbulent transport and is usually dominated by pressure work $\langle P' w' \rangle / \rho_0$). The vertical turbulent transport is scaled using *Terray et al.* [1996]. For small values of B/T, the buoyant effects can be assumed to be small, and the turbulence from wave breaking is likely unmodified by stratification effects. For large values of B/T the *Terray et al.* [1996] scaling is not valid, and therefore $B/T > 1$ would suggest buoyancy effects are important but would not quantify just how important. A similar ratio for shear production, P, to transport can be made if N^2 is replaced with S^2, and ν_t^ρ is replaced by ν_t in Eq. (3.13). If this term, P/T is small, it indicates that turbulence is created by wave breaking rather than shear production.

CTD casts were made on either side of the front during this case study using a YSI CastAway (cast locations shown in Fig. 3.10a). No direct estimates of vertical shear over the range of measured densities were made during this deployment, however a proxy velocity profile was taken from the mean profiles of Fig. 2.3. Profiles of density (Fig. 3.11a) are used to calculate stratification, N^2, and are shown along with the proxy estimate of squared shear, S^2 in Fig. 3.11b. For both river and ocean sides of the front, buoyant effects are 1-10 times larger than shear effects. To evaluate the approximate ratio of B/T (Fig. 3.11f), the surface TKE input $G = c_e u_*^2$ is estimated from the buoy measured wind speed [*Gemmrich et al.*, 1994], the diffusion of density is assumed to be $\nu_t^\rho = 10^{-2}$ m^2 s^{-1}, and $\nu_t = (0.25) * \nu_t^\rho$. In the top few meters, the ratio is small (0.1 or less), suggesting that wave-breaking turbulence is of first order importance. The ratio B/T is near unity until nearly 6 m depth, which also suggests that the surface sourced turbulence could affect mixing at the front. Near the top

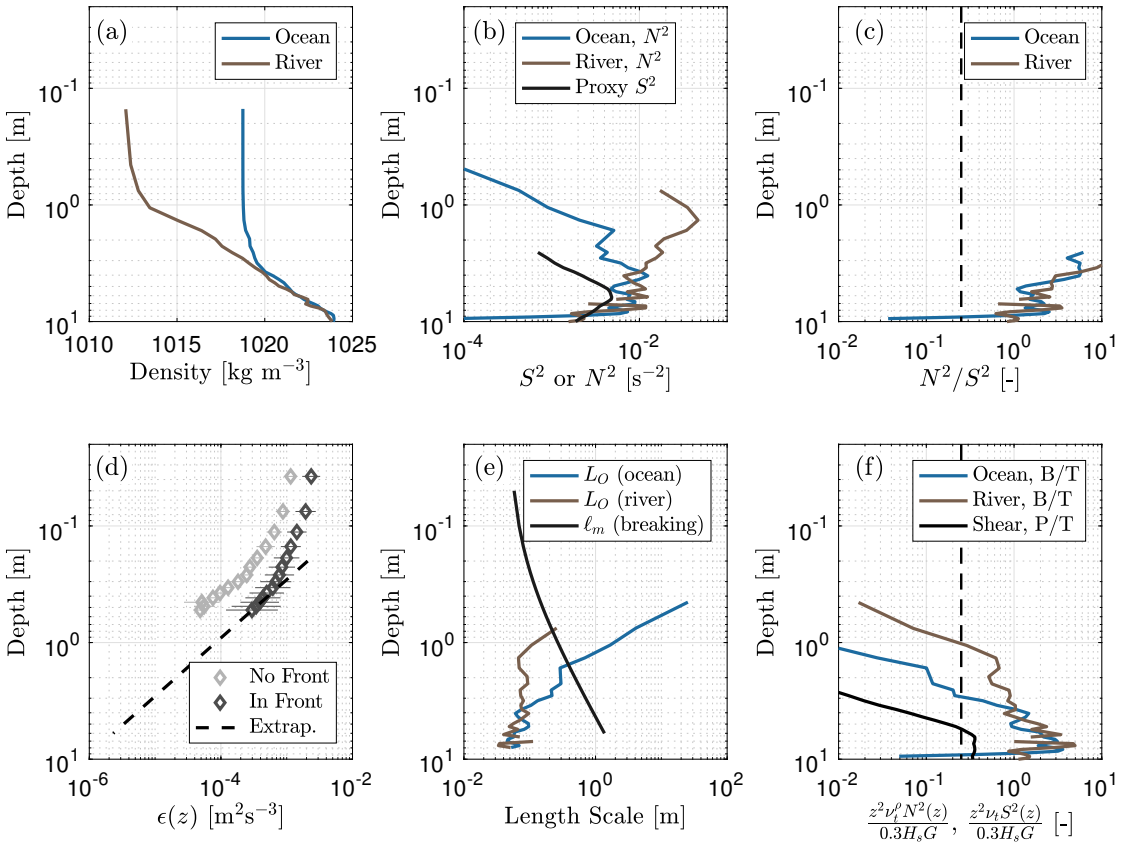

Figure 3.11: Profiles of (a) density (b) buoyancy frequency N^2 and Shear S^2, (c) the ratio of buoyancy to shear, (d) turbulence profiles measured before entering the front, and with drifters in the front, (e) estimates of length scales, and (f) the ratio of B/T and S/T are shown for the July 23rd front. Locations of the CTD casts are shown relative the drifter and SAR measurements with purple (ocean side) and orange (river side) diamonds in Fig. 3.10a. The velocity profile is taken from the mean profile with a similar surface drift (e.g., Fig. 2.3), because both drifters were in the up-looking configuration during this deployment. The extrapolated dissipation rate shown with the dashed black line in (d) is used to estimate the Ozmidov length scale, $L_O = \sqrt{\epsilon N^{-3}}$ in (e). The vertical dashed line in (c) and (f) shows the ratio 0.25.

of this layer, shear is still relatively small, as seen by both P/T, and N^2/S^2 (Fig. 3.11 c and f). Determining a critical value for the scaling of B/T is left for future studies with more comprehensive measurements of stratification (beyond the few case studies available in this dataset). Past studies have suggested shear-free turbulence can cause mixing via internal wave breaking, KH instability from large eddies, and splashing for local Richardson numbers (internal Richardson numbers, N^2h^2/q^2, or external Richardson numbers $\Delta\rho\ell/q^2$) near unity [*Fernando*, 1991; *Fernando and Hunt*, 1997], so this should be pursued.

A second estimate for the influence of buoyancy is made using the Ozmidov length scales in Fig. 3.11e. The Ozmidov length scale is defined $L_O \equiv \sqrt{\epsilon N^{-3}}$, and represents the smallest turbulent length scales affected by buoyancy. Profiles of dissipation rate in the front (Fig. 3.11d), are extrapolated to the depths of measured density, and used to estimate L_O, which is compared with the mixing length scale that best fit the turbulence measurements for the majority of the data set (i.e., $\ell_m = 0.21[z + 0.32H_s]$). Near the surface, mixing lengths are smaller than Ozmidov lengths, suggesting buoyancy is not affecting the turbulence at relevant scales. The fact that transition depths where $L_O = \ell_m$ match depths where $B/T \approx 0.25$ is consistent and encouraging, but coincidental due to the arbitrary choice of ν_t^ρ.

The example presented here shows a single case where diffusion is large compared to buoyancy and a proxy for shear near the surface, in a layer that is thin compared with plume thickness [typically $\sim$ 10 m at the Columbia River, *Kilcher and Nash*, 2010]. Therefore, it is likely that turbulence within 50 cm of the free surface is generally unaffected by buoyancy and shear production for the majority of this dataset, and the diffusion-dissipation balance shown in the previous sections is expected to be valid. The data presented in this case study also suggest a region below the measurements ($\tilde{z} < 50$ cm) where wave sourced turbulence (transport) and river effects (buoyancy and shear production) overlap and interact.

3.4 Discussion

3.4.1 Model Parameters

Specification of roughness z_0 length is clearly important in characterizing turbulence near the ocean surface, however it has been left relatively open as a model parameter in the literature. *Burchard* [2001] describe a zone of bubble entrainment, where the multi-phase bubble flow is not resolved for Reynolds Averaged Navier-Stokes (RANS) equations. Wave breaking is intermittent and highly localized, with bubble plumes decay on the order of seconds [*Callaghan et al.*, 2013]. Therefore, this region is not an idealized horizontally uniform bubble sheet. Still, many models avoid this clearly difficult region, by setting the origin one roughness length below the mean sea surface, $z - z_0$. The direct physical implication of Eq. (3.2) is that z_0 is the length scale of turbulence introduced by the wave breaking events. This length can be thought of either as that imposed by the front leading bubble plume [*Longuet-Higgins and Turner*, 1974], or the spatial extent of the vortex tube created at the horizontal edges of the breaker [*Clark et al.*, 2012]. In the former case, the physical justification for $z_0 \propto H_s$ can be seen through the work of *Duncan* [1981], where the length of the aerated fluid on a breaking wave is related to wave height. This physical justification, under the same measurements in *Duncan* [1981], could also be related to the scales k^{-1} and C_p^2/g (where C_p is wave phase speed). In the latter case, *Pizzo and Melville* [2013] showed that the circulation under breaking waves can be scaled with both wave steepness and wave phase speed. Under this framework, the turbulent length scales in a RANS model may be physically justified in a similar sense with wave parameters H_s, k^{-1} and C_p. It is possible this study only finds better agreement between roughness length and H_s due to measurement accuracy and precision, and physical justifications for scaling the vertical coordinate by k^{-1} or C_p^2/g are no less valid.

As discussed in *Burchard* [2001]; *Gerbi et al.* [2009], setting $L < \kappa$ suggests the turbulent

length scale grows more slowly in the dynamic surface boundary layer than in rigid boundary layers. *Gerbi et al.* [2009] evaluated the ratio $L/(C_\mu^0)^3$, but did not distinguish between the two parameters, finding the ratio was smaller than expected for a rigid boundary layer, $L/(C_\mu^0)^3 < 2.5$. However, as shown in Fig. 3.7a and Fig. 3.7b, this ratio is also sensitive to choice of roughness length. Therefore, the much larger $L/(C_\mu^0)^3 \approx 6.5$ is only justified here through smaller choice of z_0. The physical meaning of (C_μ^0) is even more nebulous, but, as it is associated with ℓ, it can be attributed to the roll-off wavenumber in the power spectrum of turbulent velocities [*Tennekes and Lumley*, 1972]. The measured spectra of this study have too few degrees of freedom to easily estimate such a roll-off wavenumber (especially given the relatively new application of the inertial-advective subrange), however future studies may use such a relation to better constrain C_μ^0. Typically C_μ^0 is a relatively established constant, so it is strange that it must be modified to achieve reasonable fits the measured data in Figs. 3.7, 3.8, and 3.9. While it's possible that the relation between length scale, velocity, and dissipation are physically modified by the wave field, it is also worth considering that the assumption of vertical diffusive transport is not accurately representing the near-surface physics, since strange tuning of model constants is needed to fit data. Intermittence of breaking, horizontal heterogeneity, and down gradient advection of TKE from vertical velocity may all play a role.

The success of the *Terray et al.* [1996] scaling below $\tilde{z}/H_s = 0.1$ and the exponential solution for the top of the water column (Fig. 3.9) leads naturally to a piecewise scaling for dissipation referenced to $\tilde{z}$-coordinates,

$$\frac{\epsilon(\tilde{z})H_s}{G} = \begin{cases} A\exp(-\alpha\tilde{z}/H_s), & \frac{\tilde{z}}{H_s} \leq 0.1 \\ 0.3\left(\frac{\tilde{z}}{H_s}\right)^{-2}, & \frac{\tilde{z}}{H_s} > 0.1. \end{cases} \tag{3.14}$$

Appropriate choice of α could then rectify the range of decay scales ($1 < \lambda < 2$) found very near the surface [e.g., *Gemmrich*, 2010; *Sutherland and Melville*, 2015; *Thomson et al.*,

2016]. The constant A must be a function of decay scale such that the piecewise function is consistent at the interface, $A = 0.3 z_b^{-2} \exp(\alpha z_b)$.

3.4.2 Reference Frames

Some discrepancy in reported slope λ may be attributed to choice of reference frames. As reported in *Thomson et al.* [2016], turbulence lasting longer than one wave period is moved vertically with the free surface, and thus fixed frame measurements capture an effective average of the turbulence at depths varying from the free surface. In other words, the advection of a depth varying turbulent field across fixed frame instruments creates a complicated mapping between z referenced coordinates and $\tilde{z}$ referenced coordinates. *Lumley and Terray* [1983] investigated a similar effect, where the advected turbulence is assumed uniform across wave orbitals. Given that turbulence decay is appreciable over a wave height (Figs. 3.7, 3.8, and 3.9), this assumption of vertically homogenous turbulence across a wave particle excursion is likely not valid near the surface, where particle excursions (below the free surface) are roughly equal to sea surface deviations. Here, we attempt a simple numeric estimation for the orbital advection of a non-uniform field. The key simplification is the assumption that the TKE dissipation rate as a 1-D field with a robust average in time. A more realistic approach would evaluate the effect on the velocity field (as was done in *Lumley and Terray* [1983]; *Rosman and Gerbi* [2017]), rather than directly on the higher statistical moments of the velocity field (i.e., the TKE dissipation rate). Such a description would require knowledge of how the velocity field statistics vary with depth *a priori*.

Following *Andrews and McIntyre* [1978], we take a Taylor Series expansion of the $\tilde{z}$-coordinate dissipation function, $\epsilon_*(\tilde{z})$ about the coordinate ζ. Here, we approximate the wave orbital particle excursions by setting $\zeta = \eta$, which is valid for long waves relative to the depth range z. In this way, we can relate the two reference frames as a function of

coordinate, and sea surface statistics.

$$\langle \epsilon_*(z) \rangle \approx \langle \epsilon_*(\tilde{z}) \rangle + \langle \eta \epsilon'_*(\tilde{z}) \rangle + \langle \frac{1}{2}\eta^2 \epsilon''_*(\tilde{z}) \rangle + \langle \frac{1}{6}\eta^3 \epsilon'''_*(\tilde{z}) \rangle + \langle \frac{1}{24}\eta^4 \epsilon'''_*(\tilde{z}) \rangle, \tag{3.15}$$

where $\epsilon_*(z)$ is the normalized dissipation function, $\langle\rangle$ is a time average operator, $\tilde{z}$ is the surface referenced vertical coordinate, such that $\tilde{z} = z - \eta$, and $'$ denotes differentiation with respect to z. Assuming η is Gaussian distributed, the first and third statistical moments are zero,

$$\langle \epsilon_*(z) \rangle \approx \langle \epsilon_*(\tilde{z}) \rangle + \frac{1}{2}\langle \eta^2 \rangle \langle \epsilon''_*(\tilde{z}) \rangle + \frac{1}{24}\langle \eta^4 \rangle \langle \epsilon'''_*(\tilde{z}) \rangle, \tag{3.16}$$

such that only the sea surface variance and kurtosis are needed. In this way, one can relate the $\tilde{z}$-coordinates and z-coordinates mean dissipation rates, (i.e., $\langle \epsilon_*(\tilde{z}) \rangle$ to $\langle \epsilon_*(z) \rangle$). Assuming a power law form, the non-dimensional dissipation rate $\epsilon_*(\tilde{z}) = (1 + \tilde{z}/z_0)^{-\lambda}$, the second and fourth derivatives are

$$\epsilon''_*(\tilde{z}) = \frac{\lambda(\lambda+1)}{z_0^2}\left(1 + \frac{\tilde{z}}{z_0}\right)^{-\lambda-2} \tag{3.17}$$

$$\epsilon''''_*(\tilde{z}) = \frac{\lambda(\lambda+1)(\lambda+2)(\lambda+3)}{z_0^4}\left(1 + \frac{\tilde{z}}{z_0}\right)^{-\lambda-4}. \tag{3.18}$$

This representation does not account for the partial drying of z-coordinate measurements, which are exposed to air in wave troughs. Given that ϵ_* represents a rate, the non-wetted time must be accounted for in the average. Here, a more general, probabilistic solution accounts for this issue,

$$\langle \epsilon_*(z) \rangle = \int_{-\infty}^{z} P(\eta)\epsilon_*(z - \eta)d\eta, \tag{3.19}$$

where $P(\eta)$ is the distribution of sea surface elevations. Unfortunately, this integral is not easily solved analytically for many probability distribution functions. A numerical solution Eq. (3.19) assuming Gaussian $P(\eta)$ is shown in Fig. 3.12, plotted alongside the Taylor Expansion approximate solution, and the power law referenced to $\tilde{z}$-coordinates with constants $L = 0.21$, $C_\mu^0 = 0.32$, $z_b = 0.32$. Choice of η over the wave orbital particle excursions, ζ,

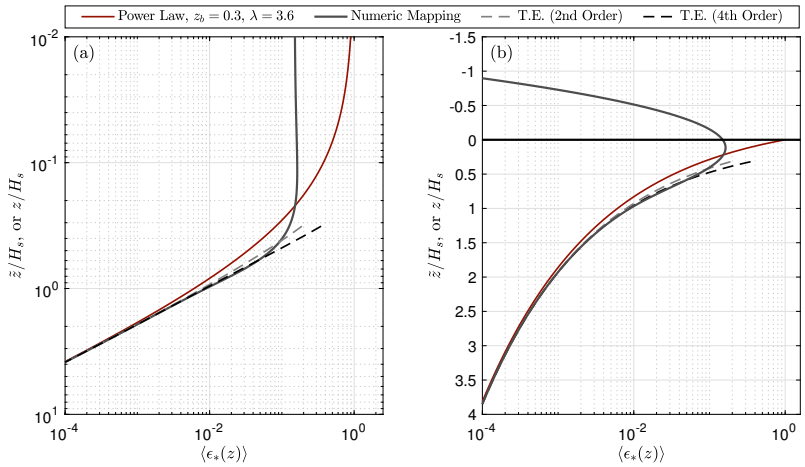

Figure 3.12: The power law solution, shown in brown is converted to a fixed frame average (black) using the naive probabilistic mapping (Eq. 3.19). Slopes to a 2nd and 4th order are shown in dashed grey and black. The solutions are shown on a vertical log scale (a) and a linear vertical scale in (b) to highlight the existence of average TKE dissipation rates above the mean sea surface.

simplifies much of the analysis, but likely adds more turbulence at depth in the z-coordinate reference since wave orbital excursions are necessarily smaller than the surface displacements, $\zeta \leq \eta$. The assumption of a Gaussian distributed sea surface elevation does not describe non-linearities common in wave fields, but is often a reasonable approximation [see, for example, *Schwendeman and Thomson*, 2017, Fig. 6].

A few notable features appear in the z-coordinate numeric mapping shown in Fig. 3.12. First, on a logarithmic scale (Fig. 3.12a), the shape of the mapping is qualitatively similar to the *Terray et al.* [1996] model. In particular, there is a nearly constant layer of dissipation above a power law decay region due to the fractional coverage of water in the region, and thus must be accompanied by a net TKE dissipation above the mean sea surface. Integration of the fixed-frame dissipation profile shows 30% of the total dissipation exists above the mean sea surface, and 50% exists above $z/H_s = 0.6$ (the assumed breaking layer depth in *Terray et al.* [1996]). The conversion also suggests measurements of λ in the fixed reference frame

could decay faster than those in the moving reference frame below the breaking layer depth. Due to the number of simplifications used, the numeric mapping presented here is only intended as a rough estimate. It does, at least, provide results qualitatively similar to the direct coordinate mapping of *Thomson et al.* [2016], wherein the surface-following estimates are maximum, on average, at the mean sea-level (i.e., similarities between Fig. 3.12 herein and Figure 2f,h in *Thomson et al.* [2016]).

3.5 Summary

Measurements of waves and near surface turbulence at the Mouth of the Columbia River were compared with existing analytical models and turbulence scalings. The vertical dependence of the turbulence is consistent with the analytic model, which assumes a balance of diffusion and dissipation. TKE dissipation rates also follow the canonical $\lambda = 2$ power law decay, but for a range of scaled depths different than those originally proposed. Further, turbulent length scales estimated from measurements are seen to increase linearly with depth, supporting the common model assumption.

The model is sensitive to the choice constants, primarily the roughness length. Measurements suggest this roughness length is proportional to the significant wave height, perhaps because of advection by wave orbital motions. We find that the method used in processing turbulence data moderately changes the result; the spatial structure function blurs the vertical gradient, yielding slightly decreased decay scales.

A mapping of coordinates from a reference frame moving with the free surface to a reference frame fixed at the still water level is discussed. This mapping is dependent on the sea surface statistics, and may help explain some of the discrepancies in reported power law decay exponent. It is in some ways surprising that near-surface turbulence at an active river inlet fits the deep water scaling so well. This is likely due to the large wave energy fluxes in the region, as well as a thick river plume.

Chapter 4

AIR-SEA INTERACTIONS IN THE MARGINAL ICE ZONE

4.1 Introduction

Waves are becoming increasingly important in the Arctic ocean, which has experienced a significant retreat of the seasonal ice extent [*Comiso and Nishio*, 2008; *Comiso et al.*, 2008]. *Thomson and Rogers* [2014] showed that the increased fetch in the Beaufort and Chukchi Seas is associated with large wave heights, far beyond what had previously been observed. Their work extends measurements from satellite data [*Francis et al.*, 2011] and model hindcasts [*Wang et al.*, 2015] which have shown a statistically significant increase in mean wave heights for this region over the past decades. Increased wave heights are of particular significance, as *Kohout et al.* [2014] recently found that the attenuation rate of large waves in ice is linear, as opposed to the exponential decay typically assumed. Thus, as wave energy increases throughout the Arctic, waves are likely to propagate farther into the ice.

Increased wave energy in the Arctic ice pack has implications beyond accelerated ice break-up. Waves have been shown to increase the exchange of momentum, heat and gasses between ocean and atmosphere, as recently reviewed by *D'Asaro et al.* [2014]. The pathway of wave energy into ocean mixing is less clear, but is often attributed to wave breaking very near the surface [*Agrawal et al.*, 1992; *Craig and Banner*, 1994; *Terray et al.*, 1996] and to Langmuir turbulence lower in the surface layer (as reviewed by *Thorpe* [2004]). Turbulence has particular importance for gas transfer, where the turbulent kinetic energy (TKE) dissipation rate at the ocean surface is commonly used to estimate gas transfer velocity (as originally proposed by *Lamont and Scott* [1970], *Lamont and Scott* [1970], and more recently employed by *Zappa et al.* [2003], *Zappa et al.* [2003], and *Loose et al.* [2014], *Loose et al.*

[2014]). In addition to mixing, waves provide the roughness which determines drag [*Chalikov and Belevich*, 1993], and thus sea state modifies air-sea momentum exchange. Exchanges of momentum, heat, and gasses are of particular importance in regions of partial ice cover, as the Arctic may be in transition from an ocean driven by thermohaline processes to one driven by atmospheric forcing [*Rainville et al.*, 2011].

Sparse measurements of waves in ice make parameterization of air-sea interactions in partial ice cover difficult, and therefore models of air-sea interaction often use open water parameterizations for waves (e.g., for air-ocean drag in *Martin et al.*, 2014). However, waves in ice are both damped and scattered [*Wadhams et al.*, 1986, 1988; *Squire*, 2007]. Therefore, it is likely that changes in the wave field alter air-sea exchanges in partial ice cover, such that they may be dramatically different from open water values.

4.1.1 Radiative Transfer Equation

The radiative transfer equation describes the evolution of wave energy per unit frequency, $E(f)$, as balanced by source and sink terms:

$$\frac{dE(f)}{dt} + \mathbf{c_g} \cdot \nabla E(f) = S_{wind} - S_{dis} + S_{nl} - S_{ice}. \tag{4.1}$$

Here, f is the intrinsic wave frequency, ∇ is the horizontal derivative operator, $\mathbf{c_g}$ is the wave group velocity, S_{wind} is the wind input term, S_{dis} is the wave dissipation term, often associated with wave breaking, S_{nl} describes energy transfers between frequencies, and S_{ice} governs wave-ice interaction. The wave-ice interactions can be both conservative (i.e., scattering) and non-conservative (i.e., damping). Typically, the energy spectrum, $E(f)$ and source/sink terms, S, are functions of both frequency and direction $E(f, \theta)$, $S(f, \theta)$. For this study we used the one dimensional variance spectrum $E(f)$, and source/sink terms $S(f)$.

Of these sources and sinks, S_{wind} can be measured directly, and is dependent on the wave action density, radian frequency $\omega = 2\pi f$, and a dimensionless parameter β [*Tolman and*

Chalikov, 1996],

$$S_{wind} = \beta\omega E(f). \tag{4.2}$$

β can be estimated from co-temporal measurements of pressure and wave height [*Plant*, 1982], and has been shown to be dependent on the wave phase speed, c, the difference in direction of the wind and the waves, θ_r, and the wind stress, either through u_* or a wind speed and drag coefficient. *Plant* [1982] parameterized β as:

$$\beta = (0.04 \pm 0.02)\left(\frac{u_*}{c}\right)^2 \cos(\theta_r). \tag{4.3}$$

Hence, the wind input term, S_{wind}, can be estimated with wave spectral measurements and directional wind stress measurements.

Terray et al. [1996] estimated the total mechanical energy flux from the wind to the waves by integrating the wind source term in frequency,

$$F = \rho g \int S_{wind} \mathrm{d}\omega = \rho g \int \beta\omega E(\omega) \mathrm{d}\omega, \tag{4.4}$$

(where ρ = density and g = gravitational acceleration) and then assumed that this flux into the waves was equal to the TKE flux from the waves into the ocean surface. This is a local balance, similar to the equilibrium defined by *Phillips* [1985]. *Terray et al.* [1996] successfully used flux, F, and the significant wave height, H_s, in open water to normalize the depth-dependent turbulent dissipation rate, $\epsilon(z)$ below the surface. In the absence of full wave spectral measurements, the energy flux into the wave field can be approximated as the wind stress multiplied by an effective transfer velocity, $F = \tau c_{eff}$ [*Gemmrich et al.*, 1994]. Subsequently, *Terray et al.* [1996] showed c_{eff} to be a function of wave age. In effect, the transfer velocity is a bulk representation of the wave spectral information and momentum transfer function, as included in Equation 4.4.

The ice source/sink, S_{ice}, primarily governs the decay of wave energy with distance from the sea-ice edge (*Squire*, 2007, and references therein). These decay rates are typically

exponential for waves less than 3 m [*Wadhams et al.*, 1986; *Kohout et al.*, 2014], occurring over scales longer than the scales of wave lengths (i.e., decays over tens to hundreds of kilometers, compared with wavelengths that are typically tens to hundreds of meters). Thus, the wave energy damping in S_{ice} is set mostly by non-local parameters: the open water wave energy levels, the horizontal distance from the ice edge, and the ice properties.

In contrast, the more localized wind source term, S_{wind}, is the focus of this paper. Observations of winds, waves, and ocean turbulence in the marginal ice zone are presented with a focus on local wind input to waves and subsequent ocean surface turbulence. Description of the methods and instrument deployments is followed by presentation and discussion of the bulk measurements, wave spectra, spectral directions, and turbulent dissipation rate profiles, including a rough estimate of the air-ocean drag coefficient in partial ice cover.

4.2 Methods

4.2.1 Cruises and Deployments

Data were collected from two research cruises, on the R/V *Ukpik* (July 25th to August 2nd, 2014) in and out of Prudhoe Bay, AK, and on the *Norseman II* (September 26th - October 3rd) from Wainwright to Prudhoe Bay, AK. Shipboard observations included wind measurements and video recordings of sea ice. In addition, buoy observations of wave spectra and TKE dissipation rate were collected on July 30th from the R/V *Ukpik* (Figure 4.1a), and on October 2nd and 3rd from the *Norseman II* (Figure 4.1b). Two buoys were left to drift between the cruises, but do not have co-located shipboard measurements of wind stress and ice. One of the unaccompanied drifting buoys encountered ice on August 31st, 2014 (Figure 4.1c).

On July 30th, a Datawell Waverider buoy was deployed in open water, while a SWIFT buoy was progressively moved to areas of larger ice coverage within 1 km of the open water buoy. On October 2nd, one SWIFT buoy was deployed in ice-free water, while a second

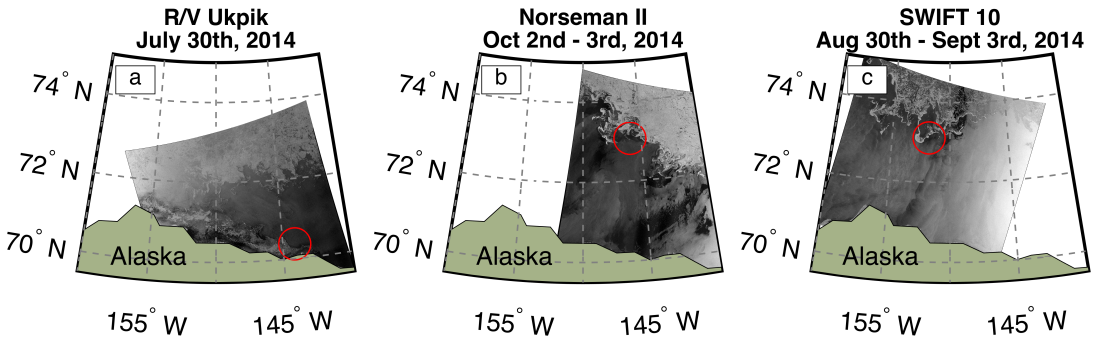

Figure 4.1: Data were collected on two cruises in the summer of 2014: from the R/V *Ukpik* in July (a), and from the *Norseman II* in September/October (b). Unaccompanied buoys deployed from the *Ukpik* encountered ice on August 31st (c). Red circles overlaid on Radarsat-2 SAR images taken within 1 day of deployments show approximate locations of measurements relative to ice. SAR from NIC, processed by CSTARS and curated by Luc Rainville.

SWIFT buoy was deployed in 1% ice, eventually free drifting into 50% brash ice. The average distance between buoys on October 2nd was less than 1 km, with a maximum distance roughly 1.5 km. Of the two unaccompanied buoys, only one encountered ice, while the other stayed in open water at a range of roughly 20 km. The deployments described above, therefore, have co-temporal in-ice and ice-free wave measurements, along ice-perpendicular lines. The October 2nd deployment only has co-located ship-based measurements (wind stress and ice fraction) with the buoy in the ice for the first and last sampling period of the deployment, because the ship moved away to continue other sampling between deployment and recovery.

Finally, a similar deployment of several hours was conducted on October 3rd, 2014. However, a freezing event took place, such that the fractional ice coverage became difficult to define, with nearly 100% of the water surface covered with grease/shuga ice while small waves were present.

4.2.2 Wind Stress

Wind speeds were measured from a shipboard sonic anemometer sampling at 10 Hz. Wind stress was estimated using the inertial method of *Large and Pond* [1981], as described by *Yelland et al.* [1994]. Wind data were processed in 10-minute intervals. Wind directions originating from the ship's stern were often contaminated by the ship's bridge, and were excluded from analysis. The velocity time series were despiked using the phase-space method of *Goring and Nikora* [2002], as implemented by *Mori et al.* [2007], with cubic interpolation replacement. Wind velocity spectra for the horizontal components $E_{wind,uu}$ and $E_{wind,vv}$ were estimated using the Welch method, where 512 point windows were de-trended, tapered with a Hamming window, and averaged with 75% overlap giving approximately 20 degrees of freedom. Frequencies between 1 and 4 Hz were confirmed to have an $f^{-5/3}$ dependence, consistent with an inertial subrange. Mean correlations with $f^{-5/3}$ spectral slopes in the inertial subrange were $R^2 = 0.85$, and all the spectra used were correlated at least $R^2 > 0.7$.

The ensemble spectra were fit to $f^{-5/3}$, and the air-side dissipation was estimated assuming advection of a frozen field (Taylor's hypothesis) at a speed U, such that

$$u_* = \left(\kappa \left(\frac{\left\langle E_{wind}(f) f^{5/3} \right\rangle}{K \left(\frac{U}{2\pi}, \right)^{2/3}} \right)^{3/2} z_{wind} \right)^{1/3}, \tag{4.5}$$

where here, $\langle\rangle$ represents an average from $f = 1$ to 4 Hz, $K = 0.55$ is the horizontal Kolmogorov constant, $\kappa = 0.4$ is the von Karman constant and z_{wind} is the measurement height above the still water level (10.3 m for the *Norseman II*, 4.5 m for the R/V *Ukpik*). This representation assumes neutral stability, which is justified by the similarity of water, air, and sea-ice temperatures during the observations (typically within 5° C).

The unaccompanied buoy did not have co-located measurements from a sonic anemometer. Therefore, a drag coefficient of $C_d = 1.5 \times 10^{-3}$ is assumed, and the friction velocity is found with $u_* = C_d^{1/2} U_{10}$.

4.2.3 Wave Spectra

Wave spectra were measured from surface tracking SWIFT buoys [*Thomson*, 2012]. Velocity and acceleration data from a 9-axis IMU (Microstrain 3DM-GX3-35) collected at 4 Hz were used to make wave spectra. The horizontal velocity and vertical acceleration time series were filtered with a high-pass RC filter in the time domain. Horizontal velocity spectra were found using the Welch method, where the time series is split into 256 second windows with 75% overlap; a Hamming taper was applied to each window, and then the windows were averaged together, giving each 10-minute spectrum approximately 28 degrees of freedom. Wave energy spectra were estimated using linear theory, which relates horizontal wave orbital velocities to surface elevation, a method developed by *Herbers et al.* [2012]:

$$E(f) = \frac{E_{UU}(f) + E_{VV}(f)}{(2\pi f)^2}, \tag{4.6}$$

where $E(f)$ is the wave energy spectrum in $\mathrm{m}^2\ \mathrm{Hz}^{-1}$, $E_{UU}(f)$ and $E_{VV}(f)$ are the horizontal velocity spectra, and f is intrinsic wave frequency.

The acceleration spectra were used as a quality control for the wave orbital shapes, and to estimate the wave directional moments. As described in *Herbers et al.* [2012], the directional moments are found from,

$$\begin{bmatrix} a_1 \\ b_1 \end{bmatrix} = \begin{bmatrix} Q_{xz} / \sqrt{E_{zz}(E_{xx} + E_{yy})} \\ Q_{yz} / \sqrt{E_{zz}(E_{xx} + E_{yy})} \end{bmatrix}, \tag{4.7}$$

where Q_{xz} and Q_{yz} are the quadrature-spectra of horizontal and vertical displacements. The wave direction and directional spread are then found from the directional moments,

$$\theta(f) = \arctan(b_1/a_1), \tag{4.8}$$

and

$$\sigma_\theta(f) = \sqrt{2(1 - \sqrt{a_1^2 + b_1^2})}. \tag{4.9}$$

4.2.4 Turbulence

Turbulent dissipation rates in the upper half meter of the ocean were estimated using the second order structure function of velocities recorded from a Nortek 2 MHz Aquadopp HR mounted underneath the SWIFT drifters [*Thomson*, 2012]. Velocities, $u(z)$, recorded at 4 Hz, in 4-cm bins were processed in 10-minute bursts. The structure function, defined as,

$$SF(z) = \langle [u(z) - u(z+r)]^2 \rangle, \tag{4.10}$$

is related to turbulent dissipation through,

$$SF = C_v^2 \epsilon^{2/3} r^{2/3}, \tag{4.11}$$

where here, $\langle\rangle$ represents a time average, $C_v^2 \approx 2.1$ is a constant, ϵ is the turbulent dissipation rate, and r is the separation distance between measurements [*Wiles et al.*, 2006]. Dissipation rates are found by fitting the structure function to a $r^{2/3}$ dependence, such that $SF(z) = B(z)r^{2/3} + N$, where N is the expected doppler noise offset. The slope coefficients, $B(z)$, can be used to estimate the turbulent dissipation rate by

$$\epsilon(z) = C_v^{-3} B(z)^{3/2}. \tag{4.12}$$

The Aquadopp was mounted such that beam #1 was oriented 60 degrees counterclockwise from the buoy's wind vane. The buoy orients vane into the wind, such that this beam is, on average, 60 degrees counterclockwise with the mean motion direction, avoiding measurement of the buoy's own wake. Average beam orientations in ice were typically similar to those in open water (i.e., changes in wave direction due to ice do not appear to change the buoy orientation, which would otherwise potentially contaminate the turbulence measurements).

4.2.5 Ice Fraction

Ice fractions were estimated from shipboard video observations using a bullet camera (Sony 1/3" ExView B/W CCD) with a horizontal resolution of 600 TVL. On the R/V *Ukpik*, the

camera was mounted above the wheelhouse, 4 m above the ocean surface, looking forward of starboard beam. On the R/V *Norseman II*, the camera was mounted at 10.3 m above the ocean surface, looking forward. Data collected at 15 Hz were subsampled to 1 Hz for processing. The camera was stabilized mechanically by a pan and tilt, and images were further stabilized in processing with the horizon method of *Schwendeman and Thomson* [2015a].

Images were rectified to real world coordinates, and filtered with a top hat filter to even illumination and help identify edges. Ice was identified as pixels above the 20% intensity threshold. Ice fraction was estimated as the area of thresholded pixels over the total number of pixels. Floe areas were estimated using MATLAB's *bwlabel* and *bwarea* functions. Example images from the *Ukpik* on July 30th and the *Norseman II* on October 2nd are shown (Figure 4.2).

Sun glare often caused spuriously high ice fractions, and would result in a large number of small area flows. Therefore, identified areas of less than three pixels were not included in ice estimates. The 1-Hz ship-based ice estimates were matched with the 10-minute SWIFT buoy bursts by taking the mean fraction and floe area observed within 200 m and 5 minutes of the centered buoy location and time. Therefore, the total area used in estimating ice fraction extents beyond the roughly (15 m x 15 m) and (40 m x 40 m) footprints shown in individual frames (Figure 4.2c and d). However, the total area considered for each ice fraction measurement is small when compared to even high resolution model grid cells (typically between 3 and 30 km). On October 2nd, when no co-located, co-temporal ship-based measurements of ice fraction were available, the fraction was taken in a nearest neighbor interpolation guided qualitatively by the images from a camera onboard the buoy. The buoy's onboard camera did not have a large enough field of view for an accurate, independent, ice fraction measurement, but qualitatively compared well with the nearest ship measurements.

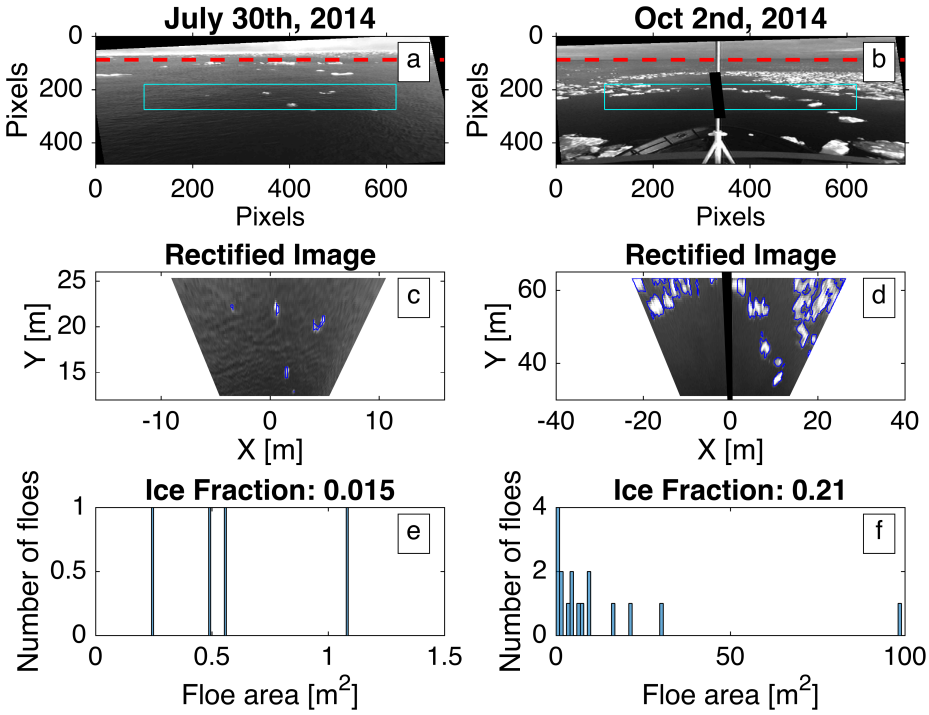

Figure 4.2: Examples of video processing from from the *Ukpik*, July 30th, 2014 (left), and from the *Norseman II*, October 2nd, 2014 (right), deployments are shown above. The stabilized images from the horizon-finding algorithm are shown in (a) and (b), with the identified horizon in red, and the region of interest outlined in teal. An image mask covered a guy-wire centered in the *Norseman II* camera's view frame (b). Panels (c) and (d) show the image rectified to real world coordinates, and filtered with a top hat filter. The blue outlines show the 20% pixel intensity contours. Panels (e) and (f) show histograms of the estimated floe areas, and the fraction of ice coverage in the image.

4.3 Results

Wind speeds, wave heights, energy-averaged wave periods, and ice fractions are shown in Figure 4.3 for the deployments on July 30th, October 2nd, and for the unaccompanied buoy shortly before and after it encountered ice on August 31st. For each deployment, a nearby open water buoy provides context for the relative changes in bulk wave parameters due to ice. In general, the trend is decreased wave heights and increased averaged periods relative to open water values. On July 30th, the open water buoy, a Datawell Waverider, was processed at 3-minute intervals with energy spectra reported in the frequency range ($0.025 < f < 0.635$ Hz). The difference in frequency bands may explain the discrepancy between the Waverider and SWIFT wave heights in open water. The Waverider was not equipped with an anemometer, thus no secondary wind speed measurement is shown in Figure 4.3a. The unaccompanied buoys were much farther apart (approximately 20 km) than the the buoys on July 30th and October 2nd (approximately 5 km or less); however, the wind and wave measurements were similar when both buoys were in open water, suggesting a valid open water comparison to the in-ice measurements.

The increases in average period with increased ice fraction, seen in Figure 4.3, are a result of the reduction of high frequency energy in the wave spectra, shown in Figure 4.4. Energy at low frequencies (longer periods) were seen to persist in the ice floes, while high frequencies (short waves) had energy levels 10-100 times less than buoys in open water. For the unaccompanied buoy, an onboard camera confirmed the presence of ice during this time, but did not provide sufficient field of view to estimate ice fraction. The observed decreases of high frequency wave energy in ice, reported here, are qualitatively consistent with the previous observations of wave spectra in ice [*Wadhams et al.*, 1986; *Doble and Bidlot*, 2013; *Collins-III et al.*, 2015].

Spectral wave directions and spread are given in Figure 4.5, where the difference in wave and wind direction is shown as $\cos(\theta_r)$, and the directional spread as, σ_θ. In open water, wind

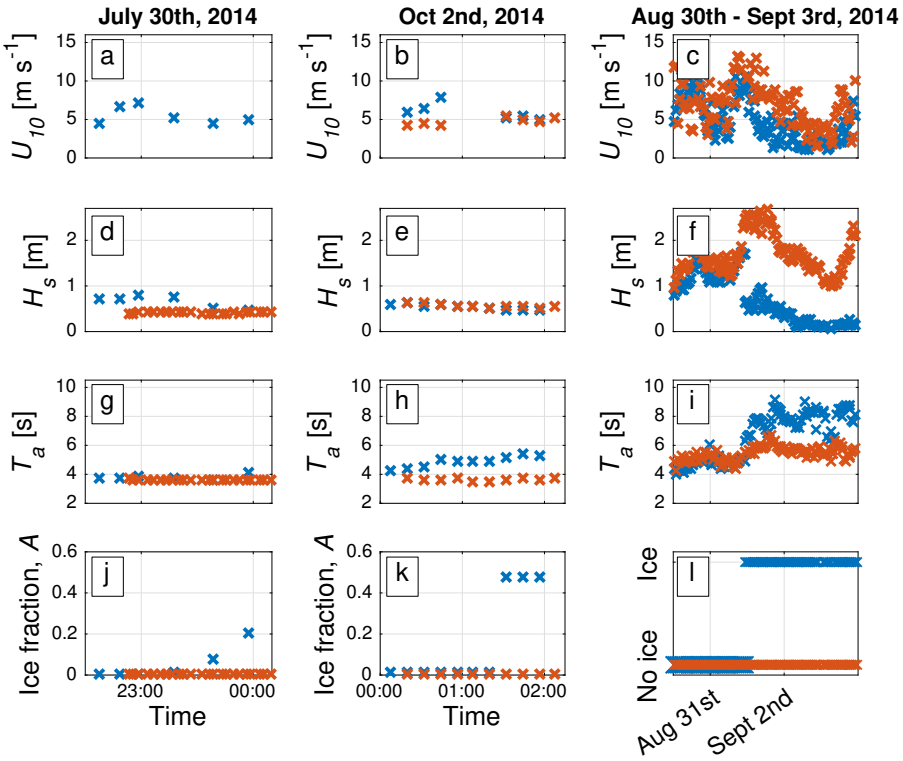

Figure 4.3: Measurements of wind speed (U_{10}, in a-c), significant wave height (H_s, in d-f), average wave period (T_a, in g-i), and ice fraction (A, in j-l) from the two ship-based deployments and for the unaccompanied buoys are shown. Blue represents buoys that transitioned into ice, while orange represents nearby, open water measurements. Wind speed measurements for open water are not available for the July 30th deployment (a), as the Waverider buoy was not equipped with an anemometer. The onboard camera for the endurance deployment confirmed the presence or absence of ice (l) but did not provide sufficient field of view to estimate ice fraction.

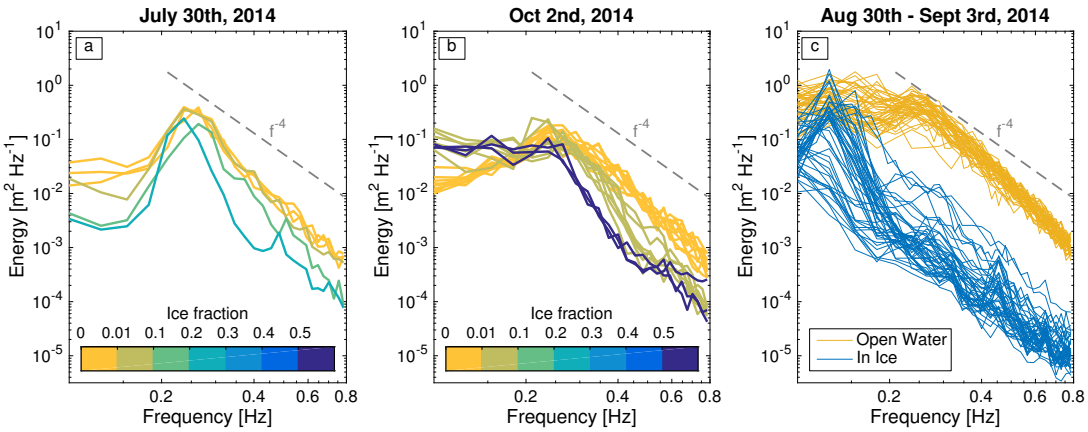

Figure 4.4: Wave spectral measurements from (a) July 30th, (b) October 2nd, and (c) the endurance deployment of August 30th - September 3rd, 2014, show energy reduction in ice at high frequencies—as much as 100 times the levels observed in open water with similar wind conditions. Lower frequencies show less attenuation, consistent with previous studies. No shipboard observations of ice fraction (c) are available for the endurance deployment (Figure 4.3). Gray dashed lines show an f^{-4} slope for reference.

and wave directions appear to be approximately aligned. Measurements in ice show decreased alignment of wind and waves, especially in the high-frequency components. This effect was most apparent in the October 2nd data (Figure 4.5b), where, in 1% and 50% ice fraction, $\cos(\theta_r)$ values at frequencies above 0.4 Hz are near zero. In addition, in-ice directional spreads on October 2nd (Figure 4.5e) are increased above 0.4 Hz. Both the wind/wave misalignment and increased directional spread indicate wave scattering due to ice at the high frequencies, qualitatively consistent with *Wadhams et al.* [1986]. The deployments on July 30th and the unaccompanied buoy on August 31st showed a similar, although less clear, trend, where wind and wave directions do not align in ice at high frequencies. The directional spread of these deployments did not show as clear an effect when compared with the October 2nd data. For the unaccompanied buoy (Figure 4.5f), the spread appears to decrease slightly in ice, but the open water directional spreads are relatively large compared with the other open water

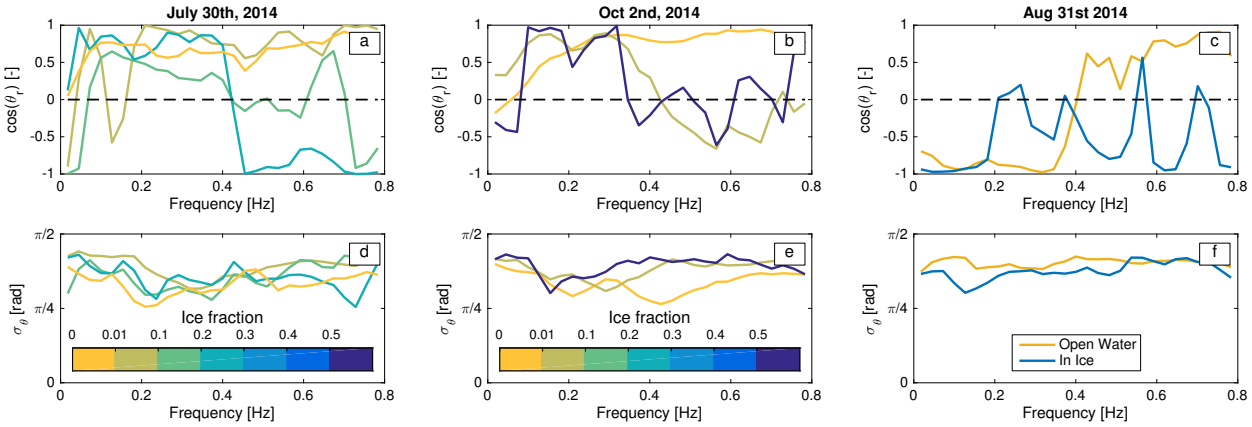

Figure 4.5: Wave spectral directions ($\cos(\theta_r)$, in a-c) and spread (σ_θ, in d-f) are shown from July 30th (a and d), October 2nd (b and e), and the unaccompanied buoy when it entered ice ($\pm$4 h of the open water/ice transition) on August 31st (c and f). Scattering appears at high frequencies when the buoys drifted into partial ice cover. Directional spread increased for these frequencies on October 2nd, and somewhat on July 30th. For visual clarity, the median relative directions and spreads are shown for each ice fraction bin, rather than each profile (as in Figure 4.4).

measurements (Figure 4.5d, and e). This effect is possibly due to a decrease of local wind, from $U_{10} = 10$ m s^{-1} early on August 31st, to $U_{10} < 5$ m s^{-1} by September 2nd (Figure 4.3c).

Near-surface TKE dissipation rates from all deployments also showed large reductions in the marginal ice zone (Figure 4.6). The decreases are one to two orders of magnitude, even for small fractions of ice coverage. This effect was accentuated at the surface in one case ($z < 0.3$ m; Figure 4.6b) when compared to the more uniform reductions in turbulence in another (Figure 4.6a). We speculate that the more depth-uniform, in-ice profiles on October 2nd may be due to ice-sourced turbulence introduced below the surface, as the buoy was visually observed to drift closer to ice floes during this deployment. Profiles from the unaccompanied buoy deployment (Figure 4.6c) showed both uniform and non-uniform reductions in TKE

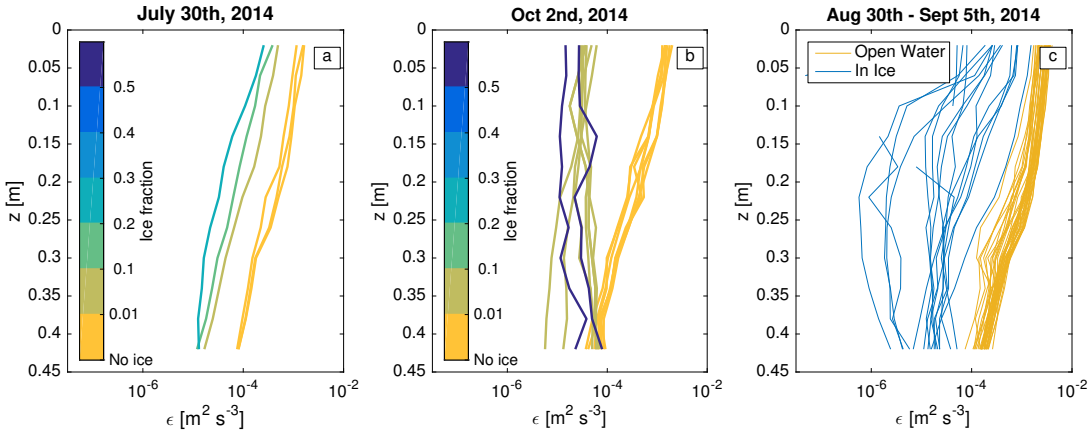

Figure 4.6: Ocean turbulence profiles in the top 45 cm are shown from (a) July 30th, (b) October 2nd, and (c) the unaccompanied deployment August 30th - September 5th, 2014. The dissipation rate of turbulent kinetic energy, $\epsilon(z)$, was reduced up to two orders of magnitude in partial ice cover when compared to similar open water wind conditions. The reduction of turbulence in the marginal ice zone is consistent with reduced energy in the wave field. No shipboard observations of ice fraction (c) are available for the endurance deployment (Figure 4.3).

dissipation rate. Some profiles were truncated near the surface due to acoustic reflections off of ice floes, which contaminate the data.

Damping, changes to relative wave direction, and increased directional spread serve to effectively decrease the wind input term, S_{wind}, a function of both $E(f)$ and $\cos(\theta_r)$ (Equation 4.2). High frequency contributions to S_{wind} are weighted larger than those at low frequency, both due to the ω in Equation 4.2, and to the $(1/c)^2$ (here, we use deep water dispersion, $c = g/\omega$) component of the *Plant* [1982] parameterization for β (Equation 4.3). Thus, preferential wave damping and directional changes at high frequencies can result in a large decrease of the total flux from wind into waves. These large reductions in flux, F (Equation 4.4), were seen to be in approximate balance with ocean surface TKE dissipation rates (Figure 4.7). Some estimates of F were negative due to contributions from $\cos(\theta_r)$, and

were not included in Figure 4.7; the negative values would imply waves doing work on the wind. Error bars for F represent the uncertainty of the constant in β (Equation 4.3), and do not include uncertainties in wave spectral or wind stress measurements. Error bars for TKE dissipation rate were estimated from the confidence intervals when fitting the structure function to an $r^{2/3}$ dependence (Equation 4.12). The data in Figure 4.7 correlate in log space across three decades ($R^2 = 0.66$, or $R^2 = 0.86$ without the unaccompanied buoy data of early September, with its reduced fidelity owing to the assumption of a drag coefficient). Most of the data fall close to the 1:1 line, although TKE dissipation rates were larger on average. The correlation was weakest for the lowest dissipation rates where instrument noise is relatively larger, and for the unaccompanied buoy where a drag coefficient is assumed in the wind source term. These are also the conditions in which ice-ocean shear from mean ice flow and lower frequency wave motions might cause turbulence dissipation not directly related to local wind-wave input.

4.4 Discussion

Our measurements indicate that the local input and dissipation of wave energy (shown in Figure 4.7) are generally not as large as the spatial gradients in wave energy flux, $\partial(Ec_g)/\partial x$, which we assume to be from wave-ice interactions, S_{ice}. A robust form of the ice dissipation term, S_{ice} is actively being pursued [*Liu and Mollo-Christensen*, 1988; *Liu et al.*, 1991; *Tolman*, 2003; *Wang and Shen*, 2010a; *Rogers and Orzech*, 2013]. The focus of this study was not to attempt to quantify S_{ice}, but the effects of S_{ice} are clearly important to the local balance, because S_{ice} is setting $\omega E(\omega)$ which in turn sets S_{wind} for any given wind forcing. We estimated the gradient of wave energy flux between open water and in-ice measurements, $\partial(Ec_g)/\partial x$, to be roughly 1 W m^{-2} for July 30th, and 10 W m^{-2} on October 2nd, and August 31st. These estimates assume ∂x to be the distance between buoys, rather than along ray paths (i.e., directional information was not used). However, these estimates are as big as,

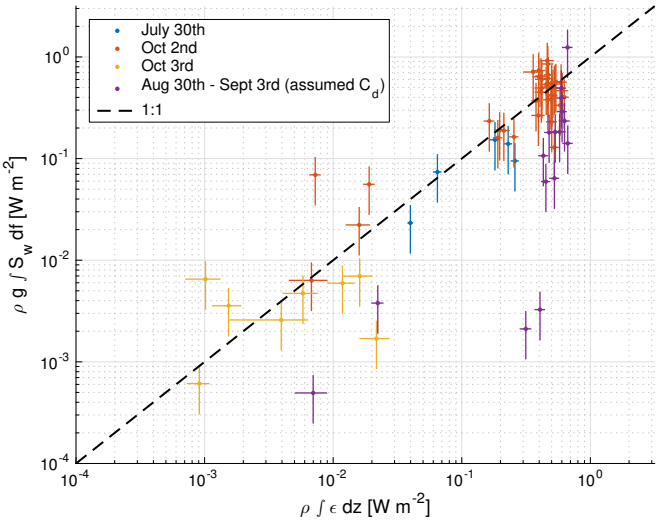

Figure 4.7: The estimated energy fluxes from wind to waves ($\rho g \int S_{wind} \mathrm{d}f$), are plotted against the vertically integrated ocean TKE dissipation rates ($\rho \int \epsilon \mathrm{d}z$). No wind stress measurements were available for the unaccompanied buoy (purple): therefore, u_* was estimated using the buoy-measured windspeed and a drag coefficient. Measurements fall approximately on the $1:1$ line, suggesting that the local wind energy flux to the waves sets the near-surface turbulence rates. Some estimates of F were negative due to contributions from $\cos(\theta_r)$, and were not included. Error bars for F represent the uncertainty of the constant in β (Equation 4.3), and do not include uncertainties in wave spectral or wind stress measurements. Error bars for TKE dissipation rates were estimated from the confidence intervals when fitting the structure function to an $r^{2/3}$ dependence (Equation 4.12).

or larger than, the largest measured near-surface dissipation rates or estimated wind inputs, about 1 W m^{-2}, in open water. Therefore, we assume that waves first lose energy to S_{ice}. The ice damping effects (shown in Figure 4.4) and scattering effects (shown in Figure 4.5) then reduce the magnitude of the wind input term. Since the damping is stronger at high frequencies, a local balance of wind input and dissipation still occurs. Restated, the waves lose energy to ice, and then, in a feedback, the waves are less effective at gaining energy from a given wind forcing. This effect, in turn, reduces the surface turbulence at a given wind forcing.

4.4.1 The effective transfer velocity, c_{eff}

The effective transfer velocity, c_{eff}, was estimated from the flux, F, (Equation 4.4), and the wind stress, τ, as $c_{eff} = F/\tau$. Figure 4.8 shows the ratio of in-ice to open water transfer velocity, $c_{eff,ice}/ceff, open$, with respect to ice fraction. Here, open water values were averaged when estimating, $c_{eff,open}$. We observed effective transfer velocities an order of magnitude lower relative to nearby open water estimates; in effect a less efficient transfer of mechanical energy from atmosphere. The largest reductions in F were seen on October 3rd, and in early September (Figure 4.7), but the respective transfer velocities are not shown in Figure 4.8 due to the unspecified ice fraction. Since c_{eff} encapsulates the total wave spectral changes due to ice as they affect F, the presentation in Figure 4.8 by ice fraction is overly simplistic, but still may be useful to understand an overall effect of partial cover.

4.4.2 Wind source term

More recent parameterizations for β (e.g., *Donelan and Pierson* [1987]; *Chalikov and Belevich* [1993]) have been shown to reduce scatter in measurements of wave growth rates. In this study, we chose the *Plant* [1982] parameterization for simplicity. We do not expect that the balance shown in Figure 4.7 would vary drastically if alternate forms of β were used to

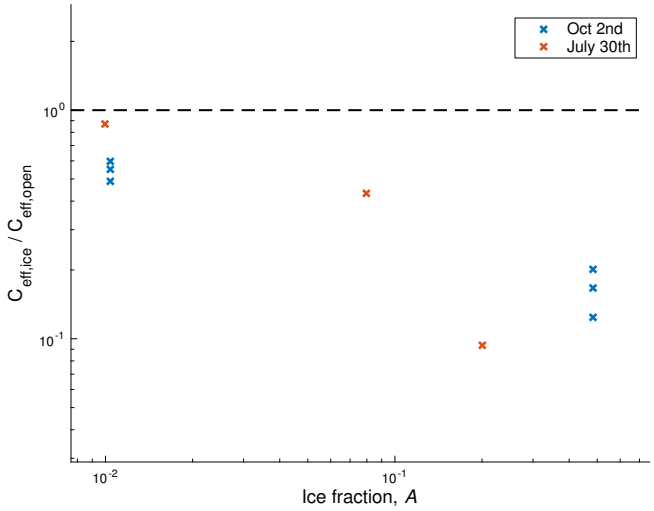

Figure 4.8: The ratio of effective transfer velocity in ice ($c_{eff,ice}$) to nearby open water conditions ($c_{eff,open}$) are plotted against ice fraction. The effective transfer velocity in open water is taken as the mean value of the nearby open water measurements. The in-ice transfer velocities are up to an order of magnitude smaller than the nearby open water counterparts, showing the decrease in energy flux from wind to waves.

estimate F, as wave damping accounts for a significant fraction of the decreases of F in ice, and $E(f)$ is independent of β (Equation 4.4). Furthermore, the directional contributions from $\cos(\theta_r)$ are analogous between parameterizations, and likely, wave scattering will result in a similar reduction of wind input. Often, negative $\cos(\theta_r)$ components (i.e., energy flux from waves to wind) are not included in wave models (e.g. *Tolman and Chalikov* [1996]). The scattering of waves in ice, however, results in many negative relative directional components (i.e., Figure 4.5), and thus wind input in ice may be sensitive to treatment of these negative components.

A commonality in the aforementioned wind input parameterizations is the dependence on wave phase speed, c. In this study we assumed the deep water dispersion relation, where wave phase speed $c = g/\omega$. However field [*Liu et al.*, 1991; *Fox et al.*, 2001], laboratory [*Wang and Shen*, 2010b], and theoretical [*Untersteiner*, 1986; *Wang and Shen*, 2010a] studies have shown that the dispersion relation of waves in ice differs from open water values, and would therefore be expected to modify the the phase speed, $c(\omega)$. For example, the results of *Liu et al.* [1991] suggest faster wave phase speeds in ice for wave periods less than 14 seconds, and slower phase speeds for wave periods above 14 seconds. These effects would increase the wind input from the low frequencies that were seen to persist farther into the ice pack, and decrease wind input for short, developing waves, when compared to open water.

4.4.3 Mechanisms for wave dissipation

Visual observations, shipboard video, and onboard buoy cameras showed little to no wave breaking in partial ice cover. This finding is consistent with the damping of short, steep waves which would otherwise be expected to break in similar open water environments. We have shown a quasi-equilibrium between the local wind input and the turbulent dissipation, and implicitly assumed that the near-surface turbulent dissipation rates were sourced from wave dissipation: however, wave dissipation is often attributed to wave breaking. The lack

of visible wave breaking calls into question the source of near-surface turbulence. The study of *Sutherland and Melville* [2015] has recently shown that dissipation by micro-breaking (breaking without forming a whitecap) also scales with wind input. This micro-breaking was only visible in infrared, and therefore would provide a pathway for wave dissipation consistent with the lack of observed whitecapping in partial ice cover. In the absence of (or in addition to) micro-breaking, viscous attenuation of waves by ice, and wave-induced shear, could also generate surface turbulence. In this scenario, the ice source/sink, S_{ice}, would replace the wave-breaking sink, S_{dis}, that commonly balances S_{wind} in the radiative transfer equation.

4.4.4 Implications for drag coefficients

Sea ice complicates the exchange of momentum at the ocean surface by balancing a portion of the wind stress. *Steele et al.* [1989] partitioned the wind stress, τ_{air}, linearly by ice fraction, A,

$$\tau_{air} = \rho u_*^2 = \rho[(1-A)C_{d,ocean} + AC_{d,ice}]U_{10}^2. \tag{4.13}$$

In the open ocean, the drag coefficient, $C_{d,ocean}$ is a function of wind speed, wave parameters, and fetch or time limitations [*Hwang*, 2005], and $C_{d,ice}$ has been shown to depend on ice fraction, floe geometry, melt ponds, ridges, and floe separation distance [*Tsamados et al.*, 2014]. Measurement of the individual drag coefficients is especially challenging in partial ice cover, because $C_{d,ocean}$ and $C_{d,ice}$ are not uniquely specified by U_{10} and u_* (Equation 4.13). However, it is not clear that use of the open water ocean drag coefficients is valid in partial ice cover, as wave-ice interactions alter wave spectra through damping and scattering. This study does not have a sufficient number of measurements across a range of A, U_{10} to fully parameterize $C_{d,ocean}$. Instead, we estimated average ice and ocean drag coefficients using all

available data with $A > 0$ in a least squares sense by solving the matrix equation,

$$\begin{bmatrix} u_{*1}^2 \\ \vdots \\ u_{*n}^2 \end{bmatrix} = \begin{bmatrix} (1-A_1)U_{10,1}^2 & A_1 U_{10,1}^2 \\ \vdots & \vdots \\ (1-A_n)U_{10,n}^2 & A_n U_{10,n}^2 \end{bmatrix} \begin{bmatrix} C_{d,ocean} \\ C_{d,ice} \end{bmatrix}. \tag{4.14}$$

Here, the subscripts $1 \cdots n$ represent separate measurements. We found $C_{d,ocean} = 1.0 \times 10^{-3}$ and $C_{d,ice} = 2.8 \times 10^{-3}$, using MATLAB's *mldivide* function. These estimates are comparable to open water drag coefficients at low wind speeds (see *Hwang* [2005]), and drag for brash ice and rough marginal ice zone floes [*Guest and Davidson*, 1991]. The data used to estimate drag coefficients (shown in Figure 4.3), had wind speeds of $U_{10} < 10$ m s^{-1}, $H_s < 1$ m, $T_a < 6$ s, and ice fractions ranging from 1 to 50%.

4.5 Summary

The use of measured of winds, waves, turbulence, and ice from the marginal ice zone has indicated that wave energy at high frequencies is strongly damped into the ice pack, while energy at low frequencies persists, consistent with previous studies. Spectral estimates of wave direction and spread are consistent with scattering primarily in the high frequencies for a subset of the deployments. Turbulent dissipation rates within 0.5 m of the free surface were reduced up to two orders of magnitude in partial ice cover when compared to nearby open water measurements. When depth-integrated, the ocean TKE dissipations roughly matched estimates of energy flux from the frequency-integrated wind source term across nearly three orders of magnitude. In partial ice cover, wind input occurred primarily at the low frequencies of the wave spectrum which did not experience significant damping or scatter. In contrast, the mechanism for wave dissipation, its frequency dependence, and subsequent turbulence generation is less clear. The local balance of wind input and surface turbulence is seen to be dependent on the ice-modified wave field, in addition to the wind stress. Thus, prediction of ocean surface turbulence in the marginal ice zone would necessitate knowledge of open

water wave parameters and ice attenuation. Finally, an average air-ocean drag coefficient of $C_{d,ocean} = 1.0 \times 10^{-3}$ has been estimated from ice fractions of 1-50% and wind speeds less than 10 ms^{-1}.

Chapter 5
CONCLUSIONS

5.1 Summary

In this thesis, measurements were used to quantify the modification of waves and turbulence at the ocean surface due to ice and currents. In Chapter 2, collocated measurements of currents, waves, and breaking events were used to evaluate the effect of currents on wave steepness and breaking. A consistent maximum finite-depth steepness was found when the vertical shear in currents was included in the dispersion relation, and the measured wave breaking was best explained by models that included the effects of currents. In Chapter 3, a new processing method was applied to analyze wave-breaking turbulence data measured from a drifter. A power-law decay model derived from the TKE equation fit the data well. In Chapter 4, measurements showed how broken brash ice modified short wind waves, decreasing both the wind input to the waves and the near surface ocean turbulence. Extended summaries of the main findings from each chapter is provided with a discussion of implications below.

At the Columbia River Mouth, application of the [*Kirby and Chen*, 1989] dispersion was important in estimating wave numbers, and thus wave steepness. Steepness is heavily linked to the other source/sink terms in modern wave models, and thus is important to predict accurately. However, it is common to forgo the effective current $U_{eff}(k)$ because of the added complexity – a full 3D current structure is needed to calculate this dispersion at all grid locations (although, some newer fully coupled models are including this term, for example *Warner et al.* [2010]). As discussed in *Akan et al.* [2017], including this dispersion in a model of the Columbia River Mouth affected waves at the offshore ebbing plume front. Using depth averaged currents (2D currents) lead to small dispersive effects, since it can be

quite deep offshore, with fast currents constrained near the surface. In contrast, *Akan et al.* [2017] showed there was significant amplification of waves at the front when the *Kirby and Chen* [1989] dispersion was used. Spectral measurements on either side of an ebbing front in [*Thomson et al.*, 2014] confirmed that these offshore fronts act as low pass filters where short waves were seen to break and/or be blocked at the fronts, while long waves propagated through into shallower water. Therefore, incorrect treatment of dispersive properties could incorrectly propagate waves throughout the domain.

Using the correct dispersion also revealed a limiting finite-depth bulk steepness existed in the data set, and that a number of wave-breaking models fit the measured breaking data well. These wave breaking parameterizations are central to many shallow and current-adjusted breaking dissipation models, such as *Thornton and Guza* [1983], *Chawla and Kirby* [2002], and *Filipot et al.* [2010]. However, there is still debate if wave/current breaking, which often occurs in intermediate water depths, should be treated more like shallow breaking or deep water breaking. A number of parameterizations modified from whitecapping (deep water) dissipation terms also show promise for use in wave/current environments [e.g., *Ris and Holthuijsen*, 1996; *van der Westhuysen*, 2012; *Rapizo et al.*, 2017]. *van der Westhuysen* [2012] argued that since wave/current breaking manifests qualitatively as weak and short crested, it should be governed by deep-water parameterizations. Although, short-crested breaking can certainly occur in the surf zone as well, and it's hard to completely disregard the role of depth in breaking in intermediate water, especially when considering the results in Chapter 2. This classification problem for wave/current and intermediate depth breaking quickly becomes philosophical without direct observation of wave dissipation (as each approach requires some heuristic or empirical arguments in their treatment of dissipation). Perhaps future studies on wave/current and intermediate depth breaking will help make, or eliminate the distinction between the shallow and deep regimes for breaking, possibly leading to a universal treatment of breaking and breaking dissipation for all relative water depths.

In Chapter 3, near-surface TKE and TKE dissipation rate measurements were compared with existing scalings and analytic solutions. Depth averaged turbulence values showed correlations with wave steepness, which was shown in Chapter 2 to relate well to wave breaking. Because we lacked direct estimates of wave dissipation, vertical turbulence profiles were normalized by the nearest surface measurement. The self-normalized profiles fit the shape of a power law decay, the solution to a diffusive-dissipative balance in one- and two-equation turbulence closure schemes. However, the constants needed for the analytic solution to match the measurements differed from commonly reported values. This suggests that the diffusive assumption for turbulent transport may not fully represent the physical processes taking place. *Kukulka and Harcourt* [2017] explored expanding the *Craig and Banner* [1994] balance to include the Craik-Leibovich vortex force production term. However, interpretation of the C-L TKE production term as it applies to surface following referenced measurements is not clear (for example, there is zero stokes drift in the buoy's reference frame at the surface). Another possibility is that turbulence constants may differ based on reference frame due to the addition of wave-motion terms [see, for example *Harcourt*, 2013].

Chapter 3 also provides direct estimates of turbulent length scale near the surface, helping constrain the surface roughness length, z_0. The surface roughness length has been one of the least constrained parameters in modeling near surface turbulence [*Soloviev and Lukas*, 2003; *Gemmrich and Farmer*, 2004; *Gerbi et al.*, 2013], and different parameterizations of z_0 in models often yield very different results [e.g., *Feddersen and Trowbridge*, 2005]. Given that it was difficult to fit the diffusive-dissipative balance with the linearly increasing length scale assumption and previously defined model constants, work is still needed to interpret the results. Wave motions severely complicate the physical meaning of a turbulent length scale, and interpretation of roughness length in the surface following reference frame as it relates to fixed surface coordinates is not clear.

Chapter 4 presents data from the Marginal Ice Zone, a region with distinct surface pro-

cesses from river inlets, but similar in that it modifies ocean waves and turbulence from deep water values. Measurements of waves in ice were compared to nearby open water measurements, showing strong damping of energy at high frequencies and modified directional properties. These measurements are qualitatively consistent with previous findings on waves in ice [*Wadhams et al.*, 1986]. Near surface turbulent dissipation rates were nearly balanced by estimates of wind input S_{wind} in open water and in ice, spanning nearly 3 decades (10^{-3} to 10^{0} W m^{-2}). This strongly suggests that open water wind input parameterizations are likely valid in fractional ice coverage if S_{ice} is appropriately treated. Further, this reduction of S_{wind} in ice has strong implications for air-sea interactions in the MIZ. The reduction of turbulence decreases the ease at which the fresh melt-layer from the ice will mix with the saltier ocean water. This mixing likely increases transfer of heat from the ocean layers below, modifying melt and/or freezing. The flux of momentum is slightly more complicated, as it is difficult to directly show the partition of wind momentum flux (i.e., wind stress) between ice and ocean.

5.2 Open questions

While a great deal was learned from these data sets, a number of questions arose from the analysis, or remain unanswered. At the Columbia River Mouth strong effects relating to spatial gradients are likely important, which were not resolved by the buoy point measurements recorded in the 2013 field campaign. In the MIZ, simply more data and better statistics will greatly aid in future work. Questions are listed below.

- How do strong horizontal gradients in currents affect wave transformation and breaking? Are waves reflected from these fronts? How large are the wave energy flux gradients across these river fronts, and is the resulting turbulence relevant to mixing?

- Can direct measurements of σ, k, and $U(z)$ be used to determine sheared current

dispersion directly, and does it differ from *Kirby and Chen* [1989]?

- How well do deep water wave dissipations modified for currents (i.e., *van der Westhuysen* [2012], *Rapizo et al.* [2017]) match dF/dx? Can these be used to accurately scale near-surface turbulence?

- How does wave-breaking turbulence interact with vertical density gradients at river inlets? When (if ever) is it important in plume depth? If wave-breaking turbulence does contribute to the mixing of river plumes, what scales the effect?

- Is the wave/current breaking process truly distinct from nearshore and deepwater wave breaking? Does it happen because of different mechanisms?

- What is the pathway of momentum across the air-ice-ocean interface? How is the transfer of momentum from the atmosphere partitioned to ice and ocean?

- What is the mechanism for surface turbulence in the MIZ if there was no visible wave breaking? Is microbreaking still active, and can this be detected with IR cameras?

- How does ice interact with turbulence directly? Is production from shear on larger ice floes important or large in comparison with other surface turbulence sources?

- How does new frazil ice modify the surface turbulence. What is the expected frazil concentration profile? How important are waves in this process?

5.3 Future Directions

The wave response to strong horizontal gradients in currents is a ripe topic for study. As was shown in Figure 3.10, these gradients can have a large effect on wave breaking and near surface turbulence. A photo of one such flooding front is shown in Figure 5.1, where the

Figure 5.1: A flooding front at the mouth of the Columbia River is shown above. The more turbid river water has a stark contrast with the bluer ocean water on the image right. Incoming ocean waves are traveling left to right across the image, however breaking crests appear to face a number of directions, indicating large changes in wave propagation direction. Wind direction was roughly out of the page (towards the observer). Photo taken by C. Bassett.

wave pattern is reminiscent of standing waves like those seen on the upwind side of a floating bridge. Some breaking crests appear to be propagating offshore (right to left), opposite the incoming wave direction, which perhaps is wave reflection off the strong current gradient. The active breaking region is relatively small (approximately 10 m wide), but offers a stark contrast with the wave features on either side. As was discussed earlier, these gradients act as a filter for shorter waves, allowing the propagation of longer waves farther into the inlet. However, the wave processes within and across the gradient are poorly defined.

Future field experiments hoping to understand the physical features in Figure 5.1 would need to to better characterize wave, current, and turbulence data in space. As mentioned in Chapter 4, drifters become trapped within the gradients, and offer no relevant information across them. Measurements from moorings or fixed structures would also have difficulties, because the fronts move rapidly in space and time. One way forward could be the use of stereo imaging, which has been successful at resolving 3D time evolving surface gravity waves

from both stationary platforms [*Benetazzo et al.*, 2012] and moving ships [*Schwendeman and Thomson*, 2017]. In theory, a ship mounted stereo video system could follow the river front, and characterize both dispersive properties, and spatial energy flux gradients. Accompanying measurements from an array of SWIFTs could be used to better determine turbulent and mean currents effects. CTD profiles, which were sparse in the 2013 project, could be more frequently sampled to better understand mixing and the distribution of density.

Characterizing turbulence very near the ocean surface in the presence of ice remains a challenge. Some work has been done to understand how frazil might form and be distributed near the ocean surface during freezing conditions. For example, *Svensson and Omstedt* [1998] included frazil terms into a k-ϵ model of the Ekman layer, and *Matsumura and Ohshima* [2015] coupled an LES model with a Lagrangian frazil model. Neither of these studies include ocean wave effects, which nearly always accompany frazil production in polynyas where strong winds are present. While wave breaking is likely absent or highly damped in such conditions, the wave influences are likely still relevant. Stokes-drift shear (i.e., Craik-Leibovich forcing) effects, or micro-breaking only effects may still be in play, although they likely result in turbulence profiles that differ from the results discussed in Chapter 3.

Perhaps one of the largest remaining questions is how to treat the partition of momentum transferred from the air to the ocean and ice. Currently, wave, ocean, and ice models treat this partition linearly, multiplying source/sink terms by ice or open water fraction. However, it's possible that momentum transfers are more complicated. For example, shading effects from taller ice floes may disrupt the formation of a classic logarithmic boundary layer over open sections of water. However closure of a full momentum budget across the air-ocean-ice boundary is difficult, and may require more advanced measurement devises and techniques. Stress estimates far from the boundary offer little insight into the pathway of momentum, and thus measurements of stress and motion for individual floes, and small patches of open water would be needed.

BIBLIOGRAPHY

Agrawal, Y., E. A. Terray, M. A. Donelan, P. A. Hwang, A. J. W. III, W. M. Drennan, K. Kahma, and S. A. Krtaigorodski, Enhanced dissipation of kinetic energy beneath surface waves, *Nature*, *359*, 219–220, doi:10.1038/359219a0, 1992.

Akan, Ç., S. Moghimi, H. Özkan-Haller, J. Osborne, and A. Kurapov, On the dynamics of the mouth of columbia river: Results from a three-dimensional fully coupled wave-current interaction model, *J. Geophys. Res. Oceans*, 2017.

Andrews, D. G., and M. McIntyre, An exact theory of nonlinear waves on a lagrangian-mean flow, *J. Fluid Mech.*, *89*(04), 609–646, 1978.

Ardhuin, F., et al., Semi-empirical dissipation source functions for ocean waves: Part I, definitions, calibration, and validations, *J. Phys. Oceanogr.*, *40*, 1917–1941, 2010.

Babanin, A. V., H.-H. Hwung, I. Shugan, A. Roland, A. van der Westhuysen, A. Chawla, and C. Gautier, Nonlinear waves on collinear currents with horizontal velocity gradient, *Proc. 12th Int. Workshop on Wave Hindcasting and Forecasting*, doi:http://www.waveworkshop.org/12thWaves/index.htm., 2011.

Banner, M., J. Gemmrich, and D. Farmer, Multiscale measurements of ocean wave breaking probability, *J. Phys. Oceanogr.*, *32*, 3364–3375, 2002.

Banner, M. L., A. V. Babanin, and I. Young, Breaking probability for dominant waves on the sea surface, *J. Phys. Oceanogr.*, *30*, 3145–3160, 2000.

Battjes, J. A., and J. P. F. M. Janssen, Energy loss and set-up due to breaking of random waves, *Coastal Engineering Proceedings 1.16*, 1978.

Belcher, S. E., et al., A global perspective on langmuir turbulence in the ocean surface boundary layer, *Geophys. Res. Lett.*, *39*(18), doi:10.1029/2012GL052932, 2012.

Benetazzo, A., F. Fedele, G. Gallego, P.-C. Shih, and A. Yezzi, Offshore stereo measurements of gravity waves, *Coastal Engineering*, *64*, 127–138, 2012.

Booij, N., R. C. Ris, and L. H. Holthuijsen, A third-generation wave model for coastal regions: 1. model description and validation, *J. Gephys. Res.*, *104(C4)*, 7649–7666, doi: 10.1029/98JC02622, 1999.

Bretherton, F. P., and C. J. Garrett, Wavetrains in inhomogeneous moving media, in *Proceedings of the Royal Society of London A: Mathematical, Physical and Engineering Sciences*, vol. 302, pp. 529–554, The Royal Society, 1968.

Burchard, H., Simulating the wave-enhanced layer under breaking surface waves with two-equation turbulence models, *J. Phys. Ocean.*, *31*, 2001.

Callaghan, A., G. de Leeuw, L. Cohen, and C. D. O'Dowd, Relationship of oceanic whitecap coverage to wind speed and wind history, *Geophys. Res. Lett.*, *L23609*, doi: 10.1029/2008GL036165, 2008.

Callaghan, A. H., G. B. Deane, and M. D. Stokes, Two regimes of laboratory whitecap foam decay: Bubble-plume controlled and surfactant stabilized, *J. Phys. Oceanogr.*, *43*(6), 1114–1126, 2013.

Campana, J., E. J. Terrill, and T. de Paolo, The development of an inversion technique to extract vertical current profiles from x-band radar observations, *J. Atmos. Ocean. Tech.*, *33*, 2016.

Canuto, V. M., A. Howard, Y. Cheng, and M. Dubovikov, Ocean turbulence. part i: One-point closure model—momentum and heat vertical diffusivities, *J. Phys. Oceanogr.*, *31*(6), 1413–1426, 2001.

Carniel, S., J. C. Warner, J. Chiggiato, and M. Sclavo, Investigating the impact of surface wave breaking on modeling the trajectories of drifters in the northern adriatic sea during a wind-storm event, *Ocean Model.*, *30*(2), 225–239, 2009.

Chalikov, D. V., and M. Y. Belevich, One-dimensional theory of the wave boundary layer, *Bound.-Layer Meteor.*, *63*, 65–96, 1993.

Chawla, A., and J. T. Kirby, Monochromatic and random wave breaking at blocking points, *J. Geophys. Res*, *107*(C7), 2002.

Chen, J. L., T. J. Hsu, F. Shi, B. Raubenheimer, and S. Elgar, Hydrodynamic and sediment transport modeling of new river inlet (nc) under the interaction of tides and waves, *J. Geophys. Res. Oceans*, *120*, doi:10.1002/2014JC010425, 2015.

Clark, D. B., S. Elgar, and B. Raubenheimer, Vorticity generation by short-crested wave breaking, *Geophys. Res. Lett.*, *39*(24), doi:10.1029/2012GL054034, 2012.

Collins-III, C. O., W. E. Rogers, A. Marchenko, and A. V. Babanin, In situ measurements of an energetic wave event in the arctic marginal ice zone, *Geophys. Res. Lett.*, *42*, doi: 10.1002/ 2015GL063063, 2015.

Comiso, J. C., and F. Nishio, Trends in the sea ice cover using enhanced and compatible amsr-e, ssm/i, and smmr data, *J. Geophys. Res.*, *113*(C02S07), doi:10.1029/2007JC004257, 2008.

Comiso, J. C., C. L. Parkinson, R. Gersten, and L. Stock, Accelerated decline in the arctic sea ice cover, *Geophys. Res. Lett.*, *35*(L01703), doi:10.1029/2007GL031972, 2008.

Craig, P. D., and M. L. Banner, Modeling wave-enhanced turbulence in the ocean surface layer, *J. Phys. Oceanogr.*, *24*, 2546–2559, 1994.

D'Asaro, E. A., J. Thomson, A. Y. Shcherbina, R. R. Harcourt, M. F. Cronin, M. A. Hemer, and B. Fox-Kemper, Quantifying upper ocean turbulence driven by surface waves, *Geophys. Res. Lett.*, *41*, 1–6, doi:10.1002/2013GL058193, 2014.

De Silva, I., and H. Fernando, Oscillating grids as a source of nearly isotropic turbulence, *Phys. Fluids*, *6*(7), 2455–2464, 1994.

Deike, L., L. Lenain, and W. K. Melville, Air entrainment by breaking waves, *Geophys. Res. Lett.*, doi:10.1002/2017GL072883, 2017.

Doble, M. J., and J.-R. Bidlot, Wave buoy measurements at the antarctic sea ice edge compared with an enhanced ecmwf wam: Progress towards global waves-in-ice modelling, *Ocean Model.*, *70*, 166–173, 2013.

Dodet, G., X. Bertin, N. Bruneau, A. B. Fortunato, A. Nahon, and A. Roland, Wave-current interactions in a wave-dominated tidal inlet, *J. Geophys. Res. Oceans*, *118*, 1–19, doi:10.1002/jgrc.20146, 2013.

Donelan, M. A., and W. J. Pierson, Radar scattering and equilibrium ranges in wind-generated waves with application to scatterometry, *J. Geophys. Res.*, *92*(C5), 2971–5029, doi:10.1029/JC092iC05p04971, 1987.

Drazen, D., W. K. Melville, and L. Lenain, Inertial scaling of dissipation in unsteady breaking waves, *J. Fluid Mech.*, *611*, 307–332, 2008.

Drazen, D. A., and W. K. Melville, Turbulence and mixing in unsteady breaking surface waves, *J. Fluid Mech.*, *628*, 85–119, 2009.

Drennan, W. M., M. A. Donelan, E. A. Terray, and K. B. Katsaros, Oceanic turbulence dissipation measurements in swade, *J. Phys. Ocean.*, *26*, 1996.

Duncan, J. H., An experimental investigation of breaking waves produced by a towed hydrofoil, *Proc. R. Soc. London Ser. A*, *377*, 331–348, 1981.

Edson, J. B., A. A. Hinton, K. E. Prada, J. E. Hare, and C. W. Fairall, Direct covariance flux estimates from mobile platforms at sea, *J. Atmos. Oceanic Tech.*, *15*(2), 547–562, 1998.

Elgar, S., B. Raubenheimer, and R. T. Guza, Current meter performance in the surf zone, *J. Atmos. Ocean. Tech.*, *18*, 1735–1746, 2001.

Farquharson, G., H. Deng, Y. Goncharenko, and J. Mower, Dual-beam ati sar measurements of surface currents in the nearshore ocean, in *Geoscience and Remote Sensing Symposium (IGARSS), 2014 IEEE International*, pp. 2661–2664, IEEE, 2014.

Feddersen, F., Observations of the surfzone turbulent dissipation rate, *J. Phys. Oceanogr.*, *42*, 386–399, 2012a.

Feddersen, F., Scaling surf zone turbulence, *Geophys. Res. Lett.*, *39*(18 (L18613)), doi: 10.1029/2012GL052970, 2012b.

Feddersen, F., and J. H. Trowbridge, The effect of wave breaking on surf-zone turbulence and alongshore currents: A modeling study, *J. Phys. Oceanogr.*, *35*(11), 2187–2203, 2005.

Feddersen, F., J. Trowbridge, and A. J. W. III, Vertical structure of dissipation in the nearshore, *J. Phys. Oceanogr.*, *37*, 1764–1777, 2007.

Fernando, H., and J. Hunt, Turbulence, waves and mixing at shear-free density interfaces. part 1. a theoretical model, *J. Fluid Mech.*, *347*, 197–234, 1997.

Fernando, H. J., Turbulent mixing in stratified fluids, *Annu. Rev. Fluid Mech.*, *23*(1), 455–493, 1991.

Filipot, J. F., F. Ardhuin, and A. V. Babanin, A unified deep-to-shallow water wave-breaking probability parameterization, *J. Geophys. Res.*, *115*(C04022), doi:10.1029/2009JC005448, 2010.

Fox, C., T. G. Haskell, and H. Chung, Dynamic, in-situ measurement of sea-ice characteristic length, *Ann. Glaciol.*, *33*, 339–344, 2001.

Francis, O. P., G. G. Panteleev, and D. E. Atkinson, Ocean wave conditions in the Chukchi Sea from satellite and in situ observations, *Geophys. Res. Lett.*, *38*(L24610), doi:10.1029/2011GL049839, 2011.

Gelfenbaum, G., D. Finlayson, P. Dartnell, E. Carlson, and A. Stevens, Bathymetry and backscatter from 2013 interforometric swath bathymetry systems survey of columbia river mouth, oregon and washington, *U.S. Geological Survey*, 2015.

Gemmrich, J., Strong turbulence in the wave crest region, *J. Phys. Oceanogr.*, *40*, 583–595, 2010.

Gemmrich, J., T. Mudge, and V. Polonichko, On the energy input from wind to surface waves, *J. Phys. Oceanogr.*, *24*, 2413–2417, 1994.

Gemmrich, J., C. J. Zappa, M. L. Banner, and R. P. Morison, Wave breaking in developing and mature seas, *J. Geophys. Res. Oceans*, *118*, 4542–4552, doi:10.1002/jgrc.20334, 2013.

Gemmrich, J. R., and D. Farmer, Observations of the scale and occurrence of breaking surface waves, *J. Phys. Oceanogr.*, *29*, 2595–2606, 1999.

Gemmrich, J. R., and D. Farmer, Near-surface turbulence in the presence of breaking waves, *J. Phys. Oceanogr.*, *34*, 1067–1086, 2004.

Gemmrich, J. R., M. L. Banner, and C. Garrett, Spectrally resolved energy dissipation rate and momentum flux of breaking waves, *J. Phys. Oceanogr.*, *38*, 1296–1312, 2008.

Gerbi, G., J. Trowbridge, E. Terray, A. J. Plueddemann, and T. Kukulka, Observations of turbulence in the ocean surface boundary layer: energetics and transport, *J. Phys. Oceanogr.*, *39*, 1077–1096, 2009.

Gerbi, G. P., R. J. Chant, and J. L. Wilkin, Breaking surface wave effects on river plume dynamics during upwelling-favorable winds, *J. Phys. Oceanogr.*, *43*(9), 1959–1980, 2013.

Gerbi, G. P., S. E. Kastner, and G. Brett, The role of whitecapping in thickening the ocean surface boundary layer, *J. Phys. Oceanogr.*, *45*(8), 2006–2024, 2015.

Gonzalez, F. I., and C. L. Rosenfeld, Slar and in situ observations of ocean swell modification by currents and bathymetry and the columbia river entrance, *IEEE Trans. Geosci. Remote Sens.*, *GE-22(6)*, 598–603, 1984.

Goring, D. G., and V. I. Nikora, Despiking acoustic doppler velocimeter data, *J. Hydraul. Eng*, *128*(1), 117–126, 2002.

Grasso, F., B. Castelle, and B. G. Ruessink, Turbulence dissipation under breaking waves and bores in a natural surf zone, *Cont. Shelf Res.*, *43*(0), 133–141, 2012.

Guerra, M., and J. Thomson, Turbulence measurements from 5-beam acoustic doppler current profilers, *J. Atmos. Ocean. Tech.*, (2017), 2017.

Guest, P. S., and K. L. Davidson, The aerodynamic roughness of different types of sea ice, *J. Geophys. Res*, *96*(C3), 4709–4721, 1991.

Hansen, J. E., T. T. Janssen, B. Raubenheimer, F. Shi, P. L. Barnard, and I. S. Jones, Observations of surfzone alongshore pressure gradients onshore of an ebb-tidal delta, *Coastal Eng.*, *91*, 251–260, 2014.

Harcourt, R. R., A second-moment closure model of langmuir turbulence, *J. Phys. Oceanogr.*, *43*(4), 673–697, 2013.

Herbers, T. H. C., and T. T. Janssen, Lagrangian surface wave motion and stokes drift fluctuations, *J. Phys. Ocean.*, *46*, doi:10.1175/JPO-D-15-0129.1, 2016.

Herbers, T. H. C., P. F. Jessen, T. T. Janssen, D. B. Colbert, and J. H. MacMahan, Observing ocean surface waves with gps-tracked buoys, *J. Atmos. Oceanic Tech.*, *29*, 944–959, 2012.

Holthuijsen, L. H., and T. H. C. Herbers, Statistics of breaking waves observed as whitecaps in the open sea, *J. Phys. Oceanogr.*, *16.2*, 290–297, 1986.

Hopkins, J., S. Elgar, and B. Raubenheimer, Observations and model simulations of wave-current interaction on the inner shelf, *J. Geophys. Res. Oceans*, *120*, doi: 10.1002/2015JC010788, 2015.

Horner-Devine, A. R., R. D. Hetland, and D. G. MacDonald, Mixing and transport in coastal river plumes, *Annu. Rev. Fluid Mech.*, *47*, 569–594, 2015.

Hwang, P. A., Temporal and spatial variation of the drag coefficient of a developing sea under steady wind-forcing, *J. Gephys. Res Oceans Res.*, *110*(C07024), doi: 10.1029/2005JC002912, 2005.

Janssen, T. T., and J. Battjes, A note on wave energy dissipation over steep beaches, *Coastal Engineering*, *54*(9), 711–716, doi:10.1016/j.coastaleng.2007.05.006, 2007.

Jones, N. L., and S. G. Monismith, The inlfuence of whitecapping waves on the vertical structure of turbulence in a shallow estuarine embayment, *J. Phys. Oceanogr.*, *38*, 1563–1580, doi:http://dx.doi.org/10.1175/2007JPO3766.1, 2008.

Kang, K., and D. D. Iorio, Depth-and current-induced effects on wave propagation into the altamaha river estuary, georgia, *Estuarine Coastal Shelf Sci.*, *66*, 395–408, 2006.

Kassem, S., and H. T. Ozkan-Haller, Forecasting the wave-current interactions at the mouth of the columbia river, or, usa, *33rd International Conference on Coastal Engineering, Santander, Spain*, 2012.

Kilcher, L. F., and J. D. Nash, Structure and dynamics of the columbia river tidal plume front, *J. Geophys. Res. Oceans*, *115*(C5), 2010.

Kirby, J. T., and T. Chen, Surface waves on vertically sheared flows: approximate dispersion relations, *J. Geophys. Res.*, *94*(C1), 1013–1027, 1989.

Kleiss, J. M., and W. K. Melville, Observations of wave breaking kinematics in fetch-limited seas, *J. Phys. Oceanogr.*, *40*(12), 2575–2604, doi:10.1175/2010JPO4383.1, 2010.

Kohout, A. L., M. J. M. Williams, S. M. Dean, and M. H. Meylan, Storm-induced sea-ice breakup and the implications for ice extent, *Nature*, *509*, 604–607, doi: 10.1038/nature13262, 2014.

Kolmogorov, A. N., Dissipation of energy in the locally isotropic turbulence, *Dokl. Akad. Nauk SSR*, *30*, 301–305, 1941.

Kuik, A. J., G. P. V. Vledder, and L. H. Holthuijsen, A method for the routine analyis of pitch-and-roll buoy wave data, *J. Phys. Ocean.*, *18*, 1020–1035, 1988.

Kukulka, T., and R. Harcourt, Influence of stokes drift decay scale on langmuir turbulence, *J. Phys. Oceanogr.*, *7*, doi:10.1175/JPO-D-16-0244.1, 2017.

Lagarias, J. C., J. A. Reeds, M. H. Wright, and P. E. Wright, Convergence properties of the nelder-mead simplex method in low dimensions., *SIAM Journal of Optimization*, *9*(1), 112–147, 1998.

Lamarre, E., and W. K. Melville, Air entrainment and dissipaiton in breaking waves, *Letters to Nature*, *351*, 469–472, 1991.

Lamont, J. C., and D. S. Scott, An eddy cell moedel of mass transfer into the surface of a turbulent liquid, *American Institute of Chemical Engineers*, *16*, 512–519, 1970.

Large, W., and S. Pond, Open ocean momentum flux measurements in moderate to strong winds, *J. Phys. Oceanogr.*, *11*, 324–336, 1981.

Liu, A. K., and E. Mollo-Christensen, Wave propagation in a solid ice pack, *J. Phys. Oceanogr.*, *18*, 1702–1712, 1988.

Liu, A. K., B. Holt, and P. W. Vachon, Wave propagation in the marginal ice zone: Model predictions and comparisons with buoy and synthetic aperture radar data, *J. Geophys. Res.*, *96*(C3), 4605–4621, 1991.

Liu, P., M. W. Dingemans, and J. K. Kostense, Long-wave generation due to the refraction of short-wave groups over a shear current, *J. Phys. Ocean.*, *20*, 53–59, 1990.

Longuet-Higgins, M. S., and R. W. Stewart, Radiation stress and mass transport in gravity waves, with application to 'surf beats', *J. Fluid Mech.*, *13*(4), 481–504, doi: http://dx.doi.org/10.1017/S0022112062000877, 1962.

Longuet-Higgins, M. S., and J. Turner, An 'entraining plume'model of a spilling breaker, *J. Fluid Mech.*, *63*(01), 1–20, 1974.

Loose, B., W. R. McGillis, D. Perovich, C. J. Zappa, and P. Schlosser, A parameter model of gas exchange for the seasonal ice zone, *Ocean Sci.*, *10*, 17–28, 2014.

Lumley, J. L., and E. A. Terray, Kinematics of turbulence convected by a random wave field, *J. Phys. Oceanogr.*, *13*, 2000–2007, 1983.

Lund, B., H. C. Graber, H. Tamura, C. O. Collins, and S. M. Varlamov, A new technique for the retrieval of near-surface vertical current shear from marine x-band radar images, *J. Geophys. Res. Oceans*, *120*, doi:10.1002/2015JC010961, 2015.

Martin, T., M. Steele, and J. Zhang, Seasonality and long-term tred of arctic ocean surface stress in a model, *J. Gephys. Res Oceans*, *119*(1723-1738), doi:10.1002/ 2013JC009425, 2014.

Masson, D., A case study of wave-current interaction in a strong tidal current, *J. Phys. Ocean.*, *26*(359-372), 1996.

Matsumura, Y., and K. I. Ohshima, Lagrangian modelling of frazil ice in the ocean, *Ann. Glaciol.*, *56*(69), 373–382, 2015.

Mendez, G. M. D., M. C. Haller, B. Raubenheimer, S. Elgar, and D. A. Honegger, Radar remote sensing estimates of waves and wave forcing at a tidal inlet, *J. Atmos. Ocean. Tech.*, *32*, 842–854, 2015.

Miche, A., Mouvements ondulatoires de la mer en profondeur croissante ou décroissante. forme limite de la houle lors de son déferlement. application aux digues maritimes. troisiéme partie. forme et propri es des houles limites lors du déferlement. croissance des vitesses vers la rive, *Ann. Ponts et Chaussées*, *114*, 369–406, 1944.

Moghimi, S., J. Thomson, T. Özkan-Haller, L. Umlauf, and S. Zippel, On the modeling of wave-enhanced turbulence nearshore, *Ocean Model.*, *103*, 118–132, 2016.

Monahan, E. C., Oceanic whitecaps, *J. Phys. Ocean.*, *1*, 139–144, 1971.

Monahan, E. C., and I. O. Muircheartajgh, Optimal power-law description of oceanic whitecap coverage dependence on wind speed, *J. Phys. Ocean.*, *10*, 2094–2099, 1980.

Mori, N., T. Suzuki, and S. Kakuno, Noise of acoustic doppler velocimeter data in bubbly flow, *ASCE J. Eng. Mechanics*, *133*(1), 122–125, doi:10.1061/(ASCE)0733-9399(2007)133:1(122), 2007.

Noh, Y., and H. Jin Kim, Simulations of temperature and turbulence structure of the oceanic boundary layer with the improved near-surface process, *J. Geophys. Res. Oceans*, *104*(C7), 15,621–15,634, 1999.

Olabarietta, M., J. C. Warner, and N. Kumar, Wave-current interaction in willapa bay, *J. Geophys. Res. Oceans*, *116*(C12014), doi:10.1029/2011JC007387, 2011.

Olabarrieta, M., W. R. Geyer, and N. Kumar, The role of morphology and wave-current interaction at tidal inlets: An idealized modeling analysis, *J. Gephys. Res. Oceans*, *119*, 8818–8837, 2014.

Pearman, D., T. H. C. Herbers, T. T. Janssen, H. D. van Ettinger, and S. A. McIntyre, Drifter observations of the effects of shoals and tidal-currents on wave evolution in san francisco bight, *Cont. Shelf Res.*, *91*, 109–119, 2014.

Perlin, M., W. Choi, and Z. Tian, Breaking waves in deep and intermediate waters, *Annu. Rev. Fluid Mech.*, *45*, 115–145, 2013.

Phillips, O. M., Spectral and statistical properties of the equilibrium range in wind-generated gravity waves, *J. Fluid Mech.*, *156*, 495–531, 1985.

Pizzo, N., and W. K. Melville, Vortex generation by deep-water breaking waves, *J. Fluid Mech.*, *734*, 198–218, 2013.

Plant, B., A relationship between wind stress and wave slope, *J. Geophys. Res.*, *87*, 1961–1967, 1982.

Rainville, L., C. M. Lee, and R. A. Woodgate, Impact of wind-driven mixing in the arctic ocean, *Oceanography*, *24*(3), 136–145, 2011.

Rapizo, H., A. Babanin, D. Provis, and W. Rogers, Current-induced dissipation in spectral wave models, *J. Gephys. Res Oceans*, *122*, doi:10.1002/2016JC012367, 2017.

Rapp, R. J., and W. K. Melville, Laboratory measurements of deep-water breaking waves, *Phil. Trans R. Soc. Lond. A*, *331*, 735–800, 1990.

Rascle, N., and F. Ardhuin, Drift and mixing under the ocean surface revisited: Stratified conditions and model-data comparisons, *J. Geophys. Res. Oceans*, *114*(C02016), doi: 10.1029/2007JC004466, 2009.

Raubenheimer, B., R. T. Guza, and S. Elgar, Wave transformation across the inner surf zone, *J. Geophys. Res.*, *101*(C10), 25,589–25,597, 1996.

Ris, R. C., and L. H. Holthuijsen, Spectral modelling of current induced wave-blocking, *Proc. 25th Int. Conf. on Coastal Eng., ASCE*, pp. 1247–1254, 1996.

Rogers, W. E., and M. D. Orzech, Implementation and testing of ice and mud source functions in wavewatch iii, nrl memorandum report, *Tech. rep.*, NRL/MR/7320-13-9462, 31 pp., 2013.

Rogers, W. E., and S. Zieger, New wave-ice interaction physics in wavewatch iii, *Tech. rep.*, Naval Research Laboratory, 2014.

Rosman, J. H., and G. P. Gerbi, Interpreting fixed-location observations of turbulence advected by waves: Insights from spectral models, *J. Phys. Oceanogr.*, *47*(4), 909–931, 2017.

Rousseaux, G., C. Mathis, P. Maissa, T. G. Philbin, and U. Leonhardt, Observation of negative-frequency waves in a water tank: a classical analogue to the hawking effect?, *New Journal of Physics*, *10*, doi:10.1088/1367-2630/10/5/053015, 2008.

Rousseaux, G., P. Maissa, C. Mathis, P. Coullet, T. G. Philbin, and U. Leonhardt, Horizon effects with surface waves on moving water, *New Journal of Physics*, *12*, doi:10.1088/1367-2630/12/9/095018, 2010.

Rusch, C., J. Thomson, S. Zippel, and M. Schwendeman, Video recognition of breaking waves, *Oceans-St. John's, IEEE*, doi:10.1109/OCEANS.2014.7002994, 2014.

Schwendeman, M., and J. Thomson, A horizon-tracking method for shipboard video stabilization and rectification, *J. Atmos. Ocean. Tech.*, *32*, 164–176, 2015a.

Schwendeman, M., and J. Thomson, Observations of whitecap coverage and the relation to wind stress, wave slope, and turbulent dissipation, *J. Gephys. Res. Oceans*, *120*, 8346–8363, 2015b.

Schwendeman, M. S., and J. Thomson, Sharp-crested breaking surface waves observed from a ship-based stereo video system, *J. Phys. Oceanogr.*, *47*(4), 775–792, 2017.

Scully, M. E., J. H. Trowbridge, and A. W. Fisher, Observations of the transfer of energy and momentum to the oceanic surface boundary layer beneath breaking waves, *J. Phys. Oceanogr.*, *46*(6), 1823–1837, 2016.

Soloviev, A., and R. Lukas, Observation of wave-enhanced turbulence in the near-surface layer of the ocean during toga coare, *Deep Sea Research Part I: Oceanographic Research Papers*, *50*(3), 371–395, 2003.

Spreen, G., L. Kaleschke, and G. Heygster, Sea ice remote sensing using amsr-e 89-ghz channels, *J. Geophys. Res. Oceans*, *113*(C2), 2008.

Squire, V. A., Of ocean waves and sea ice revisited, *Cold Regions Sci. Tech.*, *49*, 110–133, 2007.

Steele, M., J. H. Morison, and N. Untersteiner, The partition of air-ice-ocean momentum exchange as a function of ice concentration, floe size, and draft, *J. Geophys. Res.*, *94*, 12,739–12,750, 1989.

Stewart, R. H., and J. W. Joy, Hf radio measurements of surface currents, *Deep-Sea Research*, *21*, 1039–1049, 1974.

Stokes, G. G., Considerations relative to the greatest height of oscillatory irrotational waves which can be propagated without change of form, *Mathematical and physical papers 1*, pp. 225–228, 1880.

Sutherland, P., and W. K. Melville, Field measurements of surface and near-surface turbulence in the presence of breaking waves, *J. Phys. Ocean.*, *45*, 943–965, 2015.

Svensson, U., and A. Omstedt, Numerical simulations of frazil ice dynamics in the upper layers of the ocean, *Cold Regions Sci. Tech.*, *28*(1), 29–44, 1998.

Tennekes, H., Eulerian and lagrangian time microscales in isotropic turbulence, *J. Fluid Mech.*, *67*(03), 561–567, 1975.

Tennekes, H., and J. L. Lumley, *A first course in turbulence*, MIT press, 1972.

Terray, E., M. Donelan, Y. Agrawal, W. Drennan, K. Kahma, A. Williams, P. Hwang, and S. Kitaigorodskii, Estimates of kinetic energy dissipation under breaking waves, *J. Phys. Oceanogr.*, *26*, 792–807, 1996.

Thompson, D. R., and J. Jensen, Synthetic aperture radar interferometry applied to ship-generated internal waves in the 1989 loch linnhe experiment, *J. Geophys. Res. Oceans*, *98*(C6), 10,259–10,269, 1993.

Thomson, J., Wave breaking dissipation observed with SWIFT drifters, *J Atmos Ocean Tech*, *29*(12), 1866–1882, doi:10.1175/JTECH-D-12-00018.1, 2012.

Thomson, J., and A. Jessup, A fourier-based method for the distribution of breaking crests from video observations, *J. Atmos. Ocean. Tech.*, *26*, 2009.

Thomson, J., and W. E. Rogers, Swell and sea in the emerging arctic ocean, *Geophys. Res. Lett.*, *41*, doi:10.1002/2014GL059983, 2014.

Thomson, J., E. A. D'Asaro, M. Cronin, E. Rogers, R. Harcourt, and A. Schcerbina, Waves and the equilibrium range at Ocean Weather Station P, *J. Geophys. Res.*, *118*, 1–12, 2013.

Thomson, J., A. R. Horner-Devine, S. Zippel, C. Rusch, and W. Geyer, Wave breaking turbulence at the offshore front of the columbia river plume, *Geophys. Res. Lett.*, *41*, doi:10.1002/2014GL062274, 2014.

Thomson, J., M. Schwendeman, S. F. Zippel, S. Moghimi, J. Gemmrich, and W. E. Rogers, Wave-breaking turbulence in the ocean surface layer, *J. Phys. Ocean.*, *46*, doi: 10.1175/JPO-D-15-0130.1, 2016.

Thornton, E. B., and R. T. Guza, Transformation of wave height distribution, *Journal of Geophysical Research*, *88*(C10), 5925–5938, 1983.

Thorpe, S. A., Langmuir circulation, *Annu. Rev. Fluid Mech.*, *36*, 55–79, doi: 10.1146/annurev.fluid.36.052203.071431, 2004.

Tolman, H. L., Treatment of unresolved islands and ice in wind wave models, *Ocean Model.*, *5*, 219–231, 2003.

Tolman, H. L., and D. Chalikov, Source terms in a third-generation wind wave model, *J. Phys. Ocean.*, *26*, 2497–2518, 1996.

Trulsen, K., and C. C. Mei, Double refelction of capillary/gravity waves by a non-uniform current: a boundary-layer theory, *J. Fluid Mech.*, *251*, 239–271, 1993.

Tsamados, M., D. L. Feltham, D. Schroeder, D. Flocco, S. L. Farrell, N. Kurtz, S. W. Laxon, and S. Bacon, Impact of variable atmospheric and oceanic form drag on simulations of arctic sea ice, *J. Phys. Oceanogr.*, *44*, 1329–1353, 2014.

Umlauf, L., and H. Burchard, A generic length-scale equation for geophysical turbulence models, *J. Mar. Res.*, *61*, 235–265, 2003.

Umlauf, L., H. Burchard, and K. Hutter, Extending the k–ω turbulence model towards oceanic applications, *Ocean Model.*, *5*(3), 195–218, 2003.

Untersteiner, N. (Ed.), *The Geophysics of Sea Ice*, Plenum, New York, 1986.

Vagle, S., J. Gemmrich, and H. Czerski, Effect of upper ocean stratification on turbulence and optically active bubbles, *J. Geophys. Res.*, *117*(C00H16), doi:10.1029/2011JC007308, 2012.

van der Westhuysen, A. J., Spectral modeling of wave dissipation on negative current gradients, *Coastal Eng.,*, *68*, 17–30, doi:10.1016/j.coastaleng.2012.05.001, 2012.

Wadhams, P., V. A. Squire, J. A. Ewing, and R. W. Pascal, Effect of the marginal ice zone on the directional wave spectrum of the ocean, *J. Phys. Oceanogr.*, *16*, 358–376, 1986.

Wadhams, P., V. A. Squire, D. J. Goodman, A. M. Cowan, and S. C. Moore, The attenuation rates of ocean waves in the marginal ice zone, *J. Geophys. Res*, *93*(C6), 6799–6818, 1988.

Wang, R., and H. H. Shen, Gravity waves propogating into an ice-covered ocean: A viscoelastic model, *J. Geophys. Res.*, *115*(C06024), doi:10.1029/2009JC005591, 2010a.

Wang, R., and H. H. Shen, Experimentla study on surface wave propagating through a grease-pancake ice mixture, *Cold Regions Sci. Tech.*, *61*, 90–96, doi:10.1016/j.coldregions.2010.01.011, 2010b.

Wang, X. L., Y. Feng, and V. R. Swail, Historical changes in the beaufort-chukchi-bering seas surface winds and waves, 1971-2013, *J. Climate*, *28*, 7457–7469, doi:10.1175/JCLI-D-15-0190.1, 2015.

Warner, J. C., B. Armstrong, R. He, and J. B. Zambon, Development of a coupled ocean–atmosphere–wave–sediment transport (coawst) modeling system, *Ocean Model.*, *35*(3), 230–244, 2010.

Wiles, P., T. P. Rippeth, J. Simpson, and P. Hendricks, A novel technique for measuring the rate of turbulent dissipation in the marine environment, *Geophys. Res. Let.*, *33*, L21,608, 2006.

Yao, A., and C. H. Wu, Incipient breaking of unsteady waves on sheared currents, *Physics of Fluids*, *17*, doi:10.1063/1.2000276, 2005.

Yelland, M., P. Taylor, I. Consterdine, and M. Smith, The use of the inertial dissipation technique for shipboard wind stress determination, *J. Atmos. Ocean. Tech.*, *11*, 1093–1108, 1994.

Young, I., *Wind Generated Ocean Waves*, Elsevier Ocean Engineering Book Series, Elsevier, New York, 1999.

Zappa, C. J., P. A. Raymond, E. A. Terray, and W. R. McGillis, Variation in surface turbulence and the gas transfer velocity over a tidal cycle in a macro-tidal estuary, *Estuarries*, *26*(6), 1401–1415, 2003.

Zippel, S., Wave breaking and turbulence at a tidal inlet: Shoals, currents, and winds, Master's thesis, University of Washington, 2014.

Zippel, S., and J. Thomson, Wave breaking and turbulence at a tidal inlet, *J. Geophys. Res. Oceans*, *120*, doi:10.1002/2014JC010025, 2015.

Zippel, S., and J. Thomson, Surface wave breaking over sheared currents: Observations from the mouth of the columbia river, *J. Geophys. Res. Oceans*, *122*, 3311–3328, doi:10.1002/2016JC012498, 2017.